5-2023

Tumor targeting gold nanoparticles for delivery of RNA and DNA oligonucleotide therapies for glioblastoma.

Nicholas Allen
University of Louisville

Recommended Citation

Allen, Nicholas, "Tumor targeting gold nanoparticles for delivery of RNA and DNA oligonucleotide therapies for glioblastoma." (2023). *Electronic Theses and Dissertations.* Paper 4094.
https://doi.org/10.18297/etd/4094

TUMOR TARGETING GOLD NANOPARTICLES FOR DELIVERY OF RNA AND DNA OLIGONUCLEOTIDE THERAPIES FOR GLIOBLASTOMA

By

Nicholas C. Allen

A Dissertation Submitted to the Faculty of the
Graduate School in Partial Fulfillment of the Requirements for the Degree of

Doctor of Philosophy in
Interdisciplinary Studies: Specialization
in Translational Bioengineering

Interdisciplinary Studies
University of Louisville
Louisville, Kentucky

May 2023

TUMOR TARGETING GOLD NANOPARTICLES FOR DELIVERY OF RNA AND DNA OLIGONUCLEOTIDE THERAPIES FOR GLIOBLASTOMA

By

Nicholas C. Allen

A Dissertation Approved on

April 28, 2023

By the following Dissertation Committee:

Dr. Martin O'Toole, Dissertation Chair

Dr. Erin Gerber

Dr. Carolyn Klinge

Dr. Jonathan Kopechek

Dr. Patricia Soucy

DEDICATION

This work is dedicated to all my friends and family who have supported me for the past 13 years.

ACKNOWLEDGEMENTS

I began the journey toward receiving a Ph.D. immediately after my high school graduation in 2010. During this whole time, my parents, siblings, and grandparents have supported me in more ways than I can honestly remember. Through their never-ending love and support, I know I would not be where I am today. While not all my siblings or grandparents could witness this accomplishment, they cared deeply about my success and would be thrilled to see me succeed.

Since 2010, I have met many wonderful and supportive people who helped me reach this point. First, I would like to thank my calculus professor Dr. Linda Mayhew for instilling a sense of only accepting the facts outright if trying to prove them yourself. Her constant learning challenges helped develop how I approached many of the topics in this dissertation. Second, I would like to acknowledge Dr. Patricia Soucy for being the first to offer me the chance to pursue research. Her thoughtfulness and commitment to my success have been the constant drive to get me through all stages of my career leading up to this dissertation. Lastly, I would like to thank my friend of 14 years, Megan. Her family has treated me like their own, and she has been a critical reason I can be here today. She has always let me be my most authentic self and has asked for nothing in return for her extreme generosity.

I approached Dr. O'Toole about joining his lab in May of 2017, where he graciously gave me a chance to work on developing the technology described in the rest of this dissertation. Dr. O'Toole's continual support and motivation always painted a

bright picture, even on the darkest days. He allowed me to develop the work to call it my own, all while giving invaluable guidance and suggestions when necessary. He has been patient and a model dissertation advisor during my professional development. With his constant pursual of the following steps, I am where I am at today professionally.

Many research friends and staff have also helped me along in this journey. Kurtis James and Rajat Chauhan gave me the tools to develop and critically analyze gold nanoparticles for various applications. Betty Nunn gave me continual support in obtaining the resources needed to complete all research tasks and was invaluable in assisting with animal studies. Emtias Chowdhury, Rayeanne Balgemann, Larissa Pack, and Nagwa El Baz helped me see it through by lending their support and sometimes just being a soundboard for the days when I needed to vent or get other opinions and insights to confounding results.

ABSTRACT

TUMOR TARGETING GOLD NANOPARTICLES FOR DELIVERY OF RNA AND DNA OLIGONUCLEOTIDE THERAPIES FOR GLIOBLASTOMA

Nicholas Allen

April 28, 2023

Glioblastoma (GBM) brain tumors are highly aggressive gliomas due to genetic and cellular heterogeneity. Current GBM treatment consists of surgical resection of the tumor combined with radio- or chemo-therapies. While these treatments have increased the life expectancy for GBM patients up to 20 months, they have had little effect on the 5-year survival rate. The complex cellular and genetic composition of the tumor makes current treatments less effective long term. One approach to developing more effective GBM treatments is to customize nanoparticle-based drug delivery systems that can directly target the aberrant gene expression patterns within a particular GBM tumor. Delivery systems that include oligonucleotide therapies are ideal for this approach due to their ease of synthesis and ability to tailor the oligonucleotide base sequence to allow the targeting of specific gene sequences and proteins. Two therapeutically relevant classes of oligonucleotides, DNA aptamers (*e.g.,* AS1411) and RNA-interfering anti-sense microRNAs (anti-miRs), have exhibited anti-GBM properties. However, their use as standalone therapies is hindered by instability within *in vitro* and *in vivo* environments and the inability to cross some biological barriers. The conjugation of individual oligonucleotides to the surface of gold nanoparticles (GNPs) has been shown to help overcome these difficulties to make AS1411 and anti-miRs viable therapeutics for GBM; however, the conjugation of both oligonucleotides to GNPs has not been investigated. This dissertation presents a novel GNP therapy incorporating AS1411 and an anti-miR as a multi-faceted therapy against GBM. Anti-miR-21 (A21) targets miR-21, a microRNA implicated in the increased aggressiveness of GBM tumors. U-87 MG GBM cells treated with GNPs coated with AS1411 and the polymer poly (ethylene glycol) (PEG/AS1411 GNPs) displayed decreased cellular metabolic activity and growth with altered cell morphology. The GNPs were optimized based on the PEG to AS1411 ratio to maximize these bioactive effects against GBM cells. An optimal ratio of 1:3 PEG to AS1411 conjugated GNPs exhibited ~ 72% inhibition of cellular metabolic activity, reduced growth by 75%, and profoundly affected cellular morphology. The effects of AS1411 were enhanced upon conjugation to GNPs. Additionally, using a base-substituted analog of AS1411 showed that the effects on U-87 MG cells were specific to the sequence of AS1411. In addition, this dissertation details the synthesis of AS1411 GNPs coated with A21 (PEG/AS1411/A21 GNPs) and investigates the benefit of A21 addition to PEG/AS1411 GNPs. Treatment of U-87 MG cells with PEG/AS1411/A21 GNPs retained the effects seen from PEG/AS1411 GNPs and significantly lowered the motility rate of U-87 MG cells. PEG/AS1411/A21 GNPs showed additional effects on gene expression patterns of U-87 MG cells due to A21 addition. PEG/AS1411/A21 GNPs reduced miR-21 expression 3-fold in U-87 MG cells. The ability of PEG/AS1411/A21 GNPs to influence the expression of miR-21-associated proteins PTEN and STAT3 within U-87 MG cells was also investigated. The *in vivo* performance of PEG/AS1411 GNPs, with or without A21, was investigated within a mouse orthotopic xenograft model of GBM. Both

GNP types were shown to cross the blood-brain barrier and influence tumor progression. Mice treated with PEG/AS1411 GNPs ultimately survived longer (47 days post-tumor implantation) than untreated mice (37.5 days)

TABLE OF CONTENTS

LIST OF FIGURES

LIST OF TABLES

CHAPTER 1

INTRODUCTION

1.1 Current State of Glioblastoma

Glioblastoma multiforme (GBM) is the most common primary brain tumor that affects adults. GBM is one of the most lethal human cancers due to its invasive growth and tumor heterogeneity [1, 2]. GBM accounts for an estimated 54% of all brain gliomas and is considered the most aggressive form of glioma, with a progression-free survival of 6.2-7.8 months and a median overall survival of 14.6-20.5 months [3, 4]. Standard treatments include surgical resection followed by radio- and chemo-therapies. Despite improving prognoses, these treatments are not specific to GBM tumor tissues, are toxic to surrounding non-cancerous tissues, and do not consider the tumoral heterogeneity of GBM.

Surgery is essential for accurate pathological and molecular diagnosis. While surgery releases tumor burden by removing tumor tissues, incomplete resection is common [5]. Surgical resection is highly affected by confounding variables from patient to patient [6]. These variables include factors from tumors, patients, and doctors, such as accessibility, comorbidities, and experience. Efforts have been made to improve resection through pre-operative imaging techniques. Still, the diverse biological behaviors that contribute to the clinical aggressiveness of GBM can be elusive to such methods and thus result in lower rates of complete tumor resection [6].

In treating GBM, concomitant treatment with radio- and chemo-therapies are employed to minimize deficiencies from the surgical resection [3]. Radiotherapy consists of 60 Gy exposure intraoperatively to the vasculature and stromal tissues of the tumor bed. This radiotherapy treatment has been shown to mitigate GBM cell proliferation due to the anatomical and temporal advantage of the treatment [3]. Temozolomide (TMZ), the standard in GBM chemotherapy, is an oral prodrug that inhibits growth by methylating DNA bases within GBM tumor cells, eventually causing cellular apoptosis [7]. While treatments with radio- or chemo-therapies are explicitly administered to GBM tumors, they are non-specific and affect surrounding healthy tissues. Radiotherapy can cause local radiation necrosis, while TMZ can cause neural and hematological toxicities [7]. Moreover, TMZ is not advantageous as a long-term standalone treatment due to the ability of GBM to acquire resistance to TMZ [7].

Radio- and chemo-therapy standards of care for GBM have improved patient prognoses. However, they are still considered poor, with a 5-year survival rate of only 7.2% in the United States [8]. Thus, there is a need to improve upon GBM treatment. Understanding GBM cellular heterogeneity and its contribution to GBM tumorigenesis can enhance GBM treatments.

1.2 Genetic, Structural, and Molecular Basis of Glioblastoma

GBM tumors can originate from neural stem cells (NSC), oligodendrocyte precursor cells, and NSC-derived astrocytes. This gives rise to intra- and inter-tumor heterogeneity and a high degree of genomic complexity. GBM tumors are classified based on genetic markers as mesenchymal, classical, proneural, or neural [8]. While a GBM tumor is classified as one of these subgroups, other cell types can be present within the same GBM tumor. These different subgroups vary locally and temporally within a GBM tumor and contribute to genomic characteristics that lead to tumor resistance to therapies, aiding in recurrence rates associated with GBM.

The blood-brain barrier (BBB) is a cellular barrier that prevents the efficient passage of cancer therapeutics into the central nervous system [9]. It comprises specialized endothelial cells and supporting cells (*i.e.,* pericytes, oligodendrocytes, and astrocytes) controlling the inter- and intra-cellular passage of soluble molecules to and from the brain [10, 11]. At the sub-cellular level, the BBB comprises tight junctions, carrier-mediated proteins, solute carriers, and active efflux transporters [12]. Similar properties can be found in the blood-brain tumor barriers (BBTB) formed by GBM tumors. These properties of the BBB and BBTB present additional obstacles when treating GBM tumors with chemotherapies. Ultimately, therapeutic levels of chemotherapy drugs are challenging to maintain in GBM tumors because of the BBB and BBTB [13].

GBM *in vitro* models have increased our fundamental understanding of GBM biology and facilitated the development of novel treatment strategies [14]. The most common cell lines commercially available for *in vitro* studies of GBM include U-87 MG, U251, T98G, and A172 [15]. The U-87 MG and U251 cell lines were generated from male GBM patients and were derived from malignant gliomas [16, 17]. Human U-87 MG cells have been utilized in over 1700 publications in the past 40 years [18]. Additionally, the genome of U-87 MG cells has been fully sequenced. Thus, these cells can be utilized *in vitro* studies to identify crucial biomolecular mechanisms in GBM tumorigenesis, identify new therapeutic targets, and enhance rapid and reproducible testing of targeted drugs. U-87 MG cells are a valuable tool for *in vitro* prescreening new anti-GBM therapeutics [19].

Studies on GBM cells such as U-87 MG have enhanced the understanding that multiple genetic alterations in GBM tumors aid in their tumorigenesis. A fundamental discovery in GBM cell genetic alteration came from discovering microRNAs (miRNAs).

miRNAs are endogenously expressed, short, noncoding RNAs produced by GBM cells, including U-87 MG cells [20, 21]. miRNAs will negatively control messenger RNA (mRNA) targets in one of two ways depending on the degree of complementarity to their targets. miRNA binding leads to either degradation of the target mRNA and/or the inhibition of mRNA transcript translation. In GBM, miRNAs can participate in fine tuning tumorigenesis mechanisms, including cell cycle control, proliferation, differentiation, and apoptosis [22]. Targeting miRNAs with drug-like small molecules such as oligonucleotides is gaining interest when generating new therapies for GBM.

1.3 Oligonucleotides as Cancer Therapies

Oligonucleotides, described as short oligomers of DNA or RNA, have gained interest as therapeutics against various diseases since Vitravene, the first FDA-approved oligonucleotide therapy in 1998, was used to treat cytomegalovirus retinitis in immunocompromised patients [23]. Common oligonucleotide therapeutics include antisense oligonucleotides, aptamers, short interfering RNA (siRNA), miRNA, and anti-sense-miRNAs (anti-miRs) [23, 24]. Oligonucleotides can target substrates at the DNA, RNA, or protein levels. Most importantly, oligonucleotides can modulate cellular pathways that are not easily targeted with other drugs or therapeutics [25]. Two classes of oligonucleotides, aptamers and anti-miRNAs, are the focus of the topics presented in this dissertation.

1.3.1 Use of Aptamers as Cancer Therapies

Aptamers are synthetic DNA or RNA molecules that form specific secondary and tertiary structures allowing them to bind peptides, proteins, ions, bacteria, viruses, or other cell targets [26, 27]. Beginning with early reports of aptamers in 1990 [27], aptamer technology has expanded to include DNA or RNA aptamers, synthetic ribozymes, and DNAzymes. Aptamers are ideal for pharmaceutical applications due to their unique features, including high sensitivity and selectivity, small size, rapid penetration into target tissues, low immunogenicity, high thermal stability, and resistance to denaturation [26, 28-30]. Aptamer research has focused on generating therapeutic and diagnostic applications, including those in oncology for treating prostate, breast, brain, blood, colon, lung, ovarian, and other cancers [27, 31].

AS1411, a 26-mer DNA sequence (5'GGTGGTGGTGGTTGTGGTGGTGGTG), is a serum-stable quadruplex aptamer that binds to the RNA binding domains of the nuclear phosphoprotein, nucleolin [32]. Nucleolin is highly expressed on the cell surface of cancerous cells [32, 33]. In normal non-proliferating cells (*i.e.,* not cancerous), nucleolin is restricted to the cell nucleus [34]. Thus, nucleolin is a therapeutic target for developing new anti-cancer treatments. While the role of nucleolin is not entirely understood, its interactions with different proteins and cellular signaling pathways that drive tumorigenesis have been investigated.

Nucleolin interacts with epidermal growth factor receptor (EGFR) and Ras signaling proteins [35]. Downstream signaling molecules of EGFR include signal transducer and activator of transcription 3 (STAT3) and phosphatidylinositol-3 kinase (PI3K) [36]. The increased signaling activity of these molecules has been linked with critical events of tumorigenesis, such as proliferation, invasion, and evasion of apoptosis [37]. Moreover, the inactivation of the tumor suppressor phosphotensin protein (PTEN) promotes an increase in PI3K signaling, causing additional increases in tumor cell growth and proliferation [38]. Ras signaling proteins are involved in the Ras-MEK-ErK pathway, leading to ErK activation. Activation of ErK can induce endothelial-mesenchymal transition, which increases the invasiveness of tumorigenic cells [39].

Nucleolin mediates cellular proliferation, migration, invasion, and growth through interactions with other signaling molecules. Nucleolin has been linked to HER2 (ERB2, a member of the EGFR family) [32], transcripts for B-cell lymphoma 2 (BCL2) [40], protein kinase B (AKT) [41], and matrix metalloproteinase 9 (MMP9) [40]. Treating U-87 MG cells with nucleolin and Ras inhibitors (AS1411 and Salisrasib, respectively) increased cell death and decreased cell migration [41]. Thus, nucleolin is a promising target for developing anti-cancer treatments, including GBM.

Among the numerous nucleolin inhibitors investigated, AS1411 has been studied extensively[32]. It has been combined with other cancer therapies (*e.g.,* doxorubicin, gemcitabine, and cisplatin) and incorporated into different formulations (*e.g.,* polymer constructs, nanoparticles, and liposomes). These combinations and formulations of AS1411 have been used in various cancer applications (*e.g.,* GBM, breast, and ovarian) [42-52]. Moreover, the safety profile of the nucleolin targeting ability of AS1411 has been established through phase I and II clinical trials.

The phase I trial (n=30 patients) established the maximally tolerated dose of 22 mg/kg AS1411 through an escalated dose study scheme. Results from this trial confirmed the lack of severe toxicity and showed promising activity in renal cancers [53]. The phase II trial investigated the overall response rate of AS1411 treatment in renal cell carcinoma patients as its primary endpoint [54]. Progression-free survival and safety were secondary endpoints. It was determined that one patient had a potent and durable response to AS1411 treatment, and only 34% of treated patients (n= a total of 35 study patients) had a mild or moderate adverse AS1411-related event. Thus, AS1411 showed a rare yet dramatic and durable response with low toxicity [54]. These results have led to more investigations into the usability of AS1411 in improving cancer medicines.

1.3.2 Use of miRNA Inhibitors as Cancer Therapies

miRNAs were first discovered in *C. elegans* by the Ambros group in 1993 [55]. It was found that a small-non-protein-coding RNA affected the development of *C. elegans* by regulating the expression of the protein lin-14. Since this seminal discovery, thousands of miRNA precursor genes are now known to process into mature miRNA sequences via miRNA biogenesis and achieve bioactivity through a cellular response pathway known as RNA interference (RNAi) [56]. RNAi was first published in 1998 and is described as a formation of double-stranded RNA between miRNA and mRNA transcripts, causing the prevention of mRNA translation into proteins [57]. Briefly, the miRNA gene is transcribed in the nucleus into primary miRNA and then modified into pre-miRNA by the nuclear DROSHA complex before its transport to the cytoplasm [58]. Pre-miRNA is then processed by a protein complex, Dicer, into a mature miRNA, where it can interact with the RNA-induced silencing complex (RISC). Once miRNAs are incorporated into RISC, they can bind to their mRNA target in the 3' untranslated region leading to translational repression or mRNA transcript degradation.

The alteration of the RNAi mechanism can affect the processing, stability, or targeting of miRNAs, leading to disease states such as cancer [59]. Chromosomal abnormalities and transcriptional control changes contribute to the role of RNAi in tumorigenesis [56]. Changes in the number of copies of miRNA genes through chromosomal amplification, deletion, or translocation can give rise to abnormal miRNA expression in malignant cells. Moreover, miRNA expression is tightly regulated by transcription factors (TFs) [60, 61]). TFs can up-regulate oncogenic miRNA biogenesis and down-regulate transcriptional activity of tumor suppressive miRNAs, including in GBM [62-65]. This regulatory control can contribute to GBM tumorigenesis by affecting cell-cycle progression, promoting GBM cell proliferation, and evading apoptosis [66]. Thus, the ability of miRNAs to influence GBM tumorigenesis makes them a promising target for GBM therapeutics [67].

Targeting down- or up-regulated miRNAs can be achieved by miRNA mimics or inhibitors, respectively. miRNA mimics can repress tumorigenesis via targeting over-expressed oncoproteins, while miRNA inhibitors can down-regulate oncogenic miRNAs. miRNA inhibitors possess potent and specific inhibition of miRNA targets. In addition, they act by restoring gene-related miRNA expression of tumor suppressors [68] or inhibiting proto-oncogene-related miRNAs, thus reducing tumorigenic activity [69, 70]. Therefore, miRNA inhibitors are strong candidates for generating new anti-cancer therapeutics and can be applied to developing new anti-GBM therapies [71, 72].

1.4 Nanoparticle Systems for Delivering Oligonucleotides

Oligonucleotide therapies such as AS1411 and miRNA inhibitors have been established as strong candidates for developing new anti-cancer therapies. However, their instability towards nuclease degradation, inability to evade the defensive phagocytes of the reticuloendothelial system (RES), and the ease of their renal excretion limit their clinical translation [73]. Chemical modifications to oligonucleotides can overcome these challenges [25]. These modifications can include changes to the sugar, phosphodiester linkage, or base components of the oligonucleotides [74]. However, the delivery of modified oligonucleotides is difficult due to physiological barriers *in vivo*. These include the tumor stroma (which can limit drug penetration), poor intracellular internalization, and entrapment and degradation by the endosomal/lysosomal acidic environments within cells [73]. These limitations of delivering oligonucleotides *in vivo* are further complicated by the continued long-term susceptibility of oligonucleotides to nuclease and RES activity [73], the density of the extracellular matrix causing poor diffusion [75], and the electrostatic repulsions between negatively charged oligonucleotides and the negatively charged plasma membranes [76]. Utilizing nanoparticle systems can aid in overcoming these challenges of oligonucleotide delivery.

The introduction of oligonucleotides into nanoparticle systems is approached physically (through encapsulation of the oligonucleotide within a nano-sized construct) or chemically. Oligonucleotides can interact with cationic molecules through their negatively charged backbones, generating complex nanoparticle structures that have been used successfully as transfection agents [77]. Moreover, oligonucleotides can be loaded within lipophilic nanoparticle systems specially designed to carry oligonucleotides through interactions with a hydrophilic hollow cavity [78]. Oligonucleotides can also directly bind to metallic nanoparticle surfaces through established chemical interactions (*i.e.,* gold-thiol chemistry) [79, 80].

Standard laboratory instruments such as ultraviolet spectrometers (UV-VIS) and dynamic light scattering instruments (DLS) can be used to monitor the success of nanoparticle syntheses [81-83]. These characteristics of nanoparticle systems obtained from UV-VIS and DLS techniques are hydrodynamic size, zeta potential, polydispersity indices (PDI), surface plasmon resonance (SPR), and loading efficiencies of loaded molecules.

Zeta potential represents the surface charge of nanoparticles and is accepted as a measure of electro-repulsive stability with absolute values > 20 millivolts desired [84]. PDI values measure the distribution of sizes in each nanoparticle solution with ranges from 1.0 (polydispersed) to 0.0 (monodispersed) [85]. UV-VIS spectra can give a qualitative analysis of a successful nanoparticle surface modification by examining the location and/or shifting of characteristic SPR bands of plasmonic nanoparticles within the UV-VIS spectra [86]. Loading efficiencies of therapeutics/coating molecules into nanoparticle systems can be determined using multiple methods. The easiest is by fluorescently tagging the molecule of interest and comparing the fluorescent output of a nanoparticle system with unknown loading to standard concentrations of loaded molecules [87].

Combining oligonucleotides with nanoparticle systems has some benefits compared to stand-alone oligonucleotides. These include improved stability from the increased density of packing of oligonucleotides on the nanoparticle surface, enhanced cellular uptake of oligonucleotide/nanoparticle systems, and the ability of nanoparticles to achieve on-target delivery of oligonucleotides [73]. These benefits lead to the more effective delivery of oligonucleotides due to the ability of nanoparticles to be endocytosed via numerous mechanisms (determined by nanoparticle size, charge, and shape) as well as the ability of some nanoparticles to respond to specific tumor microenvironment-based stimuli to release incorporated oligonucleotides. Lastly, *in vivo* delivery of oligonucleotides loaded in nanoparticle systems to tumors benefits from the enhanced permeability and retention (EPR) effect.

The EPR effect, first coined in 1987, is the phenomenon that nanoparticles preferentially accumulate within tumors and have a prolonged presence [88]. This is due to the "leakiness" of tumor vasculature, through which nanoparticles can extravasate more readily than in healthy vasculature, and poor lymphatic drainage surrounding tumor tissues [89]. Moreover, incorporating polyethylene-glycol (PEG) constructs, which can deter protein and cellular adhesion, within nanoparticle systems increases nanoparticle circulation time *in vivo*, allowing for enhanced EPR effects. The first commercialized nanomedicine, Doxil ®, highlights the result of PEG addition on the EPR effect of the nanoparticles [90]. Doxil is a PEGylated liposomal form of the chemotherapy agent doxorubicin. In preclinical trials, Doxil was shown to increase the delivery of doxorubicin 300-fold more than free doxorubicin. This resulted in a 4- to 16-fold difference in drug retention within tumor tissues because of the EPR effect. Since the EPR effect was established, the application of therapeutics into nanoparticle systems has exponentially grown [88].

1.5 Oligonucleotide-Based Nanoparticles for Glioblastoma

AS1411 has gained momentum as a viable therapy for GBM. Nucleolin, a significant target of AS1411, is highly abundant in the plasma membrane of U-87 MG cells [91]. The binding of AS1411 to nucleolin can further affect downstream molecular processes of proliferation, migration, invasion, and survival involved in tumorigenesis due to the interrelationships of nucleolin and EGFR [91, 92]. In 2015, it was determined that while the initial cellular uptake of AS1411 was not dependent on nucleolin, its presence on the cell surface stimulated further uptake of AS1411 into the targeted cell [93]. This interaction drives the internalization of AS1411 into the cell 24-72 hours after treatment [94], where AS1411 can induce cell death via non-apoptotic pathways. Thus, AS1411-functionalized nanoparticle-based drug delivery systems have been a focus of designing new cancer therapies, including for GBM [95].

In addition to AS1411, oligonucleotides that can interfere with miRNA activity in cancers are increasingly gaining more interest as potential therapies for nanoparticle systems. In the context of GBM, many miRNAs have been discovered that, if bound by an anti-miR oligonucleotide, could provide a therapeutic target. Out of the miRNAs researched, the following have had effects classified in GBM: miRNA-7 [96, 97], miRNA-34a [98, 99], miRNA-128 [100, 101], miRNA-10b [20, 96], miRNA-21 [20, 102-106], and miRNA-93 [107, 108]. Most of these miRNAs were first discovered as early as 2005 by Cirafe et al. [20] when microarray analysis examined the expression levels of 254 miRNAs in GBM. Since then, a significant body of research has been dedicated to exploring their control and use as therapeutic targets through delivering miRNA inhibitors (anti-miRs). The most widely studied miRNA in GBM is miRNA-21 (miR-21).

1.5.1 Targeting of Nucleolin with AS1411 modified Nanoparticle Systems

Recent demonstrations of using AS1411-modified nanoparticle systems for GBM applications include molecular imaging [109, 110], targeted drug delivery [95, 109, 111-113], and viral vector generation [114]. These applications use AS1411 in combination with specific or generalized GBM therapies such as miRNAs [109], cRGD binding ligands [110], paclitaxel [111], 5-fluorouracil and doxorubicin [95, 110, 113], or transferrin [112], to either initiate an anti-GBM response or to label GBM cells. Delivery of these molecules is completed with various nanoparticle vehicles, including chitosan-gold nanoparticles [95], magnetic fluorescent nanoparticles [109], gold nanoclusters [110], poly(l-g-glutamyl glutamine)-paclitaxel nanoconjugates [111], ruthenium nanoparticles [112], or superparamagnetic iron oxide nanocrystals [113]. Regardless of their design, the overarching goals of creating new nanoparticle systems for GBM are to reduce the off-target effects of chemotherapy agents, allow access past the BBB, and increase the anti-cancer activity of incorporated therapies.

An example of using AS1411-based nanoparticle therapies in GBM comes from the Ramezani group [113]. This was one of the first designs to suggest using AS1411-based treatments for GBM applications. This group loaded magnetic SPION-PLGA-PEG nanospheres with doxorubicin and conjugated the surfaces with AS1411. These nano constructs had measured characteristics of size, zeta potential, and PDI values of 176.4 ± 5.6 nm, -30.1 ± 2.9 mV, and 0.12 ± 0.05, respectively, suggesting a stable nanoparticle system. Due to the ability of AS1411 to target nucleolin, a 3.75-fold increase in doxorubicin toxicity to glioma-representing cells was noted.

Other groups have investigated AS1411-based nanoparticle systems for GBM applications. The Kim group provided a foundation for generating more complex nanoparticle designs with proven efficacy in GBM, spinal, and other cancer models [109]. Their group created a multimodal theranostic silica-coated magnetic iron oxide nanoparticle coated with AS1411 and anti-miR-221 oligonucleotides. AS1411 allowed for specific and targeted delivery to cancer cells with an approximately 3.5 times significant increase in nanoparticle uptake. Further conjugation of the nanoparticles with anti-miR-221 conferred a significant cytotoxic effect (up to 50% decrease in C6 (astrocytoma) cell viability) after two days of treatment with the anti-miR present. These data lend credence to combinatorial AS1411-based therapies within a single nanoparticle system in GBM applications.

1.5.2 Using miR-21 Inhibitors in Nanoparticle Systems

In 2005, the Krichevsky group reported on the anti-apoptotic effects of miR-21 in GBM cells [102]. Krichevsky also identified an inverse relationship with miR-21 promoting proliferation while decreasing apoptosis within GBM cells. This work showed that transfection of GBM cells with anti-miR-21 (A21) oligonucleotides led to a 35% decrease in GBM viability and a 3-fold increase in apoptotic caspase activity. This sparked investigations into the role of miR-21 in other cancers, with Krichevsky noting that miR-21 most likely has effects in cervical adenocarcinomas, leukemia, prostatic adenocarcinoma, and colon, kidney, and breast cancers [115]. While these effects can be seen in GBM, the biological effects of any miRNA are highly dependent on cell-specific gene expression.

Since Krichevsky's 2005 paper, the biological effects of miR-21 have been investigated in-depth by examining alterations to cell-signaling pathways that contribute to various cellular functions. It is known that miR-21 is involved in GBM cell invasion and cell growth [20, 102, 104, 116-121], apoptosis [116, 122], angiogenesis [122], cellular outgrowth [118, 121, 123], migration [118, 120], metastasis [117-119] and proliferation [120-122]. All of these contribute to tumorigenesis and tumor survival. miR-21 modulates the activity of critical cell signaling molecules affecting these biological processes, either directly or indirectly [124]. By transfecting various cancer cell lines (including GBM) with miR-21 inhibitors (*e.g.*, A21), the cell signaling molecules listed in **Table 1-1** have been determined to interact with miR-21. While not an exhaustive list, understanding the complexities and interactions on the cellular level is a step forward in verifying new and novel therapies utilizing miR-21 inhibitors such as A21.

Table 1-1

Cell Signaling Proteins Modulated by miR-21

miR-21 Expression	**Cell Signaling Protein Expression**	**Biological Effects**	**Ref.**
Decreased	Increased Programmed Cell Death 4 (PDCD4)	Decreased Invasion and Cell Growth Increased Apoptosis	[123, 125, 126]
Increased	Decreased reversion-inducing-cysteine-rich protein with kazal motifs (RECK)	Increased Invasion	[104]
Increased	Decreased tissue inhibitor of metalloproteinase 3 (TIMP3)	Increased Invasion	[104]
Decreased	Decreased signal transducer and activator of transcription 3 (STAT3)	Decreased Proliferation	[124, 127, 128]
Decreased	Decreased tropomyosin alpha-1 (TPM)	Decreased Invasion and Proliferation	[123]
Increased	Decreased sprouty homolog 2 (SPRY2)	Increased Invasion	[123]
Decreased	Increased phosphatase and tensin homolog (PTEN)	Decreased Invasion, Migration, and Proliferation	[123, 125, 126, 129]

miR-21 acts as an oncogenic miRNA GBM tumorigenesis. Thus, blocking the downstream effects of miR-21 overexpression in GBM via miR-21 inhibitors (*i.e.*, A21) has gained interest since 2006. Research has focused on using A21 as a therapeutic to block miR-21 activity and reduce miR-21 levels in GBM both *in vitro* and *in vivo*. To date, utilizing A21 to reduce miR-21-related gene expression within GBM has been applied in nanoparticle systems [125], biomaterials [130], genetic engineering [127], and microfluidic applications [131]. Of these, the most notable to discuss is the work done by the Croce group [125].

In 2019, Croce designed RNA nanoparticles with A21 using locked nucleic acids (locked nucleic acids (LNAs) confer stability and longevity of nucleic acids) [125]. These nanoparticles were established from the three-way junction core of packaging RNA (pRNA-3WJ) within bacteriophages. Croce's group was able to adapt these pRNA-3WJs with A21 sequences and synthesize nanoparticles with precise control of shape, size, and stoichiometry. pRNA-3WJ nanoparticles labeled with A21 RNA (pRNA-3WJ-RNPs) measured 10.97 ± 1.47 nm in size and -20.37 ± 1.88 mV in charge—indicating a reliable and stable particle synthesis. pRNA-3WJ-RNPs produced a 4-fold decrease in the expression of endogenous mature miR-21. They also showed a dose-dependent reduction in GBM cell viability with nanoparticle treatment. Moreover, the authors reported that pRNA-3WJ-RNP treatment increased tumor suppressor PTEN and PDCD4 expression levels, two essential miR-21-regulated target proteins. Thus, a nanoparticle delivery system for A21 has been established.

Although not for GBM applications, it is noteworthy to discuss work done by the Yin group [126]. The group reported targeted delivery of A21 using RNA nanoparticles modified with RNA aptamers targeting CD133 proteins, a commonly believed cancer stem cell marker. Like Croce's group, A21 LNAs were incorporated into pRNA-3WJ-RNPs. pRNA-3WJ-RNPs were measured as 10.71 ± 2.846 nm in size with a zeta potential of -25.3 ± 10.8 mV. Upon pRNA-3WJ-RNP treatment in MDA-MB-231 triple-breast cancer cells, the authors reported increased miR-21 inhibition. Moreover, as in the

Croce study, PDCD4 and PTEN expression were significantly increased upon A21 delivery, verifying the intended result of miR-21 inhibition. Together, these studies support A21 as a viable resource for generating new and novel nanoparticle systems for GBM applications.

While the discussed results support the use of AS1411 and A21 in nanoparticle designs for GBM applications, it is essential to note that nanoparticle production is complex and minor alterations in their synthesis affect their biological and pharmacological activity. Therefore, the choice of nanoparticle type dictates the synthesis parameters and processing of incorporated therapeutics. Once determined, the nanoparticle system must be optimized to produce maximal anti-cancer effects effectively and efficiently. Several nanoparticle systems highlighted thus far have gained advantages against GBM incorporating AS1411 and miRNA inhibitors. However, gold nanoparticles (GNPs) have unique functional properties that allow efficient use in various medical applications, including drug delivery [132].

1.6 Gold Nanoparticles

GNPs have been used since Faulk and Taylor [133] first described antibody conjugation to gold (Au) in 1971. Multiple biomolecules have been used to functionalize GNP surfaces for genomics, biosensors, bioimaging, and targeted delivery of drugs, DNA, and antigens for therapeutic use [134]. GNPs are a popular choice of delivery method due to numerous advantages, including tunable surface chemistries, the ability to alter the size of the GNPs, and increased surface-to-volume ratios compared to larger-scaled objects [135-137]. These advantages of GNPs allow for a diverse range of therapies to be delivered rapidly to targeted areas of the body, internalization into cells through several endocytosis mechanisms, and reductions in therapeutic dosages due to the increased localized concentrations of drugs coated to the nanoparticle surface. Thus, GNP-based nanoparticle systems are commonly evaluated for delivering cancer therapies and have tremendous potential for their applications [138].

GNP surfaces can be easily tuned by conjugating molecules containing a thiol (SH) functional group. The chemistry behind SH groups and GNP surfaces is highly predictable and well characterized, with bond strengths approaching those of covalent bonds [136, 139, 140]. Suppose a bifunctional linker molecule (containing both an SH and a second functional group) is used. In that case, a second molecule, such as a biomolecule of interest, can be attached to the GNP/linker construct. A standard method of achieving bioconjugation to bifunctional linkers in aqueous systems is ester-bond coupling using 1-ethyl-3-(3-dimethyl aminopropyl) carbodiimide hydrochloride (EDC) with N-hydroysulfosuccinimde (Sulfo-NHS). This combination of reactants efficiently activates carboxylic acid functional groups to facilitate coupling reactions to amine or alcohol moieties on biomolecules. This technique has been effectively used in GNP design to generate systems with diverse surface functionalities [141-144].

While the term GNP incorporates a wide variety of shapes, sizes, and surface ligands, their action against tumors and tumor cells can be fine-tuned by altering the physicochemical characteristics of the nanoparticles. The shape of GNPs, spherical or non-spherical, affects their accumulation in tumor cells and circulation in the blood [145]. The most effective hydrodynamic diameter for increasing circulation times and achieving effective delivery at an intended target tissue appears to be between 10 and 100 nm—with an optimal near 20 nm [145]. The surface charge (*i.e.*, zeta potential) of GNPs affects their interaction with surrounding cells within the tumor microenvironment. Neutral and anionically charged particles display the highest cellular internalization via endocytosis. Depending on the conjugated ligand, type of cells, and the type of proteins and lipids involved, endocytosis is achieved through phagocytosis, clathrin-mediated endocytosis, caveolin-mediated endocytosis, clathrin/caveolae-independent endocytosis, or micropinocytosis [146].

Coating GNPs with various molecules further affects their size, charge, endocytosis route, and drug delivery efficiency. Conjugation of therapeutics to the nanoparticle surface can allow for faster delivery of the desired drug to the site of action, longer permeance in surrounding tissues with decreased deactivation, lower effective doses needed to be delivered, and lower associated toxicities compared to the stand-alone drug [147]. Delivery of therapeutics selectively to diseased tissue (*i.e*, malignant cells) can be achieved by conjugating molecules to the surface of the GNP that have high binding affinities to specific receptors overexpressed on cancerous cells.

There are currently thousands of GNP applications for cancer detection and treatment [148]. The use of GNPs for cancer research has increased since 1999, with over 90,000 articles published about their applications (**Figure 1-1**). Numerous chemotherapeutic agents have been conjugated to GNP surfaces, such as paclitaxel [149], docetaxel [150], and doxorubicin [151-153] to treat various cancers, including breast, ovarian, lung, cervical, esophageal, head and neck, stomach, prostate, bladder, and leukemia. Moreover, the use of GNPs to deliver DNA or RNA-based therapeutics has seen a tremendous increase in recent years. GNPs are highly suited to delivering these therapeutics due to the possibility of multifunctionalization of the GNP, allowing for the delivery of multiple synergistic anticancer agents. One previously discussed oligonucleotide cancer therapeutic, AS1411, has gained interest in designing multifunctional GNPs for GBM applications due to its nucleolin targeting abilities.

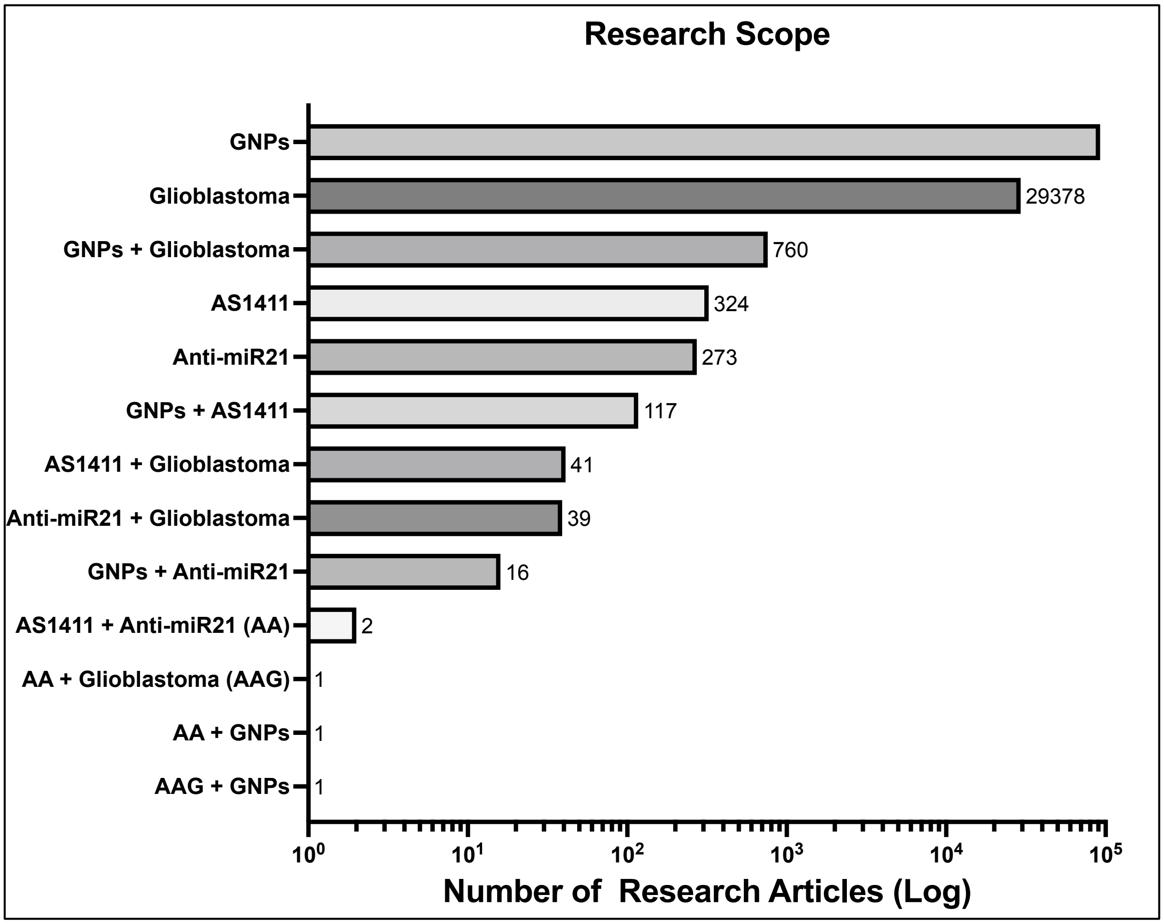

Figure 1-1: Research Scope of Research Articles about GNPs, AS1411, and A21 for GBM Applications since 1999. Source: www.sciencedirect.com

1.7 GNPs Conjugated with AS1411 or A21 Oligonucleotides for GBM Applications

Within the timeframe of reported articles on GNPs in Figure 1-1, the use of GNPs for GBM applications has begun to appear, but at only a fraction (0.62%) of the published articles. However, examining the scope of AS1411 and A21 oligonucleotides in the same timeframe (**Figure 1-1**), it becomes evident that they are increasingly relevant in the literature, with 324 and 273 articles published, respectively.

To date, AS1411 has been used in conjunction with GNPs to explore the bioactive effects of AS1411 in breast cancer [110, 154-163], colon cancer [164], lung cancer [165-167], leukemia [168, 169], brain cancer [95, 110, 166], pancreatic cancer [170], and for general use in cancer applications [171]. In addition, conjugated GNPs have been used to investigate the nucleolin targeting behavior of AS1411 [154, 161, 163, 170], deliver anti-cancer therapeutics [95, 110, 155, 165-169], image cancer cells [110, 156, 160], enable photodynamic therapy [158, 159, 164], and provide utility to biosensors [157, 162, 171].

Utilizing GNPs with AS1411 for GBM applications has focused on either using conjugated AS1411 as an anti-GBM treatment or using the nucleolin-targeting ability of AS1411 to deliver additional anti-cancer therapeutics (*e.g.*, 5-fluorouracil or doxorubicin). In 2016, the Chen group utilized gold nanoclusters conjugated with AS1411 and cyclic arginyl glycyl aspartic acid (cRGD, a cellular and tissue level targeting ligand) combined with immobilized doxorubicin to create a dual targeting therapy for tumor imaging and tissue therapy [110]. The nanoclusters were reported to be 3.06 ± 0.87 nm in core size and had a zeta potential of -17.76 ± 0.91 mV, indicating small and stable particles. In U-87 MG cells, a 75% decrease in cell viability, as measured by MTT assay, in nanocluster-treated cells at 12.5 ug/mL effective doxorubicin concentration (AS1411 concentration unknown) was reported. While promising, the proposed design was neither optimized for GBM specifically nor clinically translational (as TMZ is the standard chemotherapy for GBM). However, this report provided the foundation and motivation to use AS1411 and GNP-based designs for creating new and novel GBM therapies.

Additional studies have shown the promising potential of AS1411 for use in GBM therapies. The Wang group produced plant-derived GNPs conjugated with AS1411 and anti-cancer proteins that showed ~ 90% inhibition of LN229 GBM cell line viability at a 1000 ug/mL GNP concentration [166]. Moreover, the Sathiyaseelan group produced GNPs carrying doxorubicin and 5-fluorouracil (5FU) within a pH-responsive polymer for GBM applications [95]. This combined approach, designed to release the drug payload in the low pH of endo-lysosomes upon internalization, proved to be effective with concentration-dependent cytotoxicity of AS1411-DOX-5FU loaded GNPs showing a 75% decrease in LN229 cell viability with as little as 10 µg/mL GNPs (AS1411 concentration unknown from reported results). This treatment also increased LN229 cell apoptosis, as measured by flow cytometry.

A21 oligonucleotides have mainly been used to study the downstream effects of modulating intracellular miR-21 expression. As a result, their application with GNPs is sparse compared to those involving GNPs and AS1411. Of the 16 articles presented in **Figure 1-1** on GNPs combined with A21, only one directly uses GNPs combined with A21 oligonucleotides for an anti-cancer application. The Bae group first reported directly using A21 conjugated to GNPs [172]. They described a 13 nm GNP system for delivering A21 to HeLa cervical carcinoma cells. An increase in PDCD4, a downstream target of miR-21, was noted, indicating the ability of their GNP system to deliver functional A21 oligonucleotides. This is the first article to discuss the potential of GNPs and A21 together. But—like the other GNP syntheses—the group neither sufficiently optimized the synthesis for its intended use nor fully characterized the bioactivity of the GNP-delivered A21. Notably, none of the published works using A21 oligonucleotides involved have explored using the safe and effective nucleolin-targeting and anti-cancer ability of AS1411 in tandem with A21 for cancer or GBM applications. Utilizing AS1411 and A21 oligonucleotides with GNPs could provide a synergistic advantage in treating GBM. Cancer targeting/therapeutic effects conferred by AS1411 can potentially make A21 more effective. Meanwhile, the specific anti-GBM behavior of A21 could enhance the anti-GBM activity of AS1411. Recent advancements in GNPs at UofL and other universities have opened the idea of exploring such a multi-faceted design for GBM applications.

1.8 Advancements of GNPs in Cancer and GBM

The O'Toole and Bates groups have researched GNPs for cancer applications for over a decade at UofL. The focus of the work done thus far has shown the feasibility of 5 nm GNPs conjugated with AS1411 for breast cancer therapy. Results showed profound anti-proliferative effects of AS1411-modified GNPs in breast cancer cell lines and a dramatic decrease in the IC_{50} required to achieve therapeutic effect compared to stand-alone, unconjugated AS1411 treatments [52]. Most interestingly, when the delivery of 5 nm AS1411 conjugated GNPs was investigated in xenograft *in vivo* nude mice models, analyses of GNP-AS1411 treated tissues showed GNP concentrations present in the brain. With this observation, and given what is known about AS1411, oligonucleotide therapies, GBM, and GNPs—it was postulated that similar GNPs could be developed as a new AS1411-based therapy for GBM treatment.

Other groups have presented promising results with GNPs for GBM applications. For example, the Mirkin group has reported the successful delivery of functional GNPs to GBM tumors *in vivo* [173]. The GNPs, known as spherical nucleic acids (SNAs), are designed with densely packed, small interfering RNA (siRNA) oligonucleotides covering a solid Au core [174, 175]. SNAs were developed with siRNA against the oncogene Bcl2L12, frequently amplified in GBM. SNAs were able to accumulate within U-87 MG cells and down-regulate Bcl2L12 expression. Most importantly, SNAs could collect within intracranial GBM tumors 1.8-fold higher than sham tumors within *in vivo* mouse models of GBM. Furthermore, the ability of SNAs to down-regulate Bcl2L12 expression *in vivo* by 40% benefited mice by releasing tumor burden, as reported by an approximately 3-fold decrease in measured average tumor weight. Thus, these data from the O'Toole, Bates, and Mirkin groups imply confidence in the ability of GNPs to have practical applications in developing new GNP-based GBM therapies. Therefore, this dissertation investigates the feasibility of incorporating AS1411 targeted delivery and A21 oligonucleotide therapy onto potentially BBB-surpassing 4 nm GNPs.

1.9 Motivation and Hypothesis

The clinical motivation behind the proposed research stems from the fact that advancements in GBM treatments have not progressed as well as other cancer treatments. Because of this, recurrence is common and is driven by the cellular and genetic heterogeneity of GBM and the presence of the BBB. Preliminary results from section 1.8 detailing the anti-cancer and BBB passing ability of oligonucleotide-modified GNPs provide the research motivation behind the work discussed in this dissertation. Moreover, the ability of AS1411 and A21 oligonucleotides to influence GBM cell signaling survival mechanisms on the genetic level gives hope in decreasing the recurrence of GBM tumors. Given the results showing the potential of 5 nm GNPs to surpass the BBB, **a GBM-targeted nanotherapy combining GNPs, PEG, AS1411, and A21 was hypothesized to promote anti-GBM effects on U-87 MG cells and to gain access past the BBB *in vivo* to confer benefits of the anti-GBM bioactivity of the proposed nanoparticles.**

1.10 Developing GNPs for GBM at UofL

Developing GNPs conjugated with PEG, AS1411, and A21 oligonucleotides focused on generating a bioactive GNP against GBM. Each molecule (AS1411 and A21) conjugated to GNPs was selected due to their established bioactivity or to literature precedence for their bioactivity. A PEG linker molecule was used to allow for the conjugation of A21 oligonucleotides to the GNP. PEG is a clinically approved linker known to confer stability to a particle system via protection from adsorbing proteins [176]. The combination of PEG, AS1411, and A21 onto GNPs was evaluated with three aims. GNPs were first surface modified with AS1411 and PEG molecules. The resulting PEG/AS1411 GNPs were then assessed for selecting an optimal anti-GBM GNP by investigating the anti-GBM effects defined by decreases in metabolic ability, alterations to normal U-87 MG morphology, and decreases in growth of U-87 MG cells *in vitro* (Aim 1). Further modification of GNP-conjugated PEG molecules allowed for the attachment of A21 to the nanoparticle construct. These PEG/AS1411/A21 GNPs were then compared to PEG/AS1411 GNPs to evaluate the benefit, if any, of A21 addition. Comparisons were based on the proven anti-GBM activity from Aim 1 on U-87 MG cell metabolic ability, morphology, and growth. Downstream effects of PEG/AS1411/A21 GNPs on the expression of miR-21 transcripts and miR-21 associated proteins STAT3 and PTEN in U-87 MG cells were also used to verify the delivery of functional A21 (Aim 2). Representative GNPs from each aim were then investigated in an orthotopic nude mouse GBM model to establish the ability of GNPs to permeate the BBB and to compare benefits between PEG/AS1411 GNPs and PEG/AS1411/A21 GNPs (Aim 3).

1.11 Dissertation Organization

Chapter 1 has provided the background and literature necessary for understanding GBM and gives the reader sufficient detail to understand the techniques described in subsequent chapters involving the synthesis and *in vitro* or *in vivo* testing of oligonucleotide-based GNP systems. Chapter 2 details the specific synthesis and experimental protocols used to synthesize and evaluate the proposed GNP system. Chapter 3 focuses on synthesizing and selecting optimal PEG/AS1411 GNPs within U-87 MG *in vitro* models before further modifications with A21. Chapter 4 focuses on modifying the optimized particles from Chapter 3 with A21. This chapter compares their performance in U-87 MG *in vitro* models to that of the PEG/AS1411 GNPs. It evaluates the benefit of A21 addition by examining the effects on genetic and miR-21-associated protein expression. Chapter 5 examines the *in vivo* performance of representative GNPs from Chapters 3 and 4. Chapter 6 summarizes and concludes the research findings and suggests future directions.

CHAPTER 2

MATERIALS AND METHODS

2.1 Materials

2.1.1 Synthesis Materials

$HAuCl_4 \cdot 3H_2O$ was purchased from Alfa Aesar (Tewksbury, MA). Citric acid, trisodium salt ($Na_3C_6H_5O_7$), sodium borohydride ($NaBH_4$), dithiothreitol (DTT), and anhydrous sodium bicarbonate ($NaHCO_3$) were purchased from Sigma Aldrich (St. Louis, MO). Nanopure ultrapure water (Barnstead, resistivity of 18.2 MΩ-cm) was used for preparing all aqueous solutions. 10.0X phosphate buffered solution (pH 7.4) was purchased from Thermo Fisher Scientific (Waltham, MA). Hydrochloric acid (HCl) and nitric acid (HNO_3) were analytical grades and purchased from VWR (Radnor, PA). Aqua regia solution (3 parts HCl and 1 part HNO_3) was used to clean all glassware for GNP synthesis. Thiol Polyethylene Glycol-4-alcohol (SH-PEG-OH; Molecular Weight 210.3 g/mol; 95% purity) was purchased from BroadPharm (San Diego, CA) and prepared for use via company specifications. Oligonucleotides having a regular DNA backbone (phosphodiester), a 5'-Thiol C6 S-S modification (Thio-MC6-D), 5'-6T spacers (for AS1411 and CRO), and high-performance liquid chromatography purification were supplied by Integrated DNA Technologies (Coralville, IA). The DNA oligonucleotide sequences used (including 6-T spacer) were 5'-TTTTTTGGTGGTGGTGGTTGTGGTGGTGGTGGTTT (AS1411) and a control sequence 5'-TTTTTTCCTCCTCCTCCTTCTCCTCCTCCTCCTTT (CRO). Oligonucleotides having a 2'O-methyl modified RNA backbone, a 5'-Carboxy COOH2 modification, a 5'6U spacer, and RNAse-free high-performance liquid chromatography purification were also supplied by Integrated DNA Technologies. The RNA oligonucleotides sequences used (including 6-U spacer) were 5'-

UUUUUUUUCAACAUCAGUCUGAUAAGC (A21) and a control sequence of 5’-UUUUUUAUUCUUAAUAGUCACCGCAA (SCR21). In addition, 1-ethyl-3-(3-dimethyl aminopropyl) carbodiimide hydrochloride (EDC), N-hydrosulfosuccinimide (Sulfo-NHS), and 2-(N-morpholino) ethanesulfonic acid (MES) reagents were purchased from Thermo Scientific. Illustra NAP-25 DNA size exclusion chromatography gravity columns were acquired from GE Healthcare Life Sciences (Pittsburgh, PA). Amicon Ultra 15.0 ml centrifugal filters with Ultracel-30 (30000 molecular weight cutoff) were purchased from Merck Millipore (Billerica, MA). UV absorption spectra of nanoparticle formulations and oligos were measured with a UV Visible Spectrometer (Varian Cary 50 BIO UV, Agilent Technologies, Santa Clara, CA). Dynamic light scattering and zeta potential measurements were acquired on nanoparticle formulations using a NanoBrook Zeta PALS Zeta Potential Analyzer (Brookhaven Instruments, Holtsville, NY).

2.1.2 Cell Culture

U-87 MG GBM cancer cells were purchased from ATCC (Manassas, VA). Dulbecco's Modified Eagle Medium, Heat Inactivated Fetal Bovine Serum, 10X Trypsin, Penicillin/Streptomycin were purchased from Thermo Fisher Scientific. U-87 MG cells were subcultured in T25 or T75 sterile tissue culture-treated culture flasks from Corning Incorporated (Tewksbury, MA). For experimental studies, U-87 MG cells were passed into 6 or 96 well-sterile culture plates from VWR (Radnor, PA) for microscopy and metabolic studies, respectively.

2.1.3 Biological Assays

Metabolic activity of U-87 MG cells after GNP or control treatments was measured using (2,3-Bis-(Methoxy-4-Nitro-5-Sulfophenyl-2H-Tetrazolium-5-

Carboxanilide) (XTT) acquired from Biotium (Fremont, CA). Total U-87 MG miRNA was isolated from 6 well culture plates via RNeasy Mini Kit purchased from Qiagen (Germantown, MD). RNA content was measured using a Thermo Scientific (Waltham, MA) NanoDrop 2000 spectrophotometer. Complementary DNA libraries were created using Thermo Scientific's high-capacity cDNA reverse transcription kit. RT-qPCR cDNA libraries were made with hsa-mir-21 (000397) and RNU44 (001094) TaqMan assays purchased from Thermo Scientific. PCR tubes and 384 well plates were purchased from Genesee Scientific (El Cajon, CA). Micro RNA expression levels were quantified using Applied Biosystem's Viia7 Real-Time PCR System. Total U-87 MG protein production was measured via Pierce BCA Protein Assay Kit purchased from Thermo Scientific. Measured protein isolates collected from T75 cell culture flasks treated with radioimmunoprecipitation (RIPA) lysis buffer enhanced with Halt protease and phosphatase inhibitor cocktails (100X) purchased from Thermo Scientific. Treated cell flasks were scraped with cell scrapers. Protein samples were analyzed for specific protein content via protein separation within 10% SDS-PAGE gels cast with an 8% SDS stacking layer followed by protein transfer using PVDF/filter paper sandwiches, 0.2 um, purchased from Thermo Scientific. All equipment and buffers for western blots (MES SDS Running Buffer (1X), transfer buffer supplemented 20% methanol (1X), 1X TBS-tween 20 buffer, mini gel tank, mini blot module) were graciously given by Dr. Carolyn Klinge's lab. Western blots were imaged using a Licor Odyssey Classic Infrared Imager (Lincoln, NE). Primary antibodies used in western blot analyses included: rabbit monoclonal antibody to PTEN (D4,3) XP(R) (Cell Signaling),mouse monoclonal antibody to beta-actin (8H10D18) (Cell Signaling), and mouse monoclonal antibody to

STAT3 (124H6) (Cell Signaling). Secondary antibodies were purchased from Licor and were IRDye 800 CW Goat anti-Rabbit (926-32211) and IRDye 680 RD Goat anti-Mouse (926-68070).

2.1.4 *In vivo* Studies

Nude, three-week-old female mice were purchased from Charles River and housed in UofL's animal facilities. Carprofen (5 mg/kg), ketamine (50 mg/kg), and dexmedetomidine (0.5 mg/kg) used for implantation were acquired through UofL's Comparative Medicine Research Unit. Dr. Brian Williams and Dr. Norman Lehman from UofL provided stereotactic gear, bone wax, surgical instruments, and sutures. Insulin needles and alcohol pads were purchased from VWR (Radnor, PA).

2.2 Methods

2.2.1 PEG/AS1411 GNP Synthesis for Aim 1

4 nanometer (nm) citrate-capped GNPs were sterilely synthesized using previously reported protocols. [177, 178] Briefly, 5.0 mL of $Na_3C_6H_5O_7$ is added to 95.0 mL of sterile nanopure water. Then, 2.5 mL of $HAuCl_4 \cdot 3H_2O$ is added to the mixture and mixed for 18 seconds. At the 18-second mark, 3.0 mL $NaBH_4$ is added to allow GNP formation. This GNP mixture is allowed to stir at maximum speed for 2 hours and then conjugated with thiol-modified surface ligands via mixing of reagents. Thiol-modified AS1411 (SH-AS1411) contains disulfide linkages upon purchasing for storage and stability that were cleaved before conjugation via boiling the desired mixture of SH-AS1411, 1.0 M DTT, 0.25 M phosphate buffer (PB), and nanopure ultrapure water for 1 hour followed by cooling for another hour. SH-AS1411 was isolated from this boiled mixture via size exclusion chromatography using Illustra NAP-25 DNA gravity columns

and 0.1M PB as the eluent. SH-PEG alcohol (OH) was diluted in DMSO according to manufacturer specifications. Cleaved and purified SH-AS1411 and diluted SH-PEG-OH were then conjugated to GNPs in different ratios (see next paragraph), generating a two-component PEG/AS1411 GNP coating. The resulting particles were transferred to a physiological salt level through the stepwise addition of 10X phosphate-buffered saline (PBS) over 96 hours up to a total concentration of 1X, followed by sonication in a water bath for 10 minutes at each PBS addition. After these 96 hours, GNPs were centrifuged at 13,500 g for 20 minutes, followed by a triplicate 1X-PBS washing and re-centrifugation after each wash to remove non-conjugated components. A representative illustration of synthesized PEG/AS1411 GNPs is presented in **Figure 2-1**.

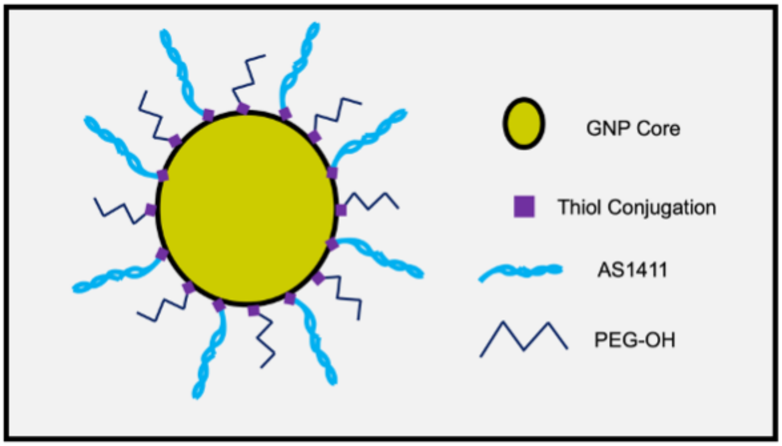

Figure 2-1: Visual Description of PEG/AS1411-GNPs

Multiple PEG/AS1411 GNP formulations were synthesized that differed by their loading ratios of PEG and AS1411. Maximum possible loading of PEG and AS1411 onto GNPs was held constant at 12 times (expressed as 12X) the concentration of Au present within the colloidal solution, as measured by UV-VIS spectrometry. [135] This 12X loading was divided up into multiple ratios of PEG/AS1411 and resulted in the following experimental loading ratios presented in **Figure 2-2**. For formulations below the maximum of 12X AS1411, PEG was introduced to fulfill the 12X maximum loading requirements.

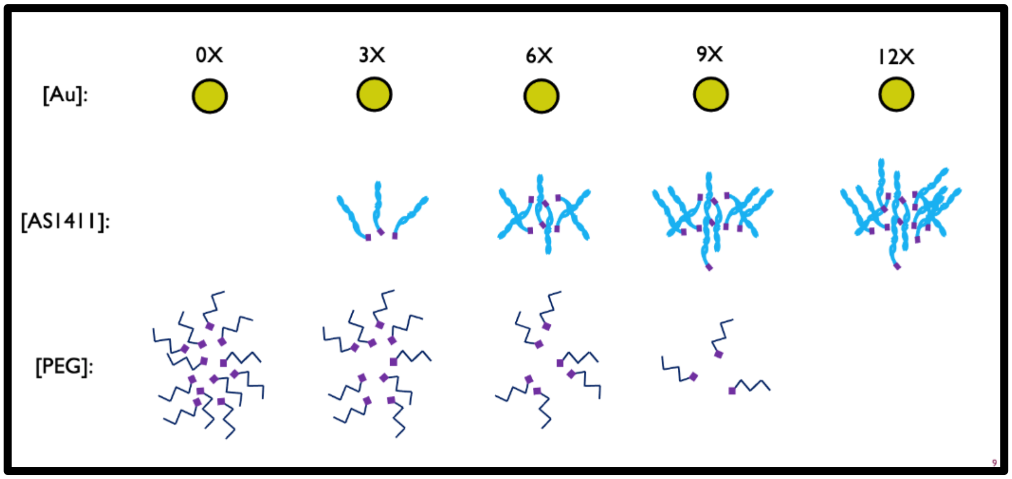

Figure 2-2: Visual Description of PEG/AS1411 Ratios Tested

2.2.2 Synthesis of PEG/AS1411/A21 GNPs for Aim 2

AS1411/PEG GNPs were modified further by conjugating a GBM-specific miRNA inhibitor, A21. Briefly, necessary volumes of miRNA inhibitor needed were activated in MES buffer according to company recommendations in a sterile solution of EDC (introduced at ten times the number of moles of A21). This mixture of EDC/MES/A21 was rotisserie mixed for 30 minutes at room temperature. Next, sulfo-NHS (introduced at 2.5 times the number of moles of EDC) was introduced to the EDC/MES/A21 mixture, and the reaction volume was raised to 0.5 mL with additional MES buffer. PEG/AS1411 GNPs were then introduced in their necessary volume. Then, the reaction volume was increased to 1.5 mL using 1X-PBS and rotisserie mixed for 72 hours at room temperature. After mixing, PEG/AS1411/A21 GNPs were centrifuged at 13,500 g for 20 minutes, followed by a triplicate 1X-PBS washing and re-centrifugation after each wash to remove non-conjugated components. A representative illustration of synthesized PEG/AS1411/A21 GNPs is presented in **Figure 2-3**. Different molar amounts of A21 and PEG present on PEG/AS1411 GNPs were used to acquire the PEG/AS1411/A21 GNPs represented in **Figure 2-4.**

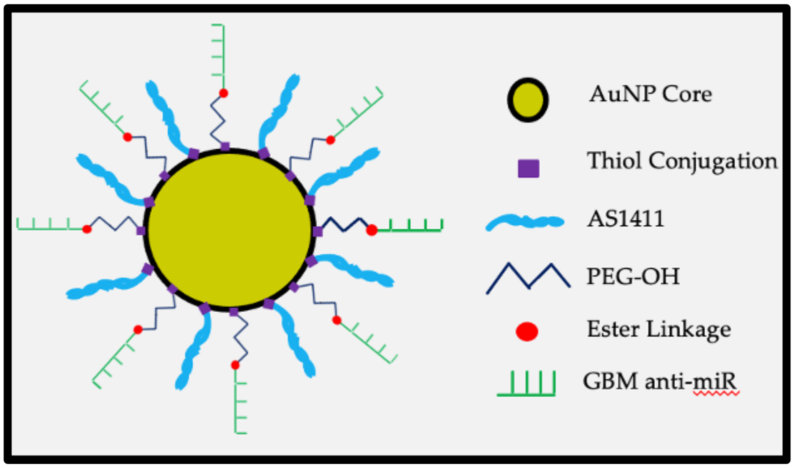

Figure 2-3: Visual description of PEG/AS1411/A21 GNPs

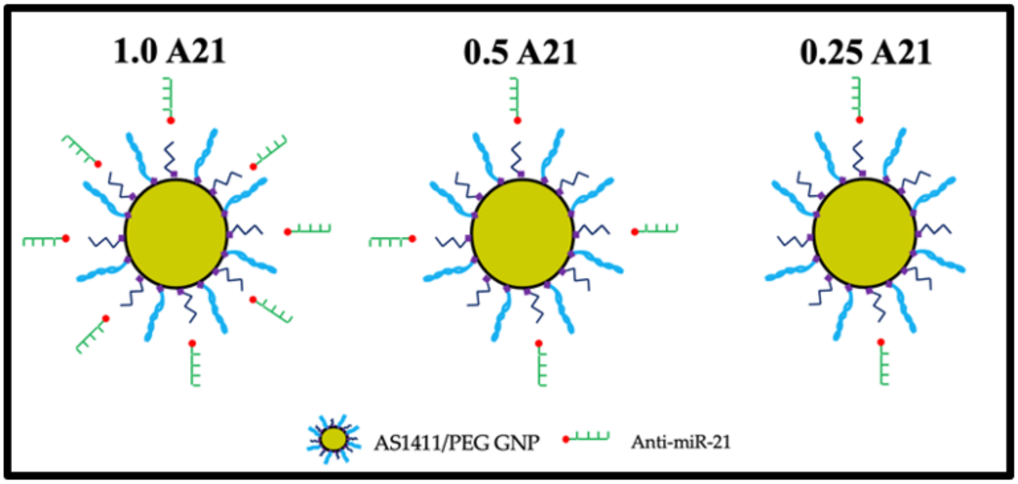

Figure 2-4: Visual Description of PEG/AS1411/A21 GNP ratios synthesized

2.2.3 GNP Characterization

GNP hydrodynamic diameter (measured in nanometers), zeta potential (measured in millivolts), and PDI (unitless) were measured for three independent syntheses of all GNPs synthesized using DLS and UV-VIS. Changes in absorption spectra were recorded on a Varian Cary 50 BIO UV (Agilent Technologies, Santa Clara, CA) spectrometer. UV-VIS spectra verified AS1411 conjugations for PEG/AS1411 GNPs and investigated A21 modification for PEG/AS1411/A21 GNPs. AS1411 loading was evaluated for each PEG/AS1411 GNP formulation (n=3 for each PEG/AS1411 GNP formulation with AS1411 present). Verification of loading was completed via a 72-hour cleavage of AS1411 from GNPs by treatment in a mixture of 1X PBS with 1.0 M DTT followed by UV-VIS measurement of cleaved and isolated AS1411 (via Illustra NAP-25 DNA gravity columns with 0.1 M PB as the eluent). Moles of AS1411 was calculated from the molar absorptivity provided by the manufacturer (IDT) using UV-VIS measurements with Beer's Law and compared to moles of Au present in colloidal solution to determine an average number of AS1411 per GNP.

2.2.4 Cell Culture

U-87 MG cells were cultured in Dulbecco's Modified Eagle's Medium with 10% heat-inactivated fetal bovine serum and 1% penicillin/streptomycin. All subcultures in culture flasks were passaged using 0.25% Trypsin and seeded at a minimum density of 5000 cells/cm^2.

2.2.5 Metabolic Activity and Specificity Studies

XTT assays measured the metabolic activity of U-87 MG cells exposed to PEG/AS1411 GNPs, PEG/AS1411/A21 GNPs, or control treatments. The specificity of

PEG/AS1411 GNPs was validated using XTT assays with U-87 MG cells exposed to PEG/AS1411 GNPs or PEG/CRO GNPs (CRO is a specificity control oligonucleotide for AS1411). Wells with cells and control wells (no U-87 MG cells) in 96 well plates were incubated with all GNPs from Aims 1 and 2 ranging from 0 - 5 micromolar (μM) AS1411 concentrations or control treatments (n=3 independent replicates for GNP treatments, n=6 independent replicates for control treatments, n=5 independent replicates for all treatment groups in specificity studies, seeding density of 3500 cells/cm.^{2}). Control treatments for all XTT assays performed were either no treatment or 10 μM concentration of standalone (unbound to GNP) AS1411. Based on the timing of AS1411 bioactivity, all treatments were incubated for 72 hours with no media changes. **Tables 2-1 through 2-4** detail the relationship between equivalent AS1411 concentration treatment and total GNP concentrations for all PEG/AS1411 GNP, PEG/CRO GNP, and PEG/AS1411/A21 GNP treatments exposed to U-87 MG cells.

XTT absorbance data was obtained from a Molecular Devices SpectraMax M2 Spectrometer running SoftMaxPro 7.0 software. GNP interference was corrected by subtracting the average absorbance values in control wells (GNP treatments with no U-87 MG cells; n=3 independent replicates) from those in treatment wells (GNP treatments with U-87 MG cells). This correction was also completed for control treatments using the appropriate treatment and control wells.

Statistical analyses were completed for all XTTs using two-way ANOVA analyses with Bonferroni post-hoc tests (α=0.05). Each test examined the main effects of GNP type, AS1411 treatment concentration, and their interactions on the metabolic activity of U-87 MG cells. The results discussed are the main effects of GNP type and

AS1411 concentrations on U-87 MG cell metabolic activity. It is noteworthy to mention that the sample sizes of GNP treatments would ideally be n=5. However, restrictions on supplies and budgets from the funding partners limited GNP treatments to an n=3 for all studies.

Table 2-1

Average GNP Concentration of PEG/AS1411 GNPs Correlated to AS1411 Concentration

Average GNP Concentration					
	GNP Particle Type Concentration (nM)				
AS1411 Treatment Concentration (uM)	**0X**	**3X**	**6X**	**9X**	**12X**
0.25	4.21	4.21	3.16	1.58	0.97
0.5	8.39	8.39	6.32	3.16	1.94
1.0	16.82	16.82	12.63	6.32	3.89
2.5	42.08	42.08	31.58	15.79	9.72
5.0	84.37	84.37	63.15	31.58	19.43

Table 2-2

Average GNP Concentration of PEG/AS1411 and PEG/CRO GNPs Correlated to Oligonucleotide Concentration

Average GNP Concentration		
	GNP Particle Type Concentration (nM)	
Oligonucleotide Concentration (uM)	**9X AS1411**	**9X CRO**
0.12	0.76	0.67
0.24	1.52	1.35
0.4	2.27	2.02
0.48	3.03	2.69
0.6	3.79	3.37
1.0	6.32	5.61
1.2	7.58	6.74
2.0	12.63	11.23
2.4	15.16	13.47
4.8	30.31	26.94
5.0	31.58	28.07

Table 2-3

Average GNP Concentration of PEG/AS1411/A21 GNPs Correlated to AS1411 Concentration

Average GNP Concentration			
	GNP Particle Type Concentration (nM)		
AS1411 Treatment Concentration (uM)	**1.0 A21**	**0.5 A21**	**0.25 A21**
0.25	1.58	1.58	1.58
0.5	3.16	3.16	3.16
1.0	6.32	6.32	6.32
2.0	15.79	15.79	15.79
5.0	31.58	31.58	31.58

Table 2-4

Expected Average A21 Content of PEG/AS1411/A21 GNPs Correlated to AS1411 Concentration

Average GNP Concentration			
	GNP Particle Type Concentration (nM)		
AS1411 Treatment Concentration (uM)	**1.0 A21**	**0.5 A21**	**0.25 A21**
0.25	83.33	41.67	20.83
0.5	166.67	83.33	41.67
1.0	333.33	166.67	83.33
2.0	666.67	333.33	166.67
5.0	1666.67	833.33	416.67

2.2.6 Microscopy Studies

Brightfield images were collected 72 hours post-treatment (n=3 images per condition). A Nikon TE200 Epiflorescent microscope (Melville, NY) with a Coolsnap HQ CCD camera (Roper, Duluth, GA) enabled with NIS Elements software captured representative 10X brightfield images of U-87 MG cells treated with GNP formulations from both aims and their controls 72 hours post-treatment. Representative images were selected for respective figures.

2.2.7 Growth Analysis

Cell counts were measured 72 hours post-treatment and compared to an initial seeding amount. U-87 MG cells were seeded at 90,000 cells per well and incubated with optimal formulations of PEG/AS1411 GNPs and PEG/CRO GNPs (n=3 independent replicates for all GNP treatments) from Aim 1 in three AS1411/CRO concentrations (1, 2, and 5 μM) for 72 hours with no media changes. Control cells were treated with no treatment or 10 μM standalone (unbound to GNP) AS1411 (n=3 independent replicates for both controls). Cell counts were obtained by collecting the cells after the 72-hour incubation period by washing plates with 1X PBS and treating them with 0.5% Trypsin for 5 minutes. Manual counts using a hemocytometer were completed to acquire cell numbers and then compared to the initial seeding density.

The same experimental setup and treatment protocol was completed to compare the anti-GBM growth effects of optimal PEG/AS1411 GNPs in U-87 MG cells to those of the different formulations of PEG/AS1411/A21 GNPs (n=3 independent replicates). These comparisons additionally included Lipofectamine transfected U-87 MG cells with standalone (unbound to GNPs) A21 as an additional control. Transfection of U-87 MG cells was completed by following the recommended transfection protocol (n=3 independent replicates for A21 transfected U-87 MG cells).

Cell count data were acquired across 6 identical growth experiments with NT controls in each experiment. Each experiment differed by its GNP treatment. Cell counts for each experiment were normalized to the initial seeding density and then normalized to each experimental NT control. Overall cell count data were normalized to the average NT control across all growth experiments. Statistical analyses were completed for all growth analyses using two-way ANOVA analyses with Bonferroni post-hoc tests (α=0.05).

2.2.8 miRNA Collection and Quantification

The cells used for determining growth analyses were also used for miRNA collection. Total miRNA was collected via an RNEasy Mini Kit following the recommended protocol from the company. miRNA samples were stored in RNAse-free water and measured for RNA concentration via NanoDrop measurement.

2.2.9 RT-qPCR and Analysis

Total miRNAs collected from U-87 MG cells were used for RT-qPCR measurements. 200 ng of miRNA were collected from each sample tested and used to generate a cDNA library using the TaqMan® MicroRNA Reverse Transcription Kit and the High-Capacity cDNA Reverse Transcription Kit for RNA (both from ThermoFisher) following the recommended company protocol. Quantitative real-time PCR (RT-qPCR) used TaqMan primers specific for the target gene (human miR-21) or the control gene (RNU44; TaqMan assays were purchased from ThermoFisher). cDNA libraries prepared with TaqMan primers were diluted in nuclease-free water and pipetted into 384 well plates (n=3 technical replicates for each sample). RT-qPCR data were collected on a Viaa 7 Real-time PCR system. The comparative threshold cycle (CT) method was used to determine ΔCT, ΔΔCT, and fold-change, log 2, relative to a small-nucleolar control gene (RNU44) [179, 180]. Statistical analyses were completed for all RT-qPCR studies using two-way ANOVA analyses with Bonferroni post-hoc tests (α=0.05).

2.2.10 Protein Collection and Quantification

Expression of miR-21 associated proteins STAT3 and PTEN in PEG/AS1411/A21 GNP-treated U-87 MG cells were investigated using western blot analysis and compared to those of PEG/AS1411 GNP-treated and control-treated U-87 MG cells (n=3 independent replicates for all treatment conditions). 1.4 x 10^6 cells were seeded in a T75 flask and incubated with GNPs from both aims at two concentrations (1 and 5 µM equivalent AS1411 concentrations) for 72 hours with no media changes. Control cells were treated with either standalone 10 µM AS1411 (unbound to GNP), no treatment, or Lipofectamine transfection of U-87 MG cells with standalone A21 (unbound to GNP). After 72 hours, flasks were washed with cold 1X PBS and placed on ice. Flasks were treated with 200 uL of RIPA buffer supplemented with 1X protease and phosphatase inhibitors. This mixture was allowed to sit on ice for 5 minutes with manual agitation every minute to distribute the buffer. Protein isolates were collected via scraping with cell scrapers in a 2.0 mL vial. Samples were then frozen overnight to induce better extraction of proteins. After one freeze and thaw cycle, protein concentrations were measured by BCA assays (5 uL of isolated samples measured in 200 uL of BCA working reagent; n=2 technical replicates for each sample). Overall protein concentration was determined by comparison to a standard curve of bovine serum albumin protein supplied by the company.

2.2.11 Western Blot Collection, Imaging, and Analysis

Western blot analysis used 10% mini, 15-well, SDS-PAGE gels made with the Bio-Rad mini-PROTEAN tetra hand cast system with an 8% stacking layer. Volumes from protein samples representing 15 micrograms of protein were mixed with a 1:1

volume of 2X Laemmli loading buffer (65.8 mM Tris-HCl, pH 6.8, 2.1% SDS, 26.3% (w/v) glycerol, 0.01% bromophenol blue) and were boiled for 5 minutes. Protein samples were mixed, and 20 µL of each sample was pipetted into gel wells. Samples were separated for 30 minutes at 100V and then for 2 additional hours at 75V. Completed gels were then transferred with a blot transfer module using Bio-Rad's recommended arrangement of sponges, filter paper, PVDF membrane, and gel. Transfers were conducted at 4ºC in 1X transfer buffer supplemented with 20% methanol for 60 minutes at 100 V. Transferred blots were washed three times with 1X-TBST and blocked for 1 hour at room temperature using Licor Intercept blocking buffer.

Blocked blots were treated with PTEN primary antibody (1:1000) at 4 ºC overnight and washed thrice with 1X-TBST. Washed blots were treated with a 1:1000 dilution of appropriate secondary antibody (1:10000) for 1 hour at room temperature and then rewashed three times with 1X-TBST and DI water. Antibody-stained blots were then imaged using a Licor Odyssey at two wavelengths (685 and 785 nm). Ponceau S staining was completed after imaging for verification of protein loading. Blots were then treated with stripping buffer (31.25 mL of 1M Tris, pH = 6.7, 10.0 g SDS, and 3.5 mL of β-mercaptoethanol) to remove all conjugated antibodies and Ponceau stain. Next, blots were reprobed for ß-actin (1:1000) for 45 minutes at room temperature and re-probed with appropriate secondary antibodies (1:10000) with repeated washing steps. Blots were then re-imaged with the Licor Odyssey, re-stripped, and re-probed with STAT3 antibodies (1:1000) overnight at 4ºC, with the same washing, incubation with appropriate secondary antibody (1:10000), and imaging steps as before.

Images acquired were analyzed using ImageJ for densitometry. The band density measurements were first normalized to the density of Ponceau-S staining in the range of molecular weight (100 – 37 kDa) of the proteins of interest (STAT3: ~ 88 kDa, β-actin: ~ 42 kDa, and PTEN: ~ 47 kDa). Ponceau-S normalized densitometry measurements were then normalized to the densitometry measurements of β-actin control bands in each lane, producing a relative protein expression. Reported values are average relative protein expressions further normalized to non-treated controls. Statistical analyses were completed for all western blot analyses using one-way ANOVA analyses with Bonferroni post-hoc tests (α=0.05).

2.2.12 Motility Analyses

The motility rate of PEG/AS1411 GNP-treated U-87 MG cells was measured and compared to those of PEG/AS1411/A21 GNP-treated U-87 MG cells. 1,000 U-87 MG cells per well were cultured in 6 well plates and incubated with optimal PEG/AS1411 GNPs from Aim 1 and the 1.0 A21 formulation of PEG/AS1411/A21 GNP from Aim 2 at 1 μM equivalent AS1411 concentration for 72 hours with no media changes (n=3 independent replicates). Control cells received no treatment (n=3 independent replicates). For each replicate, imagining locations (5 per well) within wells were selected to highlight sparse density to aid the analysis of cells that were only moving and neither dividing nor contacting other cells. Each location in each well was imaged for 72 hours. Images of live cells were taken every 15 minutes using a Nikon TE2000 Epifluorescent microscope (10X objective) fitted with a live cell chamber. 25 cells were chosen from each location set (across all 5 locations) within a 6-hour window at 48-54 hours post-treatment with GNPs. This time falls within the established timeline of AS1411 activity

[93, 181]. It ensured an appropriate number of cells analyzed (as the times after 54 hours began to have fewer non-contacting and non-dividing cells).

U-87 MG cell movement was followed for each selected cell using ImageJ software with the tracking function. XY-coordinates reported from ImageJ were placed into an Excel template to determine the motility rates of U-87 MG cells over time. Statistical analyses were completed for all motility analyses using one-way ANOVA analyses with Bonferroni post-hoc tests (a=0.05).

2.2.13 *In vivo* GBM Implantation

UofL's Institutional Animal Care and Use Committee approved all animal study procedures. Nine 3-week-old female nude mice were delivered to the animal housing facilities and acclimated for one week before intracranial glioma implantation. On day 7 of being housed, mice were weighed, ear tagged for surgical records, and *s.c* injected with carprofen (5 mg/kg) and anesthetized *i.p* with a mixture of ketamine (50 mg/kg) and dexmedetomidine (0.5 mg/kg). After anesthesia, mice were fitted into stereotactic frames (David Kopf Instruments). Cranial incisions were made lateral to the midline, and 1.0 mm burr holes were drilled approximately 2.5 mm medially from the bregma. A cell suspension of 100K Luciferase-modified U-87 MG cells in 2 uL was then deposited into the right caudate nucleus at a depth of 3 mm from the dura. Burr holes were then filled with bone wax, and the incision was closed with 4-0 vinyl sutures. Mice were then placed on a warm heating pad to come out of anesthesia before being placed into cages and housed in the animal facilities.

2.2.14 *In vivo* GNP Treatments

Subcutaneous injections of carprofen (5 mg/kg) were given once a day for two days after surgery to mitigate residual pain. Tumors were allowed to grow for 2 weeks with regular check-ins to evaluate overall health. Tumor growth was assessed via Luciferin-based imaging on days 9 and 11 post-tumor implantations. Each day, mice received a 150 mg Luciferin/kg body weight dose and were immediately imaged using a Biospace Lab Photon Imager within UofL's animal facility. Based on Luciferin uptake and processing by Luciferase-modified U-87 MG cells, bioluminescence was then measured in photon counts. Therefore, the level of photon counts present on each imaging day can be used to evaluate tumor formation and progression throughout the study. Once tumors were confirmed, *i.p* injections of GNP treatments representing a 1 mg/kg dose of AS1411 and 1X-PBS-treated controls (n=3 mice per group) were given daily for 12 days. GNP treatments were the optimal PEG/AS1411 GNPs from Aim 1 and representative PEG/AS1411/A21 GNPs from Aim 2. Imagining was completed during the treatment window on days 11 and 22 post-tumor implantations. Mice were followed out for a maximum of 67 days post-tumor implantation and euthanized once any signs of neurological distress were present or until day 67 was reached. To investigate tumor progression benefits conferred to mice because of the EPR effect of GNPs, imaging was also completed on days 28 and 36 post-tumor implantations.

To accurately conduct this animal study, sample size power analysis was completed before animal studies. This analysis was based on previous animal studies in the Bates group [7], which showed differences in tumor volumes within *in vivo* models of breast cancer on day 12 post-GNP treatment. A suggested sample size of n=7 mice per group was established to establish a power of 80% using the averages and standard deviations associated with these data. However, due to limitations on the size of the study conferred by the funding partner, this dissertation addresses n=3 mice per group.

Reported average photon counts in the tumor area across imaging days were examined. Statistical analyses were completed on tumor progression using one-way ANOVA analyses with Bonferroni post-hoc tests ($\alpha=0.05$). In addition, the survival of each mouse within the study was recorded, and statistical analysis on the probability of survival was completed using Kaplan-Meier survival analysis ($\alpha=0.05$).

2.2.15 Biodistribution of GNP Treatments *in vivo*

Euthanized mice were collected, and brain and tumor tissues were harvested. The head of each mouse was removed, and the cranium split apart to expose the brain and tumor for collection. Tumor borders were established based on the appearance of surrounding tissue and evident tumor masses on the brain, if applicable. All samples were collected, and wet weight was measured before lyophilization. Samples were weighed again after lyophilization to obtain dry weights. Lyophilized organs were digested with aqua regia over 72 hours, diluted with 1 N HNO_3, and filtered with a syringe filter to remove any solid contaminants. Digested and purified samples were then examined with inductively coupled mass spectrometry (ICP-MS) to determine the presence of Au content within the tissue samples. Au content in each organ was then normalized to dry weights to assess the biodistribution of GNPs within collected tissues.

Statistical analyses were completed for the weights of tumor and brain tissues by using student t-tests ($\alpha=0.05$). In addition, investigations were conducted for biodistribution studies using two-way ANOVAs with Bonferroni post-hoc tests ($\alpha=0.05$).

Fold increase of accumulation of GNPs in tumor tissues compared to brain tissue was also investigated from reported biodistribution data. Statistical analyses on the fold increase of GNPs in tumor tissues were completed using a student t-test (α=0.05).

2.2.16 Statistical Analyses

All data were collected and processed in Microsoft Excel. Appropriate statistical tests were completed using GraphPad Prism version 7.0.0 for Windows, GraphPad Software (San Diego, California; www.graphpad.com) using a significance level of $\alpha = 0.05$. Unless otherwise noted, data are presented as mean values +/- standard deviation. Statistical tests and sample sizes reported are described in each methods section.

CHAPTER 3

GNP SYNTHESIS AND IN VITRO CHARACTERIZATION OF PEG-AS1411-GNP

3.1. Introduction

AS1411 and GNP combinations have led to new and novel therapies for many cancers [52, 94, 161, 163, 168, 182-187]. Because of this and the rising need for generating new successful and non-invasive GBM therapies, we have aimed to develop an optimal PEG/AS1411 GNP system tailored to act against GBM. We set out to first optimize the loading of PEG and AS1411 onto the GNP surface by varying the ratios of conjugated PEG and AS1411 components (Aim 1). Then, for each ratio of AS1411 and PEG in the study, bioactivity within GBM U-87 MG cells and GNP physicochemical characteristics were compared to determine the best candidate particle to continue in the project. Optimizing at this stage allows for a baseline anti-GBM bioactivity to be established. Bioactivity of the treatments in GBM cells was determined by measuring changes in metabolic activity, growth and alterations to cell morphology.

PEG is an anti-fouling molecule employed to protect particles from protein adsorption. The hydroxy-terminated PEG used in this study also serves as a surface a reactive site for further modification of GNPs with A21 (Aim 2). The PEG linker consists of 4 ethylene glycol repeats bearing an SH group on one end and an alcohol group on the other. Typical PEG conjugates onto nanoparticles are in the 1-5 kDa range, whereas ours is 0.2 kDa. This smaller PEG was chosen because it allows for future modifications with A21 while not interrupting specific AS1411 bioactivity.

3.2 Determining Optimal PEG/AS1411 Conjugation Ratios onto GNPs

To determine the optimal PEG/AS1411 GNP configuration for GBM applications, human GBM-representing cells (U-87 MG) were exposed to GNPs with differing PEG and AS1411 loading ratios. A schematic of PEG/AS1411 detailing the proposed topographic features is shown in **Figure 2-1** from Chapter 2. Maximum possible loading of all components onto PEG/AS1411 GNPs was held constant at 12 times (expressed as 12X) the concentration of Au present within a colloidal solution. The colloidal solution concentrations were measured by UV-VIS spectrometry at 260 or 520 nm characteristic wavelengths for AS1411 and Au, respectively.

This 12X loading was divided up into multiple molar ratios of PEG/AS1411, resulting in the following experimental conditions, which were preserved throughout this dissertation: no PEG loading with maximum AS1411 loading (12X), maximum PEG loading with no AS1411 loading (0X), and three different loading ratios of PEG/AS1411 (3X, 6X, and 9X). For formulations below the maximum of 12X AS1411, PEG was introduced to fulfill the maximum loading requirements. Thus, the PEG/AS1411 GNP formulations were synthesized and differed by their loading molar ratios of PEG and AS1411. A schematic of the GNPs tested is shown in **Figure 2-2** from Chapter 2. All nomenclature is based on the amount of AS1411 conjugated to the GNP surface.

3.2.1: Characterizing the Synthesis of PEG/AS1411 GNPs

A PEG/AS1411 GNP system was synthesized sterilely by adding appropriate amounts of PEG with annealed and purified AS1411 to sterilely synthesized, unconjugated 4 nm GNPs (bare GNPs) in solution. PEG/AS1411 conjugated GNPs are then stabilized by stepwise addition of 10X PBS over five days, diluting the GNP solution to a 1X PBS concentration. The successful synthesis of PEG/AS1411 GNPs was confirmed using zeta potential (mV), hydrodynamic diameter (nm), PDI (unitless), oligonucleotide number per GNP, and UV/visible spectroscopy as shown in **Figure 3-1**.

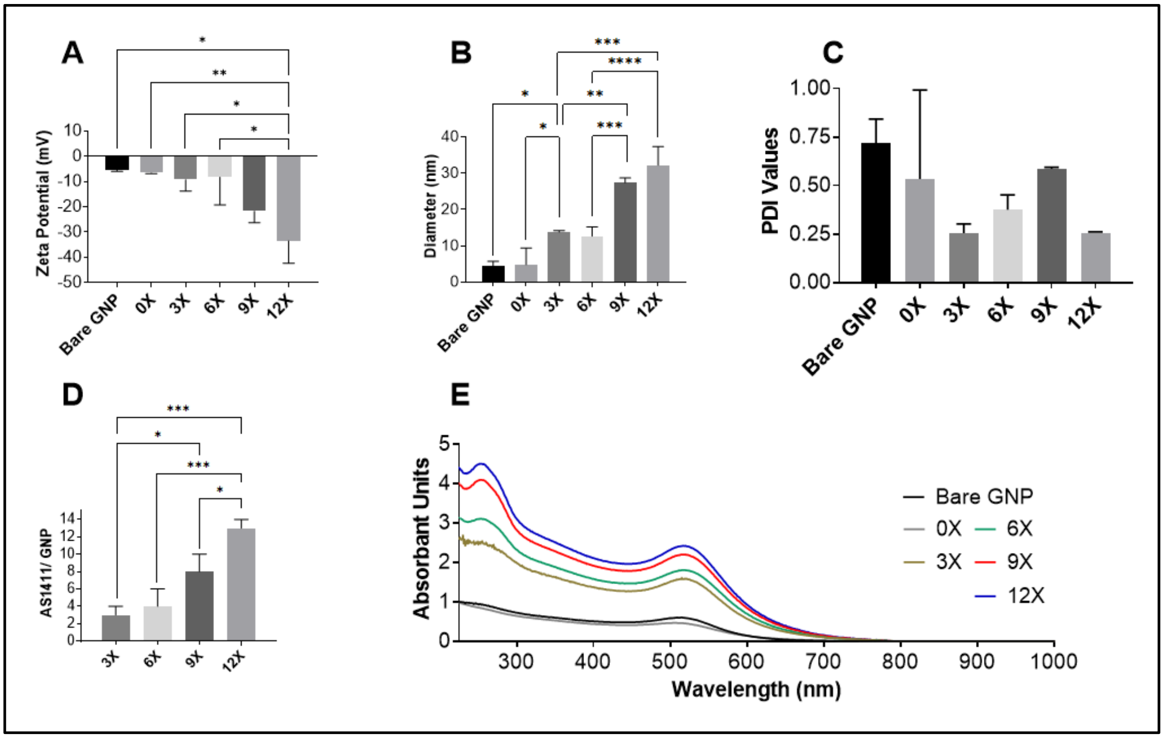

Figure 3-1: Characteristics of various syntheses of PEG/AS1411 GNPs. (A-C) Zeta potential (mV), diameter (nm), and PDI (unitless) measurements for all PEG/AS1411 GNPs and unconjugated GNP (bare) controls. (D) AS1411 loading within GNP syntheses with AS1411. (E) Resulting UV-VIS spectra for each PEG/AS1411 GNP and bare GNP control. Values are reported as mean ± standard deviation (n=3 independent syntheses). *, **, ***, and **** represent $p < 0.05, 0.01, 0.001$, and 0.0001, respectively and are reported from one-way ANOVAs with Bonferroni post-hoc test ($\alpha = 0.05$).

Zeta potential measurements help identify surface charges of nanoparticles and were used as a guideline for implying particle stability [188]. Generally, an increase in zeta potential absolute value suggests a more stable particle due to increased electrostatic repulsion between particles. Zeta potential measurements of stable GNPs measure > 20 mV in magnitude [165, 189, 190]. A gradual increase in zeta potential measurements was seen for all syntheses as AS1411 loading was increased due to the highly charged phosphate backbone of the AS1411 oligonucleotide (**Figure 3-1A**). The 12X PEG/AS1411 GNP synthesis showed the most significant increase in zeta potential magnitude (-33.5 ± 8.85) when compared to 0X PEG/AS1411 GNPs (-6.61 ± 0.262; $p<0.0074$). This is expected due to the negative charge of AS1411 and the increased amount of introduced AS1411 for each PEG/AS1411 GNP synthesis. The 9X and 12X PEG/AS1411 GNP syntheses were the most stable, with zeta potential measurements of -21.7 ± 4.57 mV and -33.5 ± 8.85 mV, respectively.

Hydrodynamic size measures the size of the Au core, conjugated biomolecules, and the hydration shell around a particle when in solution. The hydrodynamic diameter will increase as biomolecules are conjugated to a surface. The reported size is used as a gauge to verify the conjugation of molecules and further imply particle stability. For all PEG/AS1411 GNP formulations, a stepwise increase in hydrodynamic size was seen (**Figure 3-1B**). 0X particles had the smallest increase in hydrodynamic diameter compared to bare GNPs. This is expected due to the small length of PEG molecules (approximately 1.12 nm). 0X and 3X syntheses are significantly different in size (4.81 ± 4.60 nm vs. 13.7 ± 0.40; $p<0.0372$), establishing that hydrodynamic diameters are significantly increased due to an increase in AS1411 loading. However, the rise in AS1411 loading did not significantly alter the sizes between 3X and 6X PEG/AS1411 GNP nor 9X and 12X PEG/AS1411 GNP. Both 9X and 12X PEG/AS1411 GNPs increased in hydrodynamic diameter significantly when compared to 3X and 6X GNPs ($p<0.0018$ and $p<0.0009$ for 9X vs. 3X and 9X vs. 6X, respectively—$p<0.0001$ for both 12X vs. 3X and 12X vs. 6X). This data indicates an effect on the size based on the number of conjugated AS1411 to the nanoparticle surface. It also implies that the difference in hydrodynamic diameters between 3X and 6X PEG/AS1411 GNPs versus 9X and 12X PEG/AS1411 GNPs is insignificant compared to the differences between 6X and 9X PEG/AS1411 GNP syntheses.

PDI values, defined as the standard deviation of particle size divided by the average measured size, are used as a gauge for particle uniformity in terms of whether the particle population is monodispersed (uniform diameters with PDI values close to 0) or polydispersed (non-uniform diameters with PDI values more relative to 1). Benchmark values of PDI—suggesting a monodispersed size distribution, and thus increased stability—of particles are in the range of 0.5 to 0.7 [165, 189, 190]. Once AS1411 is conjugated to the surface of the GNP, PDI values are lowered (**Figure 3-1C**), indicating increased particle uniformity due to AS1411 loading. All PEG/AS1411 GNP formulations were similar, indicating PDI values within benchmark ranges.

Alongside increased values for zeta potential and hydrodynamic sizes, the measured values of AS1411 loading per GNP increased as the AS1411/PEG ratio increased from 0X to 12X (**Figure 3-1D**). The zeta potential measurements, quantification of AS1411/GNP, and DLS measurements support a successful synthesis of each PEG/AS1411 GNP formulation.

Absorbance maxima at 520 nm wavelengths (**Figure 3-1E**) showed a slight red shift (to higher wavelengths) upon conjugation of AS1411 and PEG to GNPs. This shift is common when altering the surface of GNPs, as the SPR frequency is susceptible to the local refractive index near the particle surface [191]. Furthermore, the absorbance maxima at 260 nm increased as AS1411 loading was increased. This qualitative assessment further suggests a successful synthesis of PEG/AS1411 GNPs.

Based on the data above, 9X or 12X GNP formulations have the best attributes in terms of particle stability. This is based on PDI, AS1411 per GNP, UV-VIS data, and zeta potential. However, the ultimate determination of which GNP formulation is best as a GBM therapeutic requires an assessment of the bioactivity in a U-87 MG *in vitro* model of GBM.

3.2.2 Antiproliferative Ability of PEG/AS1411 GNPs

To determine the best candidate PEG/AS1411 GNP formulation for use as a GBM therapeutic, the effects of PEG/AS1411 GNPs *in vitro* on U-87 MG cell proliferation was assessed (**Figure 3-2**). The reduced proliferation of U-87 MG cells from PEG/AS1411 GNPs was determined using XTT assays, which correlate the absorbance of a dye to perceived cellular metabolic activity. U-87 MG cells were exposed to various treatment concentrations of AS1411 within each PEG/AS1411 GNP formulation. Concentrations of AS1411 in each PEG/AS1411 GNP solution were verified with UV-VIS and AS1411/GNP loading data before XTT assays were completed. U-87 MG cells treated with 0X PEG/AS1411 GNPs were exposed to the maximal concentration of GNP found among the treatments.

0X PEG/AS1411 GNPs showed minimal effect on metabolic activity due to the lack of conjugated AS1411 to the GNP surface, **Figure 3-2**. This result indicated that GNPs conjugated only with PEG molecules in this study have no significant inherent effects on GBM cell proliferation. 3X, 6X, and 12X PEG/AS1411 GNP formulations expressed similar behaviors with acute effects on proliferation at lower treatment concentrations of AS1411. 12X PEG/AS1411 GNPs had the least overall impact on metabolic activity, implying that among all PEG/AS1411 GNPs, this formulation had the least effect on metabolic activity in U-87 MG cells. 9X PEG/AS1411 GNPs caused a concentration-dependent decrease in metabolic activity and the most significant overall reduction in metabolic activity among the different formulations.

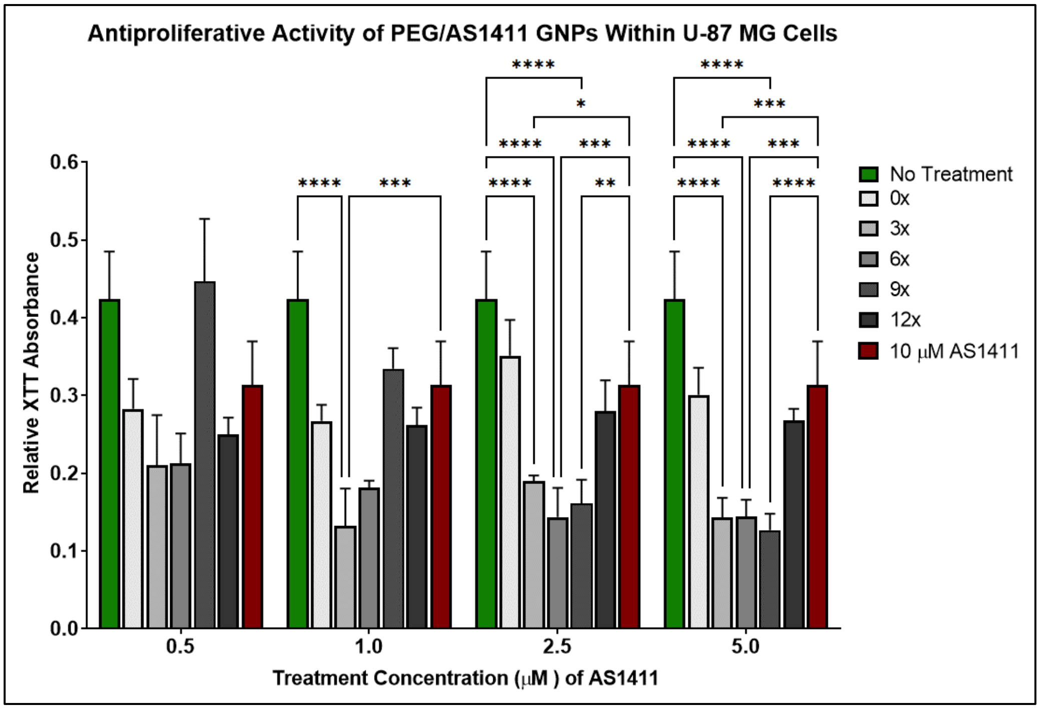

Figure 3-2: Antiproliferative activity of PEG/AS1411 GNPs within U-87 MG cells at various AS1411 treatment concentrations. No treatment represents non-treated control groups (media only). 10 μM AS1411 represents standalone AS1411 (unbound to GNP). *, **, ***, **** represent p<0.05, p<0.01, p<0.001, and p<0.0001, respectively, and are reported from two-way ANOVAs with Bonferonni post-hoc tests (α=0.05). Values are reported as average XTT absorbance ± standard deviation (n =3 independent replicates for GNP treatments; n=6 independent replicates for controls).

Additionally, from **Figure 3-2**, 9X PEG/AS1411 GNP syntheses significantly decreased metabolic activity in U-87 MG cells at 2.5 and 5 μM AS1411 treatment concentrations compared to no treatment control groups (62.05% and 70.07% decreases, respectively; *p*<0.0001 for both comparisons). 9X PEG/AS1411 GNPs also enhanced the reduction of metabolic activity by close to 2 fold at 2.5 and 5 μM AS1411 treatment concentrations (48.69% and 59.53% decreases in metabolic activity, respectively) when compared to the 26.03% decrease seen with 10 μM of standalone (unconjugated to GNP) AS1411 treatment. Although 3X PEG/AS1411 GNP syntheses showed a significant early decline in metabolic activity, the lack of concentration-dependent cytotoxicity and poor physicochemical properties ruled them out as a candidate for an optimal PEG/AS1411 GNP formulation.

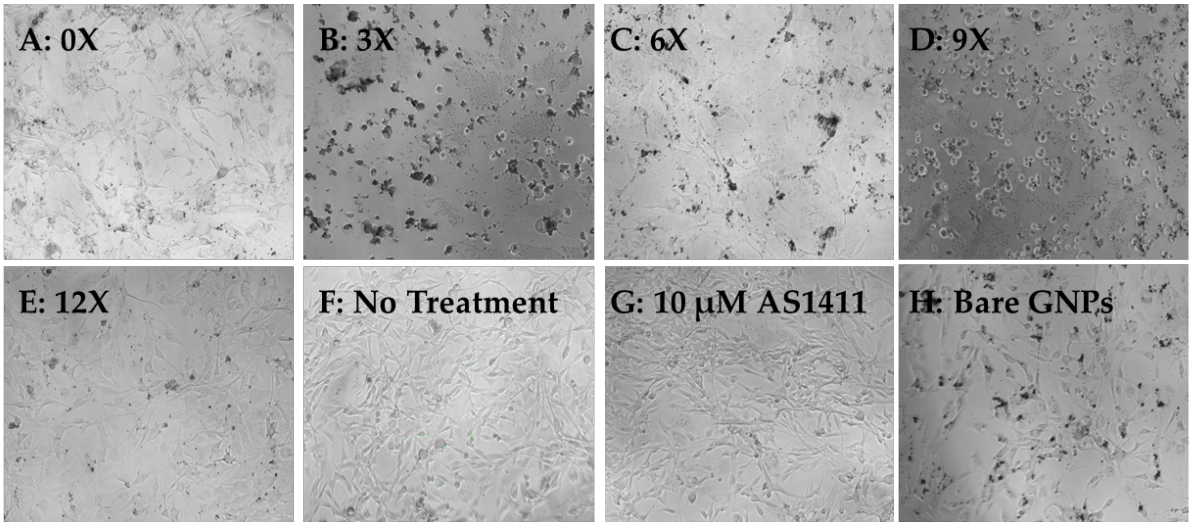

<u>Figure 3-3</u>: Morphological effects on U-87 MGs from treatment with PEG/AS1411 GNPs. Panels (a) through (e) represent 1 μM equivalent AS1411 treatment groups. Panels (f) through (h) represent control groups. The scale bar indicates 100 microns.

The effects of our GNP treatments on U-87 MG cellular morphology (**<u>Figure 3-3</u>**) were also examined. U-87 MG morphology in the 9X panel (**<u>Figure 3-3D</u>**) compared to the non-treated panel (**<u>Figure 3-3F</u>**) shows an alteration to the classical neuronal morphology. U-87 MG cells became more circular for this treatment. **<u>Figure 3-3H</u>** shows an apparent effect of citrate-coated GNP starting material on cell counts, suggesting that these GNPs affect normal cellular behavior but possibly not at cytotoxic levels. This impact of citrate-coated GNP interactions with cells has been previously reported [192-194]. The 9X panel (**Figure 3-3D**) lacks the intense black spots due to nanoparticle aggregation found in the 3X, 6X, and bare GNP treatments, indicating greater nanoparticle stability under the treatment conditions for the 9X PEG/AS1411 GNPs. **Figure 3-3D** shows U-87 MG morphologies closely related to reported morphologies of cells undergoing methuosis, a non-apoptotic cellular death pathway broadly implicated in AS1411-based treatments [93, 195, 196]. In evaluating the XTT and morphology data, 9X PEG/AS1411 GNPs displayed the most effects on cell metabolic activity and morphology at all concentrations of AS1411. Therefore, it was chosen as the PEG/AS1411 GNP formulation for the rest of the *in vitro* studies.

3.3 Specificity of PEG/AS1411 GNPs

To verify that the effects seen from 9X PEG/AS1411 GNPs are due precisely to the AS1411 sequence, 9X GNP synthesis ratios were reproduced with a control oligonucleotide, CRO, where each guanine base in AS1411 is replaced with cytosine. XTT metabolic assays were then used to compare the bioactivity of 9X PEG/AS1411 GNPs to that of 9X PEG/CRO GNPs (**Figure 3-4**).

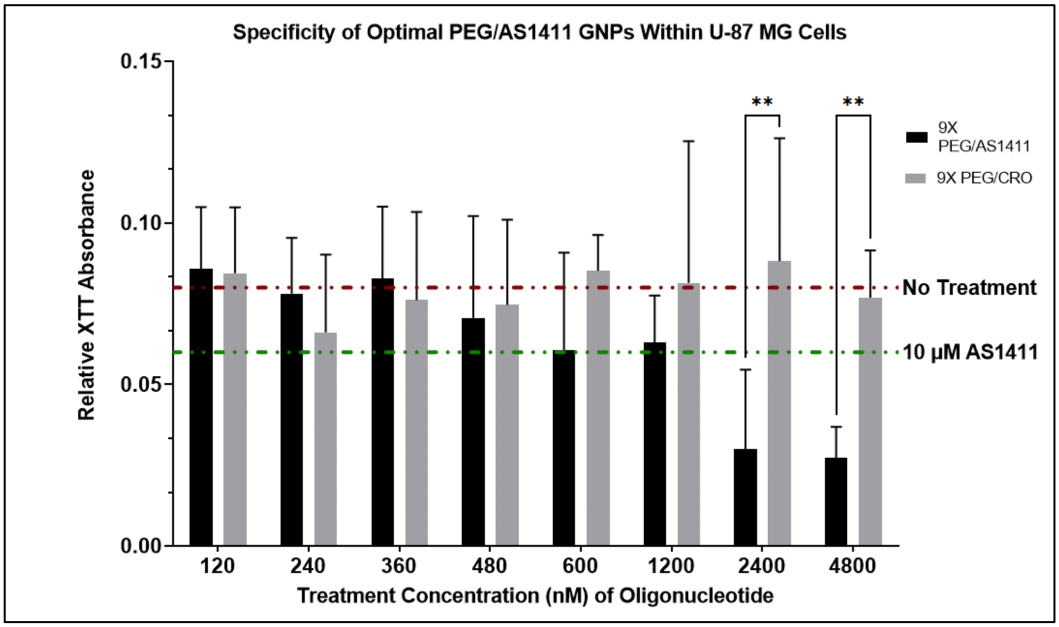

Figure 3-4: Antiproliferative activity of optimal PEG/AS1411 GNPs (black bars) versus PEG/CRO GNPs (gray bars) within treated U-87 MG cells at various treatment concentrations of oligonucleotide after 72 hours of treatment. Values are reported as average absorbance values ± standard deviation (n=5 independent replicates). A significance level of ** represents p<0.01 and is reported from two-way ANOVAs with Bonferroni post-hoc test (α=0.05).

9X PEG/AS1411 GNPs again demonstrated antiproliferative ability and continued to have dose-dependent decreases in the metabolic activity of U-87 MG cells. Treatment with 9X PEG/AS1411 GNPs led to a 75.0% decrease in metabolic activity at 4.8 µM AS1411 compared to the non-treated control. However, the 9X PEG/CRO GNPs only caused only a 5% decrease in metabolic activity in U-87 MGs compared to the non-treated control at ~5 µM CRO concentration. This value remains consistent for most concentrations tested with PEG/CRO GNPs. 9X PEG/AS1411 GNPs began to show significant decreases on U-87 MG metabolic activity when compared to 9X PEG/CRO GNPs at ~2.5 and 5 µM oligo (p<0.0012 and p<0.0017, respectively). This indicated the specificity of AS1411 within PEG/AS1411 GNPs towards their antiproliferative activity.

3.4 U-87 MG Growth Effects of PEG/AS1411 GNPs

Proliferation is a hallmark of GBM, contributing to its highly invasive and infiltrative nature and clinical progression. To further quantify the effects of PEG/AS1411 on GBM, cell counts were performed after 72 hours of treatment. The number of U-87 MGs decreased with PEG/AS1411 GNP treatment at all treatment concentrations of AS1411, **Figure 3-5**. The number of cells were significantly reduced by 37.38%, 75.57%, and 56.49% for 1, 2, and 5 µM AS1411, respectively (p<0.001 for all). Additionally, 9X PEG/AS1411 GNPs significantly reduced the cell number at 2 µM AS1411 treatment concentration compared to 1 µM AS1411. However, the reduction of cell counts was not enhanced at 5 µM AS1411 treatment concentrations, suggesting that there is an optimal AS1411 treatment concentration of PEG/AS1411 GNPs. PEG/CRO GNPs treated at the same oligonucleotide concentrations did not significantly decrease in U-87 MG cell number.

Other studies have investigated the effects on GBM regulation of proliferation using NCL interaction with AS1411. They have shown significant decreases (near 40%) in U-87 MG cells after 48 hours of 5 µM AS1411 treatment and a 50% decrease after 72 hours [197]. The GNP produced here has improved the AS1411 antiproliferative effects by showing a 75% decrease in cell number after 72 hours of treatment at lower concentrations of AS1411 (2 µM). This data confirms the increased bioactivity of AS1411 against U-87 MG cells when conjugated to GNPs. This result is supported in previous studies, with the antiproliferative effects consistent across two cancer cell types. [52]

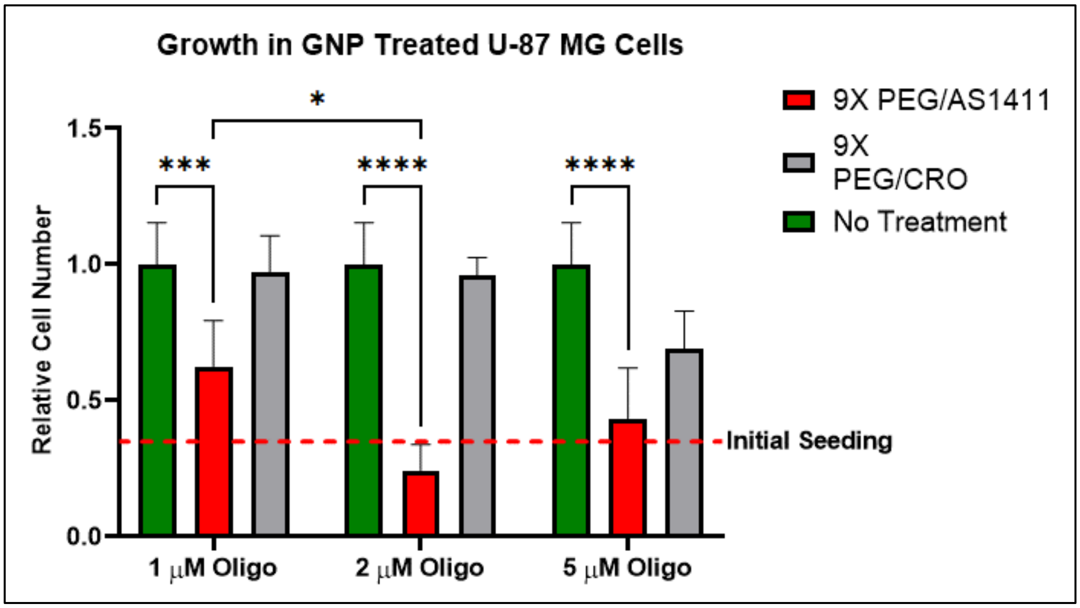

<u>Figure 3-5</u>: Growth effects on U-87 MG cells of optimal 9X PEG/AS1411 or PEG/CRO GNPs at differing oligo concentrations. No treatment (only media) serves as the control. Cell count measurements were normalized to initial seeding density (dashed red line) and are presented as normalized average fold increase of cells ± standard deviation (n=3). Statistical significance of *, ***, and **** represents $p<0.05$, <0.001, and <0.0001. Significance is reported from two-way ANOVAs with Bonferonni post-hoc test ($\alpha=0.05$).

Mechanistic studies in other cancer cell types have aimed at elucidating the antiproliferative role of AS1411. Studies have shown that treatment with AS1411 modestly increases EGFR phosphorylation leading to an increase in phosphorylation of Akt and Rac1 proteins, which most likely contributes to its antiproliferative nature [93]. In addition, analyzing gene expression of significant cancer-related genes in malignant cells has implicated additional cell cycle mediators (TP53, CDK proteins, MDM proteins, and BCL2/BAX) in the mechanism of AS1411-related cytotoxicity. However, specific relationships still need clarification [154, 198].

3.5 Conclusions

A PEG/AS1411 GNP system has been developed, optimized, and designed to be active against GBM cells *in vitro*. 9X PEG/AS1411 GNPs were stable, as evidenced by zeta potential data, hydrodynamic size, and PDI values. Screening various PEG/AS1411 GNP loading ratios further implicated the 9X formulation as the optimal GNP type as a potential GBM therapeutic. Metabolic assays showed the most notable effects on the metabolic activity of U-87 MGs treated with 9X PEG/AS1411 GNPs. Furthermore, the most significant impact on U-87 MG cellular morphology resulted from treatment with 9X PEG/AS1411 GNPs. AS1411 conjugated to PEG/AS1411 GNPs retained specificity compared to the CRO analog oligonucleotide and decreased U-87 MG cell numbers after treatment. The PEG/AS1411 GNP design allows conjugating of other anti-GBM molecules, including gene therapy molecules like A21. The synthesis and performance of these further modified 9X PEG/AS1411 GNPs are presented in the following chapters.

CHAPTER 4

SYNTHESIS AND IN VITRO CHARACTERIZATION OF PEG/AS1411/A21 GNPs

4.1. Introduction

Chapter 3 of this dissertation described the optimization of the PEG: AS1411 ratio on GNPs in terms of particle stability and anti-GBM bioactivity. The system was designed to make further modification possible with additional anti-GBM oligonucleotides through conjugation to the PEG molecules. In GBM, miR-21 is the most frequently dysregulated miRNA and plays a vital role in oncogenesis by affecting numerous tumor suppressors and oncogenes [102, 125, 199, 200]. Down-regulation of miR-21 through A21 leads to GBM cell inhibition [121]. Because of this established miR-21 activity in GBM, it was postulated that adding A21 via the PEG linker would increase the efficacy of PEG/AS1411 GNPs.

PEG/AS1411/A21 GNPs were synthesized, and their anti-GBM properties were compared to PEG/AS1411 GNPs. Comparisons were based on the demonstrated anti-GBM activity on U-87 MG cell metabolic ability, morphology, and growth from Aim 1. In addition, downstream effects of PEG/AS1411/A21 GNPs treatments on the levels of free miR-21 transcripts and expression of miR-21-related proteins STAT3 and PTEN in U-87 MG cells were also used to assess the delivery of functional A21.

To assess the effect of A21 loading density on the nanoparticle surface, three different formulations of PEG/AS1411/A21 GNPs were synthesized that varied by their molar ratios of PEG: A21 loading. Like Aim 1, the determination of an optimized A21 loading onto PEG/AS1411 GNPs was based on the effects of nanoparticle treatments on the metabolic activity, morphology, and growth effects on U-87 MG cells in addition to GNP characteristics. In addition, due to the potential impact of introducing anti-miR technology to the nanoparticle, bioactivity assessments were expanded to include effects on U-87 MG cell mobility and modulation of target miR-21 transcripts and associated expression of downstream proteins.

4.2 Characterization of PEG/AS1411/A21 GNPs

4.2.1: Synthesis of PEG/AS1411/A21 GNPs

PEG/AS1411/A21 GNPs were synthesized by conjugating carboxy-modified A21 to GNP-bound PEG hydroxyl groups on 9X PEG/AS1411 GNP. EDC and Sulfo-NHS chemistry was employed for the conjugation. **Figure 2-3** from Chapter 2 shows the proposed topography of the PEG/AS1411/A21 GNP system. A21 was introduced to PEG/AS1411 GNP solutions in different molarity ratios of PEG to A21, resulting in three particle solutions (**Figure 2-4** from Chapter 2) 1:1 A21:PEG (1.0 A21 GNPs), 1:2 A21:PEG (0.5 A21 GNPs), and 1:4 A21:PEG (0.25 A21 GNPs). Optimal 9X PEG/AS1411 GNPs from Aim 1 are notated by the same nomenclature from Chapter 3.

The successful synthesis of PEG/AS1411/A21 GNPs was confirmed by measuring the zeta potential, hydrodynamic diameter, PDIs, and UV-VIS spectra of each formulation, **Figure 4-1**. Significant decreases in zeta potential measurements were seen upon the addition of A21 for all formulations of PEG/AS1411/A21 GNPs (**Figure 4-1A**) when compared to 9X PEG/AS1411 GNPs. This phenomenon implied that A21 conjugation might lead to greater shielding of the GNP surface charge due to ions in the buffer solution more tightly associating with the GNPs, or possibly compaction of the oligonucleotide coating due to interactions between A21 and AS1411. While a decrease in zeta potential measurement usually suggests a less stable GNP synthesis, it is essential to note that no aggregation or changes in GNP dispersion color over the 72-hour experiments (discussed in the following sections) were observed. Thus, it is implied that the GNPs remained stable to aggregation despite the reduced zeta potentials.

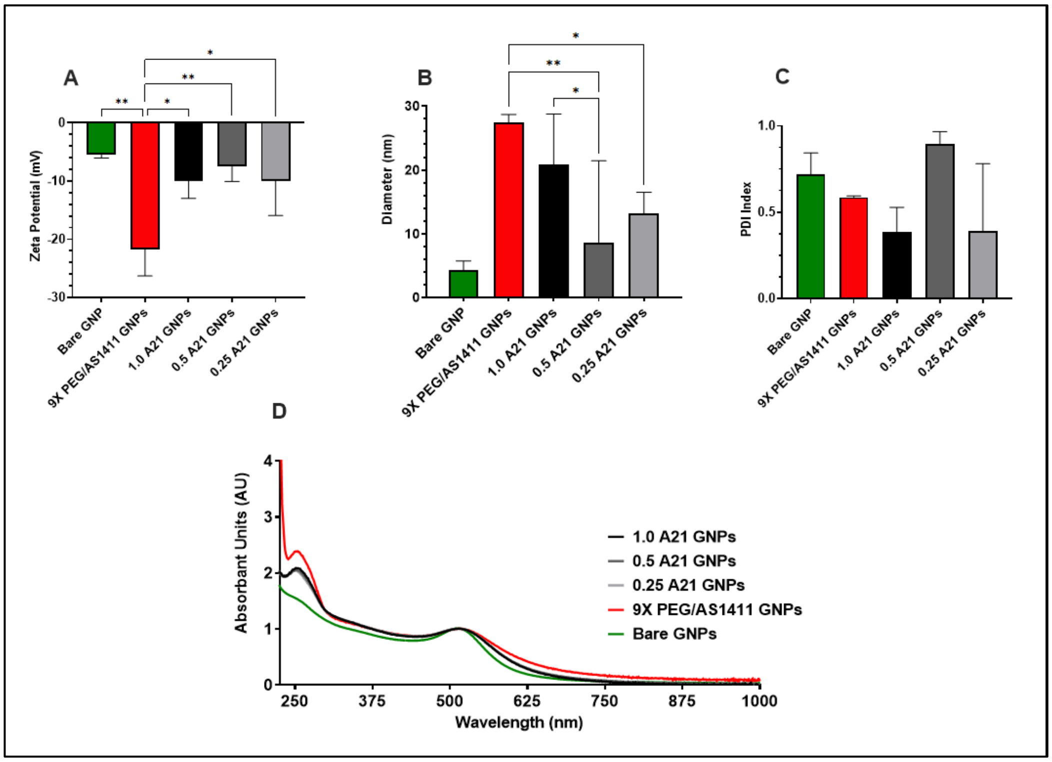

<u>Figure 4-1</u>: Zeta potential (A), Hydrodynamic Diameter (B), and PDI (C), and UV-VIS spectra (D) for PEG/AS1411/A21 GNPs, as measured by DLS or UV-VIS spectroscopy. GNP formulations with AS1411 and A21 (black and gray bars) are indicated by ratios of PEG to A21 (1.0 A21 GNPs, 0.5 A21 GNPs, or 0.25 A21 GNPs) and compared to 9X PEG/AS1411 GNPs (red bars) or bare 4 nm GNPs (green bars). * and ** indicate $p < 0.05$ and $p < 0.01$, respectively, from one-way ANOVA with Bonferonni post-hoc tests (n=3 independent syntheses; data presented as mean ± standard deviation; ($\alpha=0.05$).

Significant decreases in hydrodynamic diameter were also seen for all formulations of PEG/AS1411/A21 GNPs (**<u>Figure 4-1B</u>**) when compared to unmodified PEG/AS1411. This result further supports the idea of compaction of the oligonucleotide coating upon A21 conjugation. This result is reinforced in PDI measurements (**<u>Figure 4-3C</u>**), where PDI values decreased for 2 of the GNP formulations (1.0 A21 and 0.25 A21 PEG/AS1411/A21 GNPs). This suggested greater uniformity in PEG/AS1411/A21 GNPs of these two GNP formulations, possibly due to the compaction. UV-VIS spectra of

PEG/AS1411/A21 GNPs (**Figure 4-3D**) were similar for all PEG/AS1411/A21 GNP formulations. Absorbance maxima in the characteristic region for DNA/RNA (~260 nm) further suggests the tight association between ions and GNPs, as indicated by PEG/AS1411/A21 maxima falling between bare GNP and 9X PEG/AS1411 GNPs. This phenomenon in the UV-VIS spectra could represent a hyperchromic effect [201] due to base pairing between RNA bases of A21 with DNA bases of AS1411.

4.2.2 Antiproliferative Ability of PEG/AS1411/A21 GNPs

XTT cell metabolic activity assays were performed to assess the *in vitro* performance of PEG/AS1411/A21 GNPs (**Figure 4-2**). These assays were used to determine if there was an optimal configuration of PEG/AS1411/A21 GNPs for GBM applications. U-87 MG cells were exposed to the 3 different PEG/AS1411/A21 GNP formulations at 5 different AS1411-equivalent treatment concentrations each (0.25, 0.5, 1.0, 2.0 and 5.0 μM). All treatment concentrations were based on the concentration of AS1411 conjugated to the GNPs as determined by UV-VIS spectroscopy before A21 modification. Therefore, any differences in metabolic activity of the cells would be attributed to the presence of A21.

All PEG/AS1411/A21 GNP formulations displayed antiproliferative activity in U-87 MG cells. The 1.0 PEG/AS1411/A21 GNPs affected U-87 MG cellular metabolism with the most decreases in metabolic activity in a dose-dependent manner. This effect is like the 9X PEG/AS1411 GNPs, showing a dose-dependent reduction in U-87 MG cellular metabolic activity. Among all PEG/AS1411/A21 GNP formulations at 5.0 μM equivalent AS1411 treatment concentrations, 1.0 PEG/AS1411/A21 GNPs showed the most significant decrease in metabolic activity with an 84.8% decrease compared to NT controls (*p*<0.0083). In addition, this GNP formulation performed the closest to 9X PEG/AS1411 GNPs at the same concentration (a significant 90.9% decrease compared to NT; *p*<0.0023); thus, there appeared to be no loss of PEG/AS1411 GNP anti-GBM activity upon the conjugation of A21 at a 1:1 A21:PEG. However, no apparent benefit of A21 addition to PEG/AS1411 GNPs was observed in this assay.

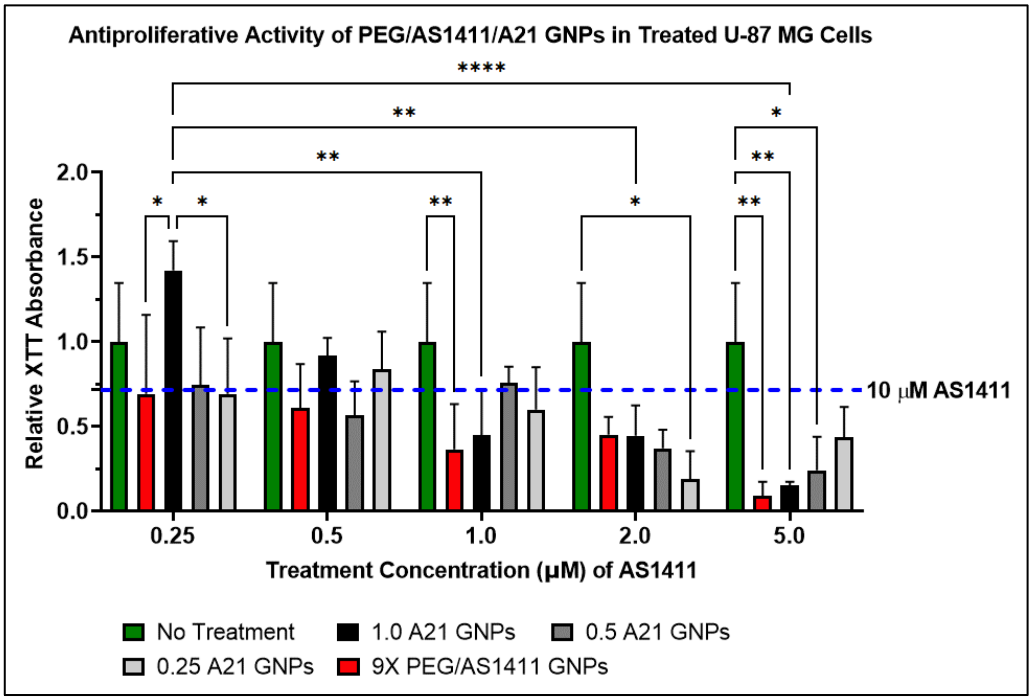

Figure 4-2: Antiproliferative activity of PEG/AS1411/A21 GNP treated in U-87 MG cells at various treatment concentrations of AS1411. No treatment represents non-treated control groups (media only). 10 μM AS1411 represents standalone AS1411 (unbound to GNP). Values are reported as average XTT absorbance ± standard deviation (n =3 independent replicates for GNP treatments; n=6 independent replicates for controls). *, **, **** represent p<0.05, p<0.01, and p<0.0001, respectively, and are reported from two-way ANOVAs with Bonferonni post-hoc tests (α=0.05).

To further explore the ramifications of adding A21 to the PEG/AS1411 GNP formulation, the effects of PEG/AS1411/A21 GNP treatments on U-87 MG cellular morphology were examined (**Figure 4-3**).

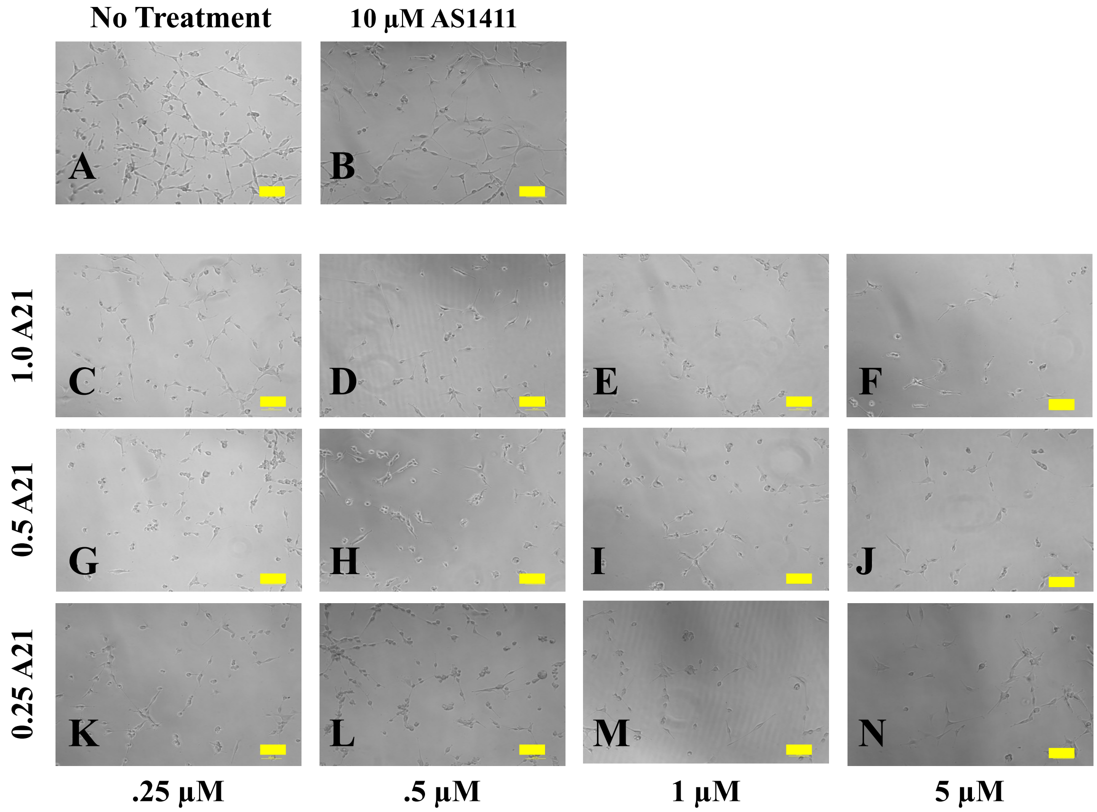

Figure 4-3: Morphological changes in U-87 MG cells after 72-hour treatment with PEG/AS1411/A21 GNPs. Images were acquired at 10X magnification and taken on a Nikon TE2000 Epifluorescent microscope. Treatments (C-N) are listed as the concentration of AS1411 vs. GNP formulations with varying A21:PEG ratios. The top panels (A-B) represent control images for comparison. The scale bar indicates 100 microns.

U-87 MG cell morphologies after 72-hour exposure to 1.0 PEG/AS1411/A21 GNPs formulation (**Figure 4-3 C-F**) showed an alteration to the classical neuronal morphology of branched networks of cells compared to no-treatment controls **Figure 4-3A**). Furthermore, as the treatment concentration increased, U-87 MG cells incubated with the 1.0 PEG/AS1411/A21 GNPs (**Figure 4-3 C-F**) became more circular and sparse compared to other treatment panels (**Figure 4-3 G-N**)—implying a more significant effect on cellular function than 0.5 and 0.25 PEG/AS1411/A21 GNPs. Taken together with XTT cell viability, the 1.0 PEG/AS1411/A21 GNPs formulation is implicated as the best performing PEG/AS1411/A21 GNP formulation in that it (1) decreases U-87 MG cell metabolic activity; (2) induces changes in U-87 MG cell morphology *in vitro, and* (3) appears to maintain previously reported hallmarks of AS1411 bioactivity. However, the A21 addition to the nanoparticles still had no apparent benefit. Thus, additional insights into U-87 MG cellular growth, motility, and expression of miR-21 genetic targets aimed to determine whether A21 addition to PEG/AS1411 was beneficial.

4.3 Anti-GBM Activity of PEG/AS1411/A21 GNPs

4.3.1 Effects on GBM Growth

Rapid growth is a hallmark of GBM due to its highly invasive and infiltrative nature and clinical progression [202]. Therefore, as in Aim 1, cell counts were evaluated after 72 hours of PEG/AS1411/A21 GNP treatment (**Figure 4-4**). U-87 MG cells were treated with 9X PEG/AS1411 GNPs, the 3 formulations of PEG/AS1411/A21 GNPs, and controls. Controls included NT and 10 μM standalone (unconjugated) AS1411, and 10 nM Lipofectamine transfected A21. Treatment concentrations were based on the effective AS1411 concentration in each GNP sample (1, 2, or 5 μM equivalent AS1411).

U-87 MG cells treated with either 10 μM standalone AS1411 or 10 nM of Lipofectamine transfected A21 showed significant decreases in the total number of cells compared to NT controls (65.5% and 70.0% decreases, respectively; $p<0.0001$ for both). All GNP treatments significantly reduced cell number compared to NT controls (a maximum of $p<0.0089$) at all AS1411 treatment concentrations. Additionally, PEG/AS1411/A21 GNPs performed similarly to PEG/AS1411 GNPs at all AS1411 treatment concentrations.

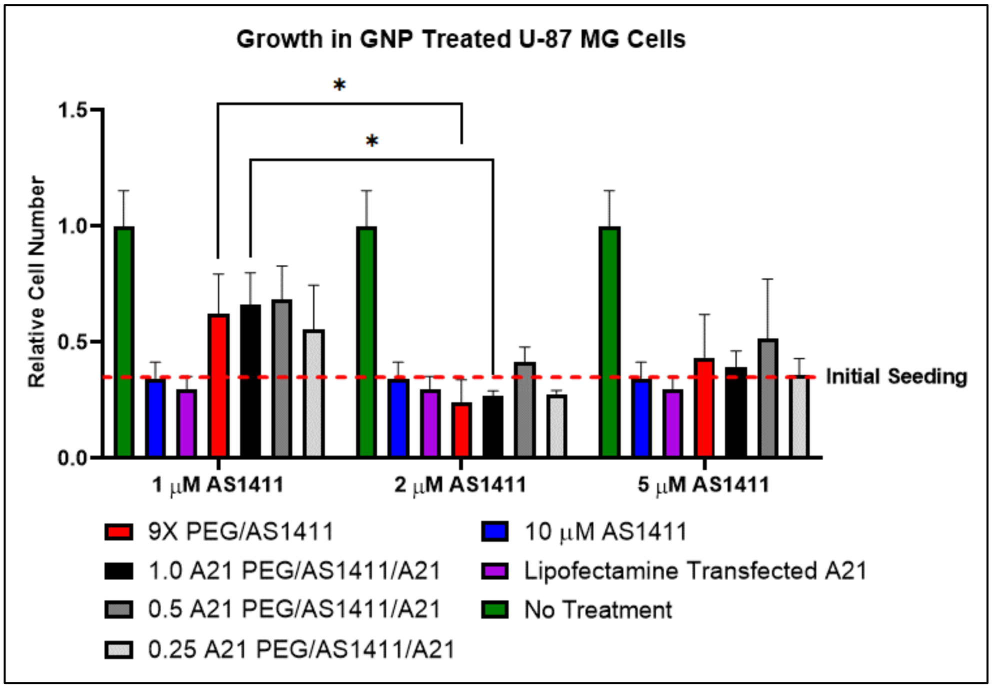

Figure 4-4: Growth effects on U-87 MG cells treated with 9X PEG/AS1411 or formulations of PEG/AS1411/A21 GNPs at differing AS1411 concentrations. No treatment (only media), 10 µM AS1411, and 10 nM Lipofectamine transfected A21 are controls. Cell count measurements were normalized to initial seeding density (dashed red line) and are presented as normalized average fold increase of cells ± standard deviation. Statistical significance of * represents $p<0.05$ ($n = 3$ biological replicates for all treatments across all experiments; 6 total experiments were completed with independent NT controls). Significance is reported from two-way ANOVAs with Bonferroni post-hoc test ($\alpha=0.05$).

Cell number results implied an optimal treatment concentration of 2 µM AS1411 in all GNP types to obtain maximum inhibition of U-87 MG growth. Among the PEG/AS1411/A21 GNPs across all concentrations, only 1.0 PEG/AS1411/A21 GNPs showed a significant decrease at 2 µM vs. 1 µM AS1411 treatment ($p<0.0350$). The 1.0 PEG/AS1411/A21 GNPs are also the only PEG/AS1411/A21 GNP that maintained concentration-dependent behavior compared to PEG/AS1411 GNPs at 2 vs. 1 µM AS1411 treatment ($p<0.0213$).

Together with XTT and morphological data, these cell count data implied that the PEG/AS1411/A21 GNPs inhibited cell growth, a significant contributor to GBM aggression. Interestingly, 0.25 and 1.0 PEG/AS1411/A21 GNPs formulations performed similarly to PEG/AS1411 GNPs. On the other hand, 0.5 PEG/AS1411/A21 GNPs consistently performed worse than PEG/AS1411 GNPs. However, no PEG/AS1411/A21 GNP formulation enhanced the anti-GBM effects on U-87 MG cell growth after 72 hours of treatment compared to 9X PEG/AS1411 GNPs. Thus, there were no apparent increases in therapeutic effects through A21 addition into PEG/AS1411 GNPs.

4.3.2 Effects on GBM Motility

The motility and migration of U-87 MG cells are two other hallmarks of its tumorigenic potential. U-87 MG cells are readily invasive, and *in vivo* invasion of GBM cells contributes to disease progression and metastasis [203]. Therefore, the effects of 72-hour exposure of PEG/AS1411 GNPs or PEG/AS1411/A21 GNPs on the U-87 MG cell motility rate at 1 μM equivalent AS1411 concentrations were investigated (**Figure 4-5**). Only 1.0 PEG/AS1411/A21 GNPs were used in this experiment based on their efficacy demonstrated in the XTT cell viability, cell morphology, and cell count experiments. To accurately determine any differences in U-87 MG motility, cells were seeded at low densities and allowed to move freely for the entire 72-hour treatment period. In addition, only U-87 MG cells that were neither dividing nor contacting other cells were considered in the analysis.

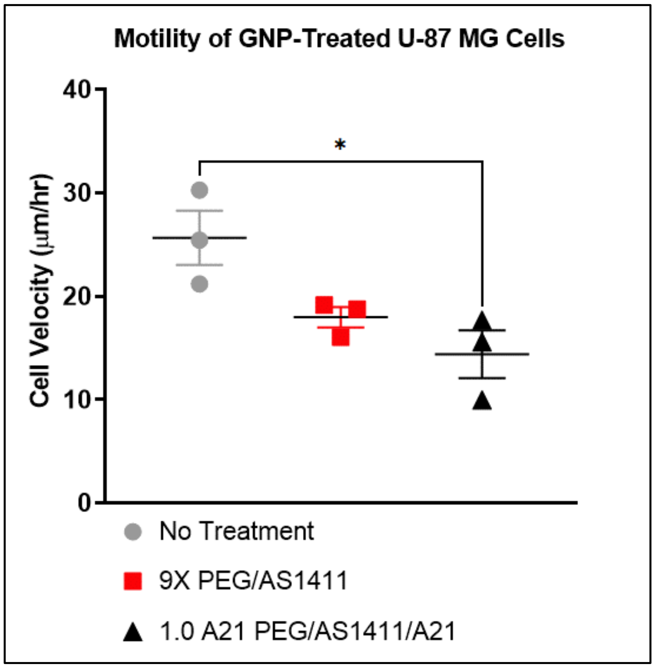

Figure 4-5: Effects on the motility rate of U-87 MG cells at 1 µM equivalent AS1411 concentrations from PEG/AS1411 GNPs and PEG/AS1411/A21. Non-treated (NT; gray bars) serve as controls. Data are presented as average cell velocity with SEM (n = 3 independent replicate groups of 25 cells in each replicate). * indicates $p < 0.05$. Analysis was completed by one-way ANOVA with Bonferonni post-hoc test (α=0.05).

Motility rates of U-87 MG cells were reduced by an average of 29.88% microns per hour in cells treated with PEG/AS1411 GNPs (17.97 ± 1.864 µm/hr) when compared to NT controls (25.63 ± 4.541 µm/hr). Additionally, average motility rates were significantly lowered in U-87 MG cells treated with 1.0 PEG/AS1411/A21 GNPs at the same (1 µM) effective AS1411 concentrations, with a 43.85% decrease in U-87 MG motility rates (14.39 ± 3.986; $p<0.0209$). Thus, 1.0 PEG/AS1411/A21 GNPs significantly reduced the motility rates of U-87 MG cells compared to NT groups. However, U-87 MG cell motility rates were not significantly reduced by adding A21 to PEG/AS1411 GNP.

4.4 Bioactivity of A21 from PEG/AS1411/A21 GNPs

4.4.1 Effects of PEG/AS1411/A21 GNP on miR-21 Expression

In GBM, increases in invasiveness are attributed to increased miR-21 [104]. Adding A21 to PEG/AS1411 GNPs is speculated to counteract this overexpression of miR-21, affecting the genetic and protein level expression of miR-21 and associated downstream proteins. To investigate this, miR-21 expression levels were measured in U-87 MG cells treated with PEG/AS1411/A21 GNPs using qPCR. Relative miR-21 expression was obtained by evaluating the expression of miR-21 transcripts compared to the expression of the small-nucleolar reference gene RNU144. The $2^{\Delta\Delta Ct}$ method reported relative miR-21 expression as a relative log2 expression. This quantification method describes miR-21 expression results as fold increases (positive values) or decreases (negative values) of miR-21 expression in terms of base 2. The conversion between base 2 and 10 values is:

$$Fold\ increase\ or\ decrease\ miR-21\ Expression\ (base\ 10) = 2^{(log2\ miR-21\ expression\ value)}$$

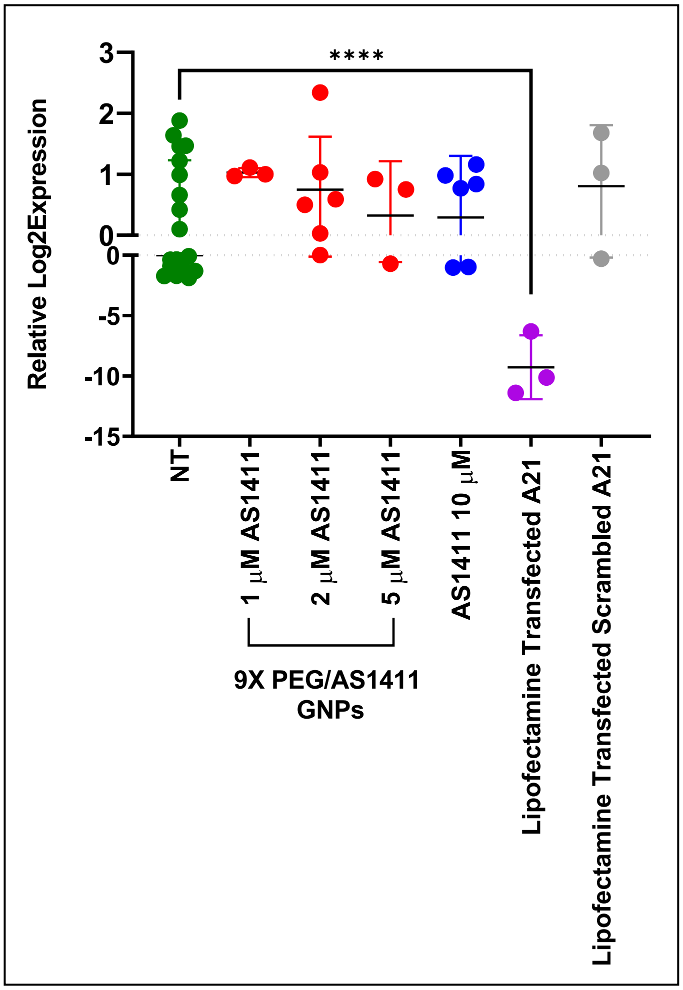

Figure 4-6: miR-21 expression levels present within U-87 MG cells post-treatment with PEG-AS1411 GNP treatments (red), NT (green), 10 μM AS1411 (blue), 10 nM Lipofectamine transfected A21 (purple), or scrambled A21 (grey) controls. GNP treatment concentrations represent AS1411 equivalence present in the GNP solution. Data are presented as individual values of average miR-21 log2expression ± SEM. **** represent $p<0.0001$ reported from one-way ANOVAs with Bonferonni post-hoc tests ($\alpha=0.05$) (n = 3 biological replicates for all treatments across all experiments; 6 total experiments were completed with independent NT controls).

First, the ability of PEG/AS1411 GNPs and controls to reduce miR-21 expression levels was evaluated (**Figure 4-6**). Controls included Lipofectamine transfected U-87 MG cells with either 10 nM A21 (5'- UUUUUUUUCAACAUCAGUCUGAUAAGC) or 10 nM scrambled A21 (5'-UUUUUUAUUCUUAAUAGUCACCGCAA). Using a scrambled control allowed the specificity of the A21 sequence toward affecting miR-21 expression levels to be examined.

Lipofectamine transfection of cells with 10 nM A21 significantly reduced miR-21 expression levels. miR-21 log2expression levels were, on average, 10.13 ± 2.6-fold times lower than NT cells (~ 1000 times lower relative to NT cells in base 10 expressions). We observed no change in U-87 MG cellular miR-21 levels in cells treated with either PEG/AS1411 GNPs, 10 μM AS1411, or scrambled A21 controls compared to NT control. This established that A21 could specifically target miR-21 transcripts, while PEG/AS1411 GNPs could not target miR-21 through AS1411 bioactivity.

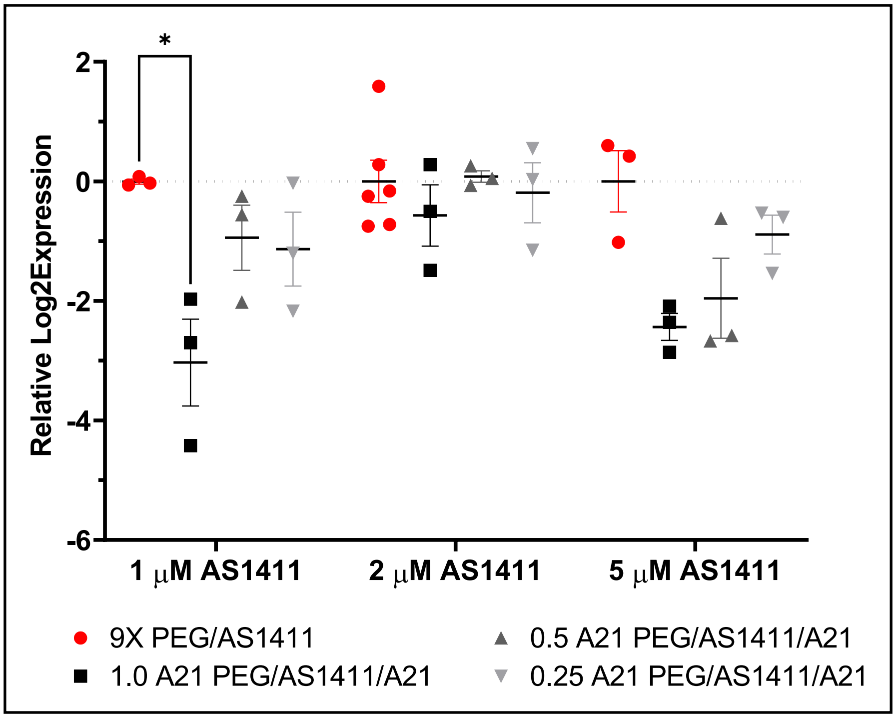

Figure 4-7: miR-21 expression levels present within U-87 MG cells post-treatment with PEG/AS1411/A21 GNP treatments (black and grey) compared to PEG/AS1411 GNP treatments (red). GNP treatment concentrations represent AS1411 equivalence present in the GNP solution. Data is presented as individual values of average miR-21 log2expression ± SEM. * represent $p<0.05$ reported from two-way ANOVAs with Bonferonni post-hoc tests (α=0.05) (n = 3 biological replicates for all treatments across all experiments).

Next, the ability of PEG/AS1411/A21 GNPs to reduce miR-21 expression was investigated **(Figure 4-7)**. 1.0 PEG/AS1411/A21 GNPs at 1 µM equivalent AS1411 significantly decreased miR-21 expression levels in U-87 MG cells compared to 9X PEG/AS1411 GNPs. miR-21 log2expression were on average 3.03 ± 1.3-fold times lower than PEG/AS1411 GNPs at the same concentration ($p<0.0108$; ~ 8.17 times lower relative to PEG/AS1411 GNP-treated cells in base 10 expression). While this qPCR data demonstrates that 1.0 A21 PEG/AS1411/A21 GNPs lowered expression levels of miR-21 in U-87 MG cells at 1 µM equivalent AS1411 compared to PEG/AS1411 GNPs, incorporating A21 into PEG/AS1411 GNPs appears to reduce the potency of A21.

The reduction in miR-21 expression was only observed in 1.0 PEG/AS1411/A21 GNP treatment groups and not in other PEG/AS1411/A21 GNP formulations. This is most likely a result of 1.0 A21 GNPs theoretically having the highest levels of A21 available on the nanoparticles. This phenomenon of the 1.0 PEG/AS1411/A21 GNPs performing the best was supported in XTT, growth, morphology, and motility assays. Each experiment showed that among the GNP formulations tested, 1.0 PEG/AS1411/A21 GNPs were the most effective at altering the hallmarks of GBM growth.

4.4.2 Protein Target Expression in PEG/AS1411/A21 GNP Treated U-87 MG Cells

Successful intracellular delivery of A21 oligonucleotides should decrease the amount of active miR-21 available within the cell environment (**Figure 4-8**), resulting in downstream effects on protein targets of miR-21. Numerous proteins associated with miR-21 have been identified and verified [20, 102, 104, 116-123, 204]. Among these proteins, PTEN and STAT3 were investigated as hallmark miR-21-associated proteins overexpressed in GBM.

STAT3 is a transcription factor that mediates cytokine IL-6 signaling and has been shown to play a role in GBM tumorigenesis, ultimately promoting the proliferation and invasiveness of gliomas. STAT3 and miR-21 closely interact, and it is believed that there is a regulatory loop between the two [129]. Therefore, it is implicated that STAT3 mediates its oncogenic activity via miR-21 and is directly involved in the regulatory control of pri-miR-21 precursors that are processed into mature miR-21 [205]. In fact, after inhibition of miR-21, it has been shown that lower levels of STAT3 expression are observed [206]. Conversely, expression levels of miR-21 have been positively correlated with the expression of STAT3 [207]. Thus, successful intracellular delivery of A21 should lead to lower STAT3 expression.

PTEN is a dual-specific phosphatase (dephosphorylating) that is usually downregulated in cancers and contributes to increased proliferation and survival of tumors. PTEN expression is suppressed in GBM and is negatively correlated with miR-21 levels. [129, 208] Thus, successful intracellular delivery of A21 should lead to a rise in the expression of PTEN.

Western Blot analysis was used to examine the expression of miR-21-associated proteins STAT3 and PTEN after treatment with PEG/AS1411/A21 GNPs or PEG/AS1411 GNPs. It is important to note that the data discussed here were inconclusive, and the quantitative effects on STAT3 and PTEN expression could not be definitively determined. This is due to the inherent limitations of western blots and gel electrophoresis coupled with cell-to-cell variability, sample size, and antibody concerns used in the analysis. Nonetheless, a qualitative analysis of STAT3 and PTEN expression can still assess whether there was successful A21 delivery via PEG/AS1411/A21 GNPs.

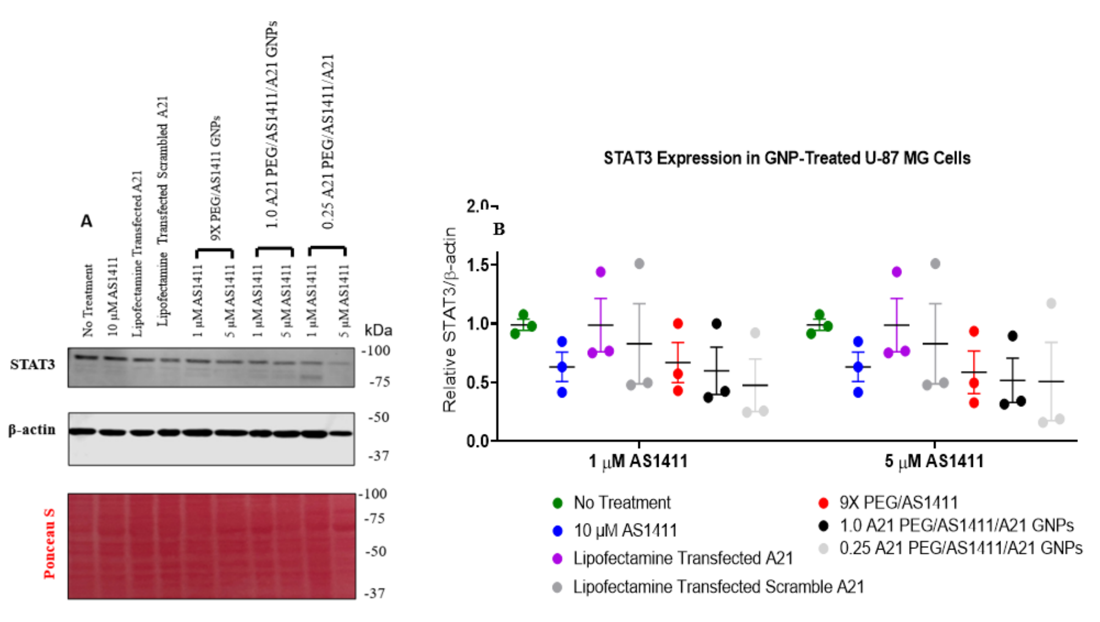

Figure 4-8: Western Blot analysis of STAT3 expression in GNP treated U-87 MG cells after 72-hour exposure. STAT3 and ß-actin (A) bands are designated by their relative sizes (kDa). Ponceau S stain shows gel loading. Densitometry measurements (B) are shown for each band (n= 3 biological replicates). Data is presented as average normalized band intensity relative to ß-actin and normalized to no treatment conditions ± SEM. Significance was investigated via two-way ANOVAs with Bonferonni post-hoc tests (α=0.05).

Representative western blot analysis of STAT3 in U-87 MG cells treated with PEG/AS1411 GNPs or PEG/AS1411/A21 is shown in **Figure 4-8A**. Full blot images of STAT3 expression are found in Appendix A (**Figure A1-2.1 – A1-2.3**). On average, STAT3 expression was lower in 10 µM AS1411 control groups (blue) compared to NT groups (**Figure 4-8B**). Given the observed decrease in metabolic activity (**Figure 4-2**) and cell growth (**Figure 4-4**) and knowing that decreases in STAT3 are implicated with lower amounts of cellular proliferation, the apparent reduction in STAT3 expression in AS1411 control groups is not surprising. However, upon conjugation of AS1411 onto

GNPs, the effects of AS1411 on STAT3 expression are not significant at either AS1411 treatment concentrations (red) when compared to AS1411 controls.

No decreases in STAT3 expression were found in Lipofectamine transfected A21 groups (purple) (**Figure 4-8B**). With no change in average expression in A21 control groups, it could suggest that other miR-21 targets may need to be investigated, that 10 nM transfection concentrations are ineffective at altering STAT3 expression, or that 72 hours of exposure is too long of a time window to establish A21 activity within U-87 MG cells. Since no changes in STAT3 expression were noted in the A21 control group, it was assumed that any results in PEG/AS1411/A21 GNP-treated U-87 MG cells were due to the bioactivity of the PEG/AS1411 components present in the PEG/AS1411/A21 GNPs. Therefore, it is unclear if adding A21 to PEG/AS1411 GNPs affects STAT3 levels. 0.5 PEG/AS1411A21 GNP syntheses were not included in this analysis due to their poor anti-GBM performance in metabolic, growth, motility, and qPCR assays compared to 1.0 and 0.25 PEG/AS1411/A21 GNPs.

Like STAT3, expression levels of PTEN within U-87 MG cells with or without PEG/AS1411/A21 GNP treatments were investigated (**Figure 4-9**). PTEN expression levels were increased for all control groups compared to NT controls (**Figure 4-9B**). This suggested that AS1411 and A21 could increase PTEN expression in U-87 MG cells. The increased effect of AS1411 on PTEN expression in U-87 MG cells agrees with other studies investigating PTEN expression in miR-21-affected breast cancers [209]. However, caution must be taken in interpreting this data due to high variability and low sample size.

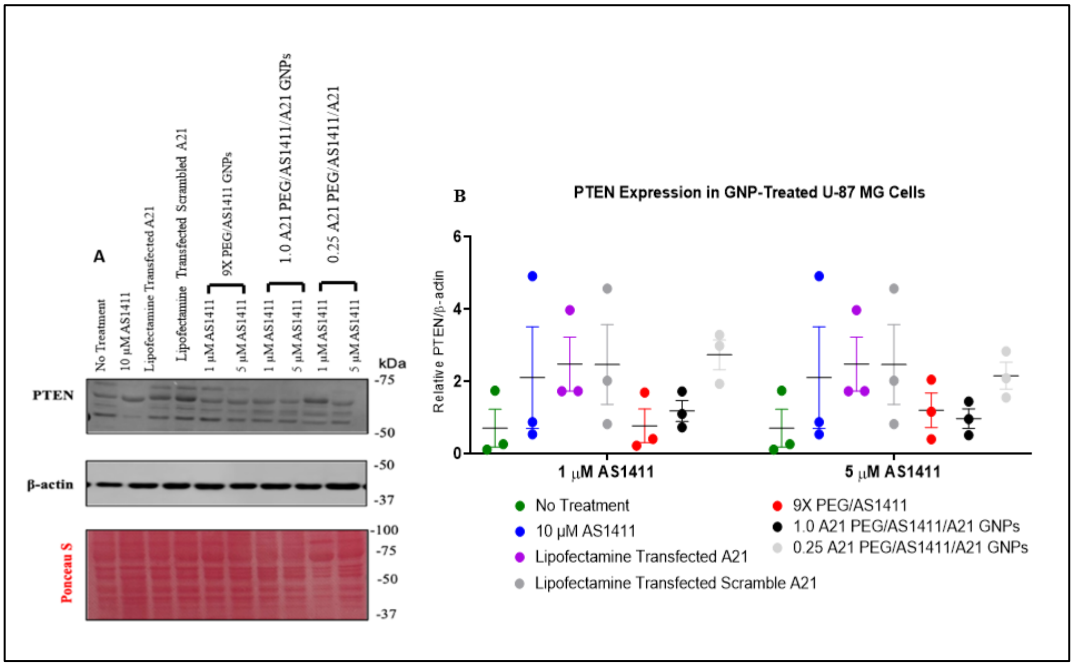

Figure 4-9: Western Blot analysis of STAT3 expression in GNP-treated U-87 MG cells after 72-hour exposure. PTEN and ß-actin (A) bands are designated by their relative sizes (kDa). Ponceau S stain shows gel loading. Densitometry measurements (B) are shown for each band (n= 3 biological replicates). Data are presented as average normalized band intensity relative to ß-actin and normalized to no treatment conditions ± SEM. Significance was investigated via two-way ANOVAs with Bonferonni post-hoc tests (α=0.05).

In cells subjected to 9X PEG/AS1411 GNP and PEG/AS1411/A21 GNP treatments, PTEN expression levels were similar in expression levels to NT controls. Despite a slight increase in PTEN expression levels in 0.25 PEG/AS1411/A21 GNPs, it was difficult to claim a definitive effect due to A21 inclusion in PEG/AS1411/A21 GNPs. Full blot images of PTEN expression are found in Appendix A (**Figure A1-1.1 – A1-1.3**)

4.5 Conclusions

PEG/AS1411/A21 GNPs were stable, as indicated by zeta potential, hydrodynamic size, and UV-VIS GNP characterization. PEG/AS1411/A21 GNPs produced effects on the metabolic activity, cellular morphology, growth, and motility of U-87 MG cells. However, across all experiments, PEG/AS1411/A21 GNPs performed similarly to PEG/AS1411 GNPs in anti-GBM metrics. The presence of A21 in PEG/AS1411/A21 GNPs enhanced the anti-GBM activity of the nanoparticle formulations on U-87 MG cellular motility. While miR-21 levels were lowered due to PEG/AS1411/A21 GNP treatment, the ability of PEG/AS1411/A21 GNPs to affect downstream miR-21 associated proteins, STAT3 and PTEN, was unclear. Nonetheless, PEG/AS1411/A21 GNPs containing an A21 oligonucleotide had an impact expression of miR-21. The subsequent chapter will assess the PEG/AS1411/A21 GNPs in an *in vivo* orthotopic mouse model of GBM.

CHAPTER 5

IN VIVO PERFORMANCE OF PEG/AS1411 and PEG/AS1411/A21 GNPS

5.1 Introduction

Before clinical development of new therapies can proceed, *in vivo* testing is required to show efficacy and safety upon the interaction of the candidate therapeutic with the native biological environment. This allows for analysis within a more realistic version of the native biology of the target disease. In the context of GBM, multiple *in vivo* models exist. These include cell line xenografts, patient-derived xenografts, genetically engineered mouse models, and syngeneic mouse models—each with unique advantages [16]. For *in vivo* orthotopic models of GBM, the ability of therapies to cross the BBB is directly tested to determine the ability of new therapeutics to target and reach the tumor in the brain.

Genetically engineered and syngeneic mouse models boast a high degree of biological relevance. Still, they are not practical for screening new therapeutics due to their complex initiation, lack of tumor heterogeneity, and the use of immunocompetent mice (syngeneic models). Thus, these models are more suited for tumor initiation and progression studies or immunological research. On the other hand, xenograft models offer quick and easy methods to screen new therapeutics for GBM research.

Cell line xenograft (CLX) models establish GBM tumors via commercially available GBM representing cell lines (U-87 MG, U251, T98G, and A172). These cell lines are the most used for *in vitro* and *in vivo* research into GBM. CLXs have high engraftment and growth rates, relatively good reproducibility, and reliable disease growth and progression [210]. However, models of these types do not show single-cell invasion, tumor necrosis, or microvascular proliferation [16, 211]. They are also believed to have different phenotypes from native GBM tumors [16]. While these models are suitable for a first step in evaluating the efficiency of therapeutics, additional models are needed to investigate in-depth anti-GBM properties of potential therapeutics.

Patient-derived xenograft (PDX) models are established using GBM tumorspheres from cultured cells harvested from GBM patients [212]. As such, PDX models are helpful for translational research as they retain the genetic and histological features of the primary tumors they are derived from. Therefore, PDX models are superior in investigating and verifying molecular changes and signaling pathways [16]. However, only 10-20% of derived tumor cells are cultured successfully for tumor implantation [210]. Whether CLX or PDX-derived, xenograft models are created either orthotopically (in the native region—*i.e.*, the brain for GBM) or subcutaneously (under the flank of skin) [213]. While subcutaneous xenografts are less technically difficult in their deployment, orthotopic xenografts closely mimic the biological and clinical environment of tumors [16].

In selecting the kind of *in vivo* model with which to investigate the synthesized PEG/AS1411 or PEG/AS1411/A21 GNPs, the focus was placed on preliminary questions that needed to be answered from *in vivo* models: (1) do both types of GNPs reach their intended target after passing through the BBB?, (2) does the accumulation of either GNP type affect tumor progression?, and (3) do any changes to tumor progression confer a benefit on survivability? Since orthotopic models could be created and grown quickly in the brain, an orthotopic CDX nude mouse model was chosen for initial *in vivo* testing of PEG/AS1411 and PEG/AS1411/A21 GNPs.

Orthotopic xenograft tumors were established in female three-week-old nude mice via surgical implantation of Luciferase-modified U-87 MG cells using stereotactic equipment under the courtesy and guidance of Dr. Brian Williams at UofL. The subsequent analysis of treatment, tumor progression, and survivability was then completed over 67 days post-tumor implantation (the maximum amount of time allowed by the IACUC).

This model was advantageous due to the presence of the BBB and its biological relevance to evaluating PEG/AS1411/A21 GNPs as anti-GBM therapies. PEG/AS1411 GNPs were synthesized in the 9X configuration from Chapter 3, where AS1411 and PEG are loaded onto the GNP in a 9:3 ratio. PEG/AS1411/A21 GNPs from Chapter 4 were synthesized in the 0.25 PEG/AS1411/A21 GNP formulation, where the PEG/AS1411 GNPs were modified with 0.25 moles of A21 for every mole of PEG on the GNP surface.

5.2 Effectiveness of GNP Delivery to GBM Tumors

5.2.1 Biodistribution of GNPs *in vivo*

To determine if our GNP formulations can pass through the BBB, we examined the *in vivo* biodistribution of both PEG/AS1411 GNPs and PEG/AS1411/A21 GNPs in our orthotopic mouse GBM model. Intracranial GBM tumors were established on day 0. GBM tumors were established by day 11 (verified with bioluminescent imaging, discussed in the next section). Starting at day 11, *i.p* injection of either PEG/AS1411 GNPs or PEG/AS1411/A21 GNPs at a dose of 1 mg equivalent AS1411/kg mouse body weight began and was continued for 12 consecutive days. Mice were followed until sacrificed (at day 67 post-tumor implantation or sooner if signs of neurological distress were evident). Au content (ng/mL per dry weight of tissue) within the brain and tumor were determined by ICP-MS.

ICP-MS data confirmed that PEG/AS1411 GNPs accumulated within brain and tumor tissues (**Figure 5-1A**). Tumor samples had an average of 12.71 ± 14.40 times more Au present than in the brain (**Figure 5-1B**; black bar), implying selective retention of PEG/AS1411 GNPs in tumors. Likewise, PEG/AS1411/A21 GNPs accumulated in tumor tissues with an average of 14.69 ± 4.078 times more Au than in the brain (**Figure 5-1B:** red bar). The accumulation of GNPs represents an average of 3.12% and 1.12% retention of the total administered PEG/AS1411 GNPs and PEG/AS1411/A21 GNPs (**Figure 5-2**). This indicates that administered PEG/AS1411 and PEG/AS1411/A21 GNPs most likely accumulated in other organs (*e.g.*, liver and kidney). This low accumulation within the brain and tumor tissues agrees with studies investigating the biodistribution of GNPs modified with PEG constructs [214].

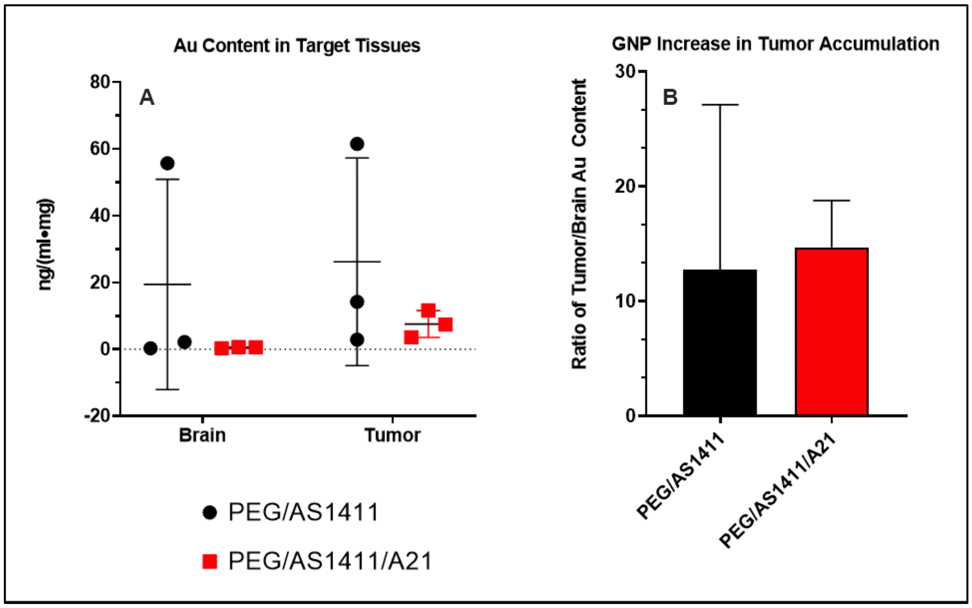

Figure 5-1: Biodistribution of PEG/AS1411 and PEG/AS1411/A21 GNPs *in vivo*. Brain and tumor tissues were collected after sacrifice and investigated for Au content using ICP-MS (n=3 for each GNP treatment). Amounts are the average concentration of Au per mg of dry weight (A). Fold increase in accumulation in tumor tissue vs. brain tissue of each GNP type is presented in (B). Significant differences were investigated by two-way ANOVA with $\alpha = 0.05$ with Bonferonni post-hoc tests.

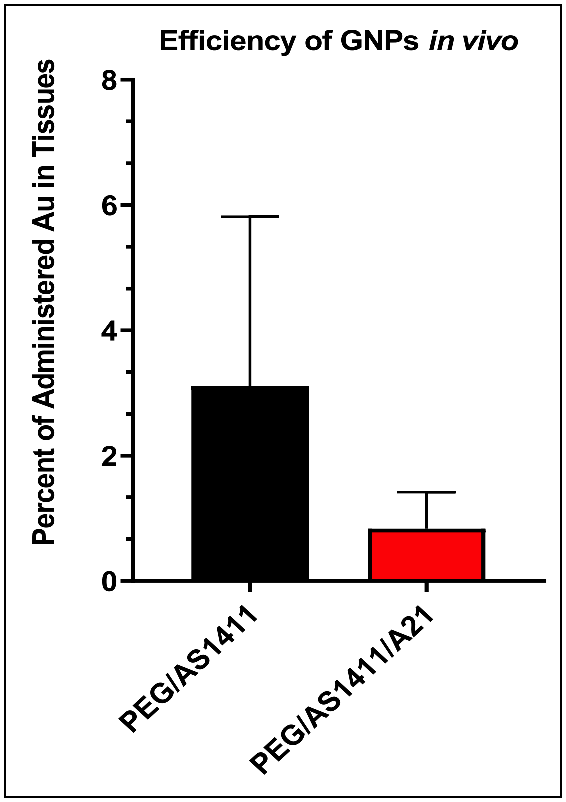

Figure 5-2: Percentage of administered Au retained within brain and tumor tissues. Harvested tissue (n=3 for each GNP treatment) was evaluated for Au content via ICP-MS and concentrations compared to the total delivered Au from GNPs across the 12-day treatment window. Values are the average cumulative percentage retained within tissues ± standard deviation. Significant differences were investigated by student t-tests with $\alpha = 0.05$.

Some precautions must be considered when evaluating these data. Due to cost considerations, the study did not include non-treated control mice. It was assumed that the presence of Au in brain tissue would be unique to animals treated with GNP and that all Au detected in the brain would be due to GNP treatments. The results suggest that both PEG/AS1411 GNPs and PEG/AS1411/A21 GNPs crossed the BBB. Once crossing of the BBB was confirmed, a second *in vivo* study was performed to evaluate GNP efficacy by following GBM tumor progression and the survivability of mice.

5.2.2 Tumor Progression *in vivo*

To determine whether tumor progression is affected by the accumulation of PEG/AS1411 GNPs or PEG/AS1411/A21 GNPs, mice with orthotopic GBM tumors were treated with GNP formulations at 1 mg equivalent AS1411/kg mouse body weight began and was continued for 12 consecutive days (n=3 mice for each group). Luciferase-transfected U-87 MG cells allowed for bioluminescent imaging of the tumor area to evaluate tumor progression pre- and post-GNP treatment dates. On days 9, 11, 22, 28, and 36 after tumor implantation, mice were injected with Luciferin (150 mg Luciferin/kg body weight), bioluminescent images were taken, and photon counts were tallied. While not quantitative, photon counts varied proportionally with the amount of bioluminescent U-87 MG cells and were used to assess tumor sizes and progression throughout the study, **Figure 5-3**.

These data show that GBM tumors for all mice expressed similar photon counts on day 9 after tumor implantation with an average of 65k total photon counts per animal (**Figure 5-3;** the first set of data points). This agrees with other work detailing orthotopic xenograft establishment in GBM [215, 216]. A decrease in photon counts for all groups to an average of 9K was seen on day 11 (**Figure 5-3**; the second set of data points), implying possible tumor shrinkage or confounding factors attributed to variations in tumor engraftment or sensitivity of Luciferin imagining to animal positioning and skull thickness. All reported images show a visible tumor in all mice (**Figures 5-4** through **5-6**). Regardless, photon counts on this day are similar, and all groups had reduced photon counts implying similar tumor growth patterns across all tumors.

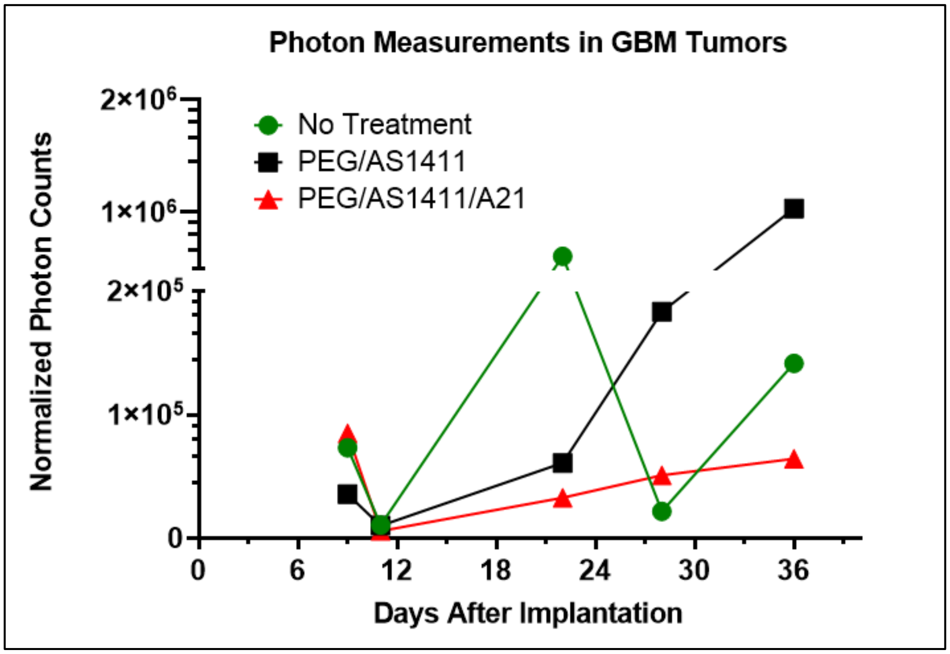

Figure 5-3: Timelapse of photon counts in GNP and control-treated mice. Mice (n=3 per group) bearing orthotopic GBM tumors were imaged on days 9, 11, 22, 28, and 36. Data are presented as mean photon count on imaging day.

Once GBM tumors were established on day 11, GNP and control treatments began on this day. Mice were imaged again on day 22 (the last day of treatment). On day 22, photon counts increased 56.00-fold times in PBS control (NT) mice (**Figure 5-3**; the third set of data points). Smaller fold increases were also observed in mice receiving PEG/AS1411 GNPs (5.06-fold increase) and PEG/AS1411 /A21 GNPs (4.61-fold increase; **Figure 5-3**; the third set of data points).

Imaging continued through days 28 and 36 to see if GNP treatments effects continued past cessation of treatments (**Figure 5-3**; the fourth and fifth set of data points). On day 28 post-implantation (6 days post-treatment window), photon counts from NT mice decreased compared to day 22 due to unknown reasons. From day 22 to 28, photon counts for mice treated with PEG/AS1411 GNPs increased 2.0-fold more than PEG/AS1411/A21 GNPs, suggesting an increased benefit of adding A21 to the nanoparticle formulations. This was further supported on day 36, where photon counts increased in mice treated with PEG/AS1411 GNPs compared to day 28, indicating pronounced tumor growth post-treatment. Photon counts seemed to level off in mice treated with PEG/AS1411/A21 GNPs on this same day. It is important to note that by this day, only one mouse in this treatment group had survived.

Care must be taken when examining photon count data due to the low number of mice (3) in each group. As such, the power of this study is low. Effect size analysis indicates that only 22.7% of the differences seen in the photon count data on tumor progression are explained by GNP treatments. The NT group initially had an n=7, but due to factors of the U-87 MG cells at the time of implantation, GBM tumors did not progress for 4 mice. Additionally, **Table 5-1** shows the standard error of the mean (SEM) associated with photon counts.

Table 5-1

SEM of photon count measurements from GNP and control-treated mice

Treatment Type	Imaging Day	Standard Error of the Mean (SEM) in Photon Counts		
		Average	SEM	Percentage SEM
NT	9	7.3E+04	5.14E+04	70.06%
	11	1.1E+04	4.52E+03	42.31%
	22	6.1E+05	5.96E+05	97.93%
	28	2.2E+04	1.24E+04	57.29%
	36	1.4E+05	7.44E+04	52.50%
PEG/AS1411 GNPs	9	3.6E+04	2.56E+04	72.06%
	11	1.0E+04	2.66E+03	26.48%
	22	6.1E+04	4.79E+04	78.65%
	28	1.8E+05	1.63E+05	88.91%
	36	1.0E+06	8.38E+05	81.03%
PEG/AS1411 /A21 GNPs	9	8.5E+04	7.45E+04	87.54%
	11	5.8E+03	2.98E+03	50.91%
	22	3.3E+04	1.88E+04	57.32%
	28	5.1E+04	2.88E+04	56.59%
	36	6.4E+04	-	-

Bioluminescent images supported the photo count trends observed on days 9, 11, and 22. (**Figure 5-4** through **Figure 5-6**). One mouse in the NT group (**Figure 5-4**) appeared to have complete tumor regression. Given that the success rate of each xenograft engraftment in mice is 80-90% [217], this result is not unusual. Still, it does deflate the average photon counts reported for the NT mice beginning on day 22 post-implantation. Regardless, photon counts showed that both GNP treatment types decreased apparent tumor size during the treatment window.

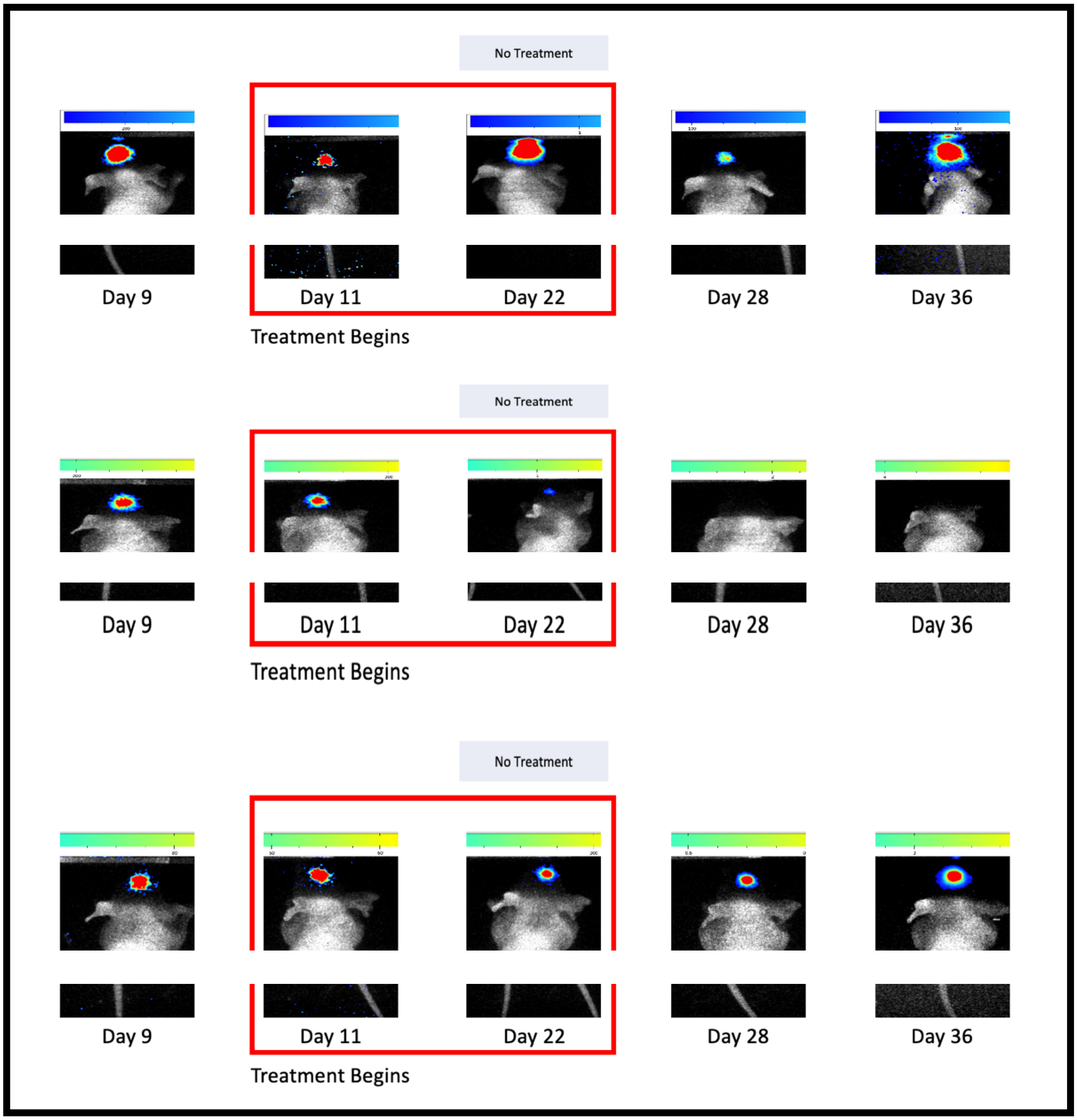

Figure 5-4: Photon images from non-treated mice

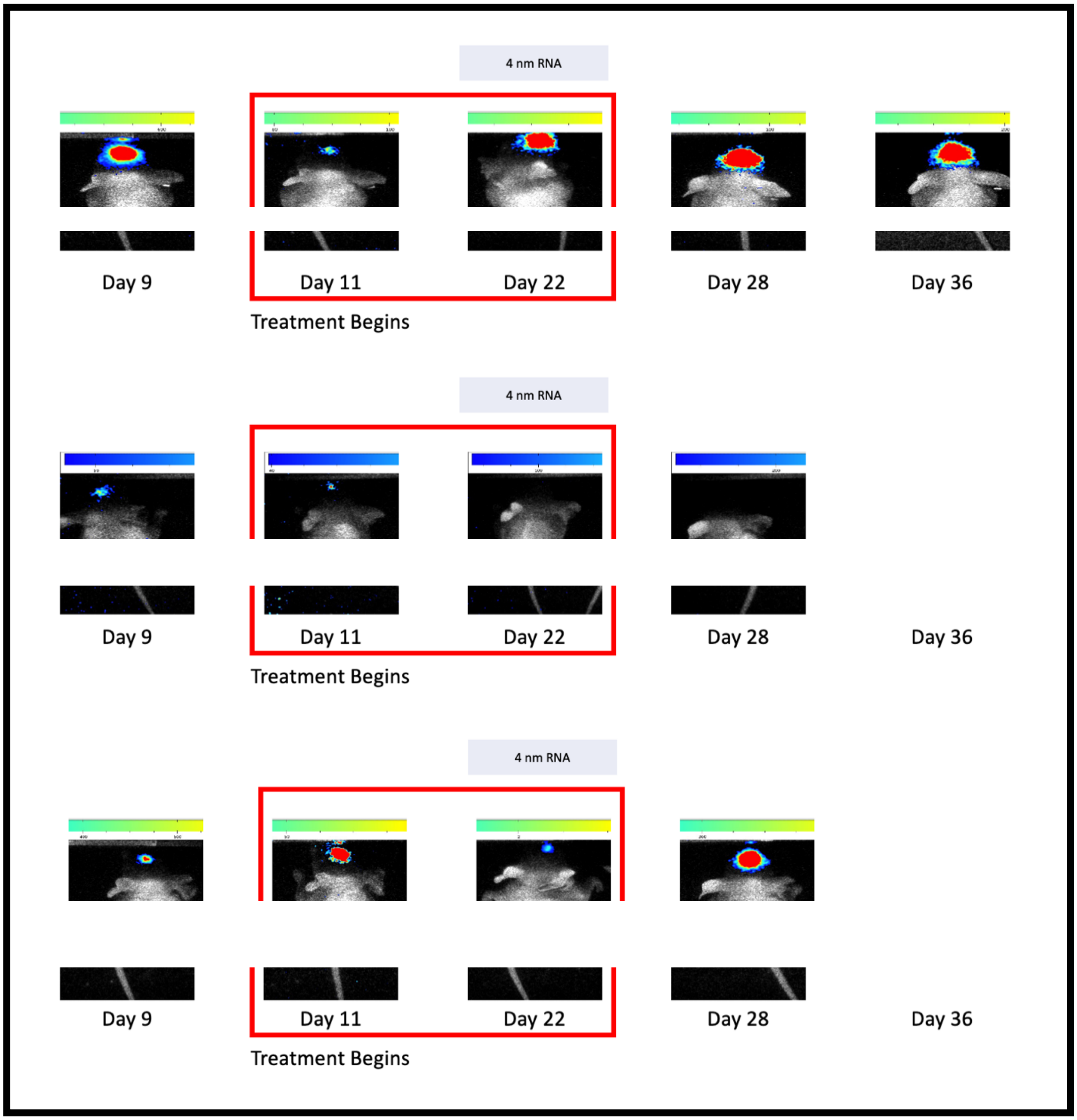

Figure 5-5: Photon images from PEG/AS1411/A21 GNP-treated mice

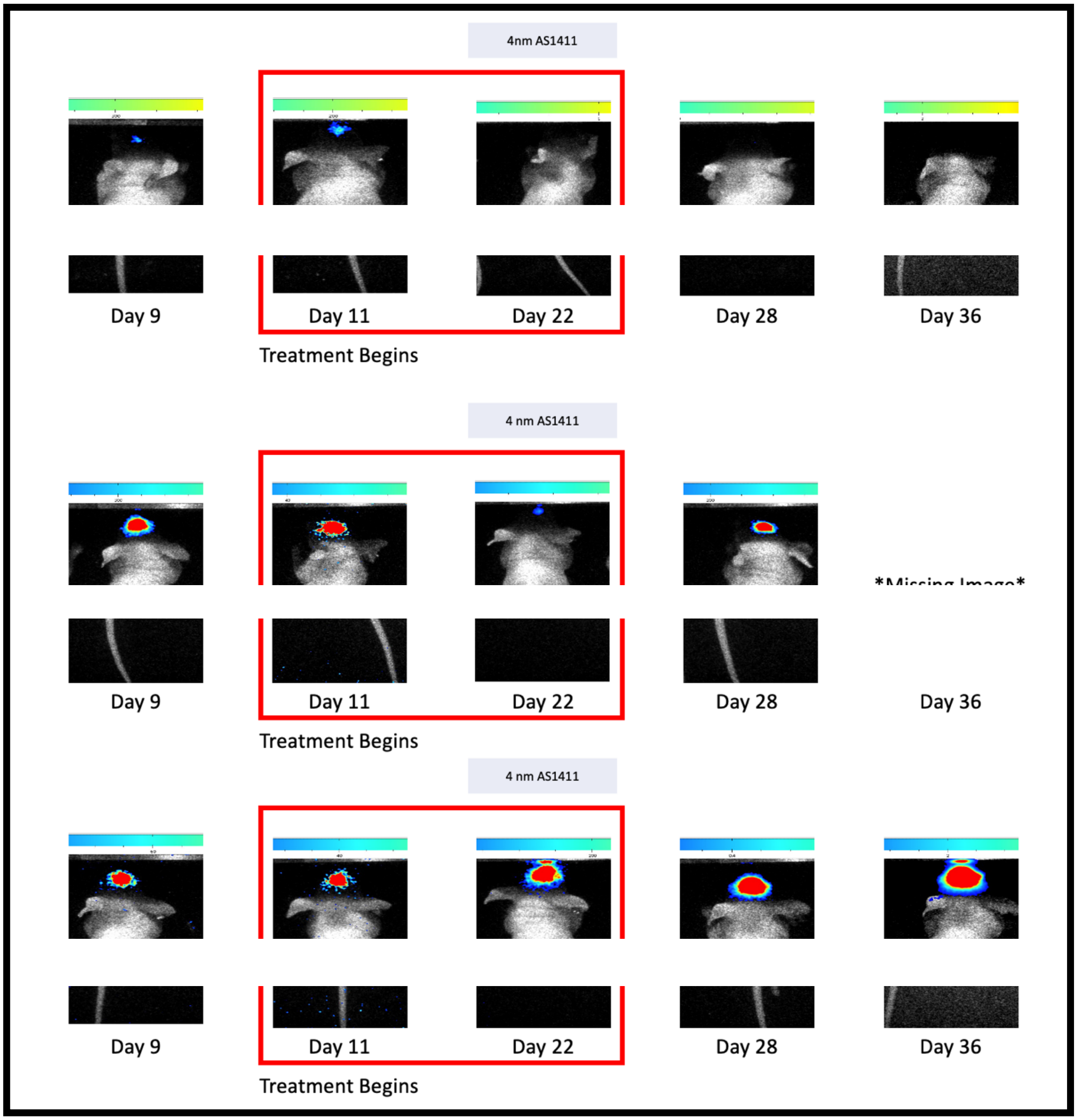

Figure 5-6: Photon images from PEG/AS1411 GNP-treated mice

The *in vivo* efficacy of PEG/AS1411 GNP and PEG/AS1411/A21 was investigated further by examining the brain and tumor weights at the time of sacrifice. All mice treated with PEG/AS1411 GNPs had tumors with an average dry weight of 14.37 ± 6.035 mg (**Figure 5-7A**). Mice treated with PEG/AS1411/A21 GNPs had average weights of 13.90 ± 14.16 mg.

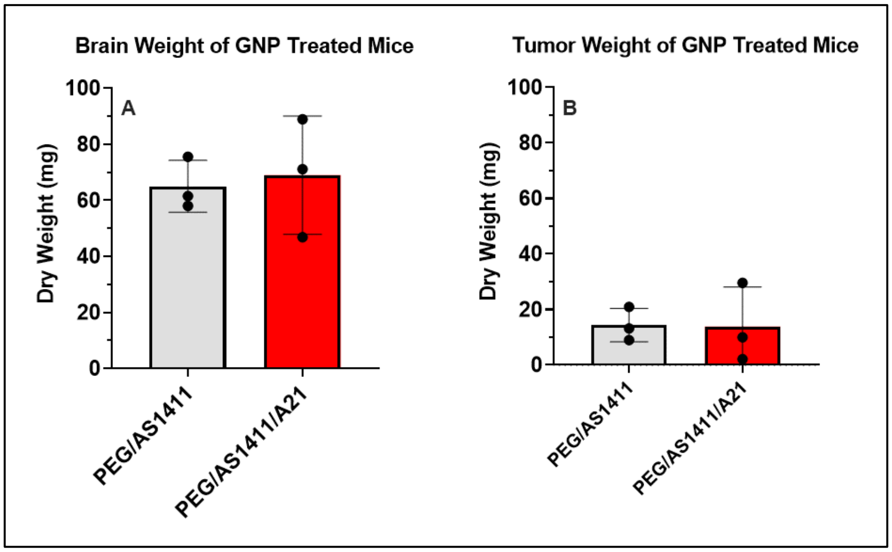

Figure 5-7: Weights of brain and tumor tissues in GNP-treated mice after sacrifice. Values are presented as an average weight (n=3) with standard deviation. Statistical significance was determined via student t-test.

From tumor weights in **Figure 5-7B**, we see that it is likely that one mouse in the PEG/AS1411/A21 GNP treatment group that initially gave no bioluminescent signal (**Figure 5-5**; second row) most likely never developed a tumor. Additionally, this mouse presented with no visible tumor at harvesting; thus, "tumor tissue" was acquired from the assumed growth area. This resulted in the lowest result in dry weight in **Figure 5-7**. Given that the early bioluminescent images showed a small signal for tumor formation, it is plausible that this tumor disappeared due to the PEG/AS1411/A21 GNP treatments.

Tumor weight data suggest that both GNP formulations performed similarly based on post-sacrifice tumor weight.

5.2.3 Survivability of GNP Treated Mice

To determine if GNP treatments affected tumor progression influenced by GNP, the survivability of each mouse was tracked for up to 67 days, as per IACUC guidelines, **Figure 5-8**. Mice were sacrificed once they presented with health concerns and complications due to GBM tumors. Mice still surviving on day 67 were sacrificed. NT mice survived until days 32, 43, and 67, **Figure 5-8A**. Results are also presented without the mouse in the NT group that did not have tumor progression, **Figure 5-8B.** Overall survivability times agree with the literature average median survival of mice bearing orthotopic GBM tumors expected to be between 28-35 days [218-220].

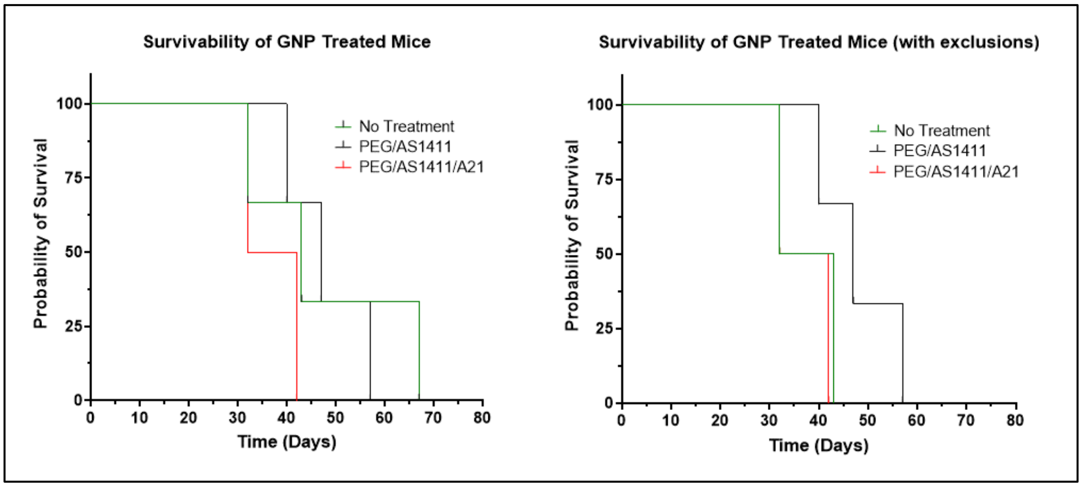

Figure 5-8: Survivability of GNP-treated Mice up to 67 days.

Mice treated with PEG/AS1411 GNPs survived an average of 47 days compared to 37.5 days in NT mice (trending towards significance with *p*<0.2773). This was most likely driven by mice with relatively small tumors in this group based on bioluminescent imaging. Interestingly, in the data with the NT exclusion, PEG/AS1411/A21 GNP treatment group showed survivability like the NT groups (37 days on average). Thus, PEG/AS1411/A21 GNPs conferred no apparent survival benefit.

5.3 Conclusion

Establishing orthotopic xenograft GBM tumors with Luciferase-transfected U-87 MG cells in three-week-old nude mice allowed for investigating the performance of PEG/AS1411 GNPs and PEG/AS1411/A21 GNPs. Mice were implanted with cells on day 0 and imaged through day 36 to determine tumor progression. GNP treatments began on day 11 and lasted for 12 days. Survivability was evaluated through day 67. Upon sacrifice, tumor weights and biodistribution (via ICP-MS) were measured. Tumors were established in most mice, and both GNP types accumulated in brain and tumor tissues, showing that both GNP types could cross the BBB. PEG/AS1411 GNPs were retained by brain and tumor tissues more than PEG/AS1411/A21 GNPs. However, only mice treated with PEG/AS1411 GNPs had an extended benefit on survivability.

Bioluminescent images of mice treated with PEG/AS1411/A21 GNPs implied either that tumors in this group had progressed too much before treatment and affected the survivability of the mice or that PEG/AS1411/A21 GNPs were mildly toxic. However, this toxicity directly contradicts photon count, biodistribution, and tumor size measurements. Given that synthesizing PEG/AS1411/A21 GNPs is completed with sterile, pharmaceutical-grade solutions and chemicals, these contradictory results are caused by the inherent toxicity of PEG/AS1411/A21 GNPs or the small sample size in the study. Reevaluating power analyses to see a significant impact on overall survivability, the sample size of each group needs to be increased from 3 mice to 17, increasing the power to a minimum of 80%. Overall, survivability does suggest an increased benefit because of PEG/AS1411 GNPs. To avoid confounding factors from tumors and minimize contradicting results, further experiments should aim to have uniform tumor engraftment or stratified groups based on tumor size to examine the effects of GNP types adequately. In *vivo* data suggests that PEG/AS1411 GNPs confer the best benefit to overall survival.

CHAPTER 6

CONCLUSIONS AND FUTURE DIRECTIONS

6.1 Conclusions

GBM is hallmarked by increased cellular proliferation and motility, contributing to its clinical aggressiveness. Current treatments include radio- and chemo-therapies which have extended the prognosis of GBM. However, these treatments are not specific to tumor tissues and do not consider the cellular heterogeneity of GBM. The heterogeneity of GBM arises due to the phenotypic expression of multiple GBM cell subtypes at different times within tumors. This results in genomic complexities that reduce the efficiency of radio- and chemo-therapies and lead to the common recurrence of GBM. The presence of the BBB increases the difficulty of treating GBM with most standard chemotherapies due to the tight regulation of which molecules can access the central nervous system.

The deregulation of cell-signaling pathways can promote tumorigenic pathways involved in GBM proliferation, migration, and survival. These pathways have numerous shared control points using signaling and regulatory molecules, including proteins and miRNA. The involvement of these molecules in multiple tumorigenic processes makes them potential targets for therapeutic intervention. In GBM, nucleolin and miR-21 are examples that have gained interest as targets for GBM therapies.

Nucleolin interacts with cell-signaling pathways such as Ras and EGFR signaling, ultimately contributing to GBM tumorigenesis. miR-21 is an oncogenic miRNA interacting with multiple protein targets promoting GBM progression. Thus, targeting these molecules can have profound anti-GBM implications affecting GBM cellular proliferation, migration, and survival.

Oligonucleotide therapies such as AS1411 and A21 can target nucleolin and miR-21 molecules. However, their practical use is poor due to their rapid degradation/excretion and inability to cross the BBB *in vivo*. Incorporating oligonucleotides into GNP nanotherapy systems can help increase their effectiveness against GBM due to increased stability and retention within GBM tumor tissues. GNPs offer a robust platform for new therapies bearing AS1411 for anti-GBM applications. Moreover, the anti-GBM behavior of A21 has been investigated in numerous studies. Thus, combining AS1411 and A21 onto GNPs offers a promising approach for developing new anti-GBM therapeutics.

Here we have chosen the DNA aptamer AS1411 based on its proven bioactivity against cancers of many types, including GBM. 4 nm GNPs were conjugated with AS1411 and a PEG linker molecule. This PEG linker allowed further modification of PEG/AS1411 GNPs with A21 oligonucleotides. The resulting PEG/AS1411 GNPs were optimized based on the PEG: AS1411 ratio on the GNP surface. PEG/AS1411 GNPs were stable, as evidenced by zeta potential, PDI, and hydrodynamic size measurements. These measurements, along with anti-proliferative activity and GNP effects on U-87 MG cellular morphology, aided in selecting 9X AS1411/PEG GNPs (3 AS1411 for every 1 PEG loading onto the GNP surface) as the most stable and efficacious nanoparticle formulation.

9X PEG/AS1411 GNPs were conjugated with A21 oligonucleotides to produce a PEG/AS1411/A21 GNP to couple the cancer targeting/therapeutic properties of AS1411 with the potential of A21 to modulate GBM gene expression pathways. GNPs with three different PEG: A21 loading ratios were synthesized and evaluated for physicochemical characteristics and anti-GBM activity. Conjugation of A21 to the PEG/AS1411 GNPs decreases the particle zeta potential, and hydrodynamic diameters with no significant changes in PDI. *in vitro* testing of PEG/AS1411/A21 GNPs showed similar performance in altering GBM cellular growth, morphology, and motility compared to 9X PEG/AS1411 GNPs. 1.0 PEG/AS1411/A21 GNPs (1:1 A21:PEG ratio) significantly reduced miR-21 transcripts, indicating the possibility of direct modulation of GBM gene expression at the translational level. While PEG/AS1411/A21 GNPs did not show higher anti-GBM activity compared to 9X PEG/AS1411 GNPs, the successful delivery of anti-miRs could have future applications with other nanoparticle systems.

PEG/AS1411 GNPs, with and without A21, were also tested in an *in vivo* GBM model. 3-week-old nude mice bearing CDX-derived, orthotopic GBM tumors were treated with 9X PEG/AS1411 GNPs or 0.25 PEG/AS1411/A21 GNPs. Both formulations were found to cross the BBB based on their presence in GBM tumors post-mortem. Mice in the 9X PEG/AS1411 GNP treatment group survived longer compared to NT mice. While PEG/AS1411/A21 GNPs showed uptake in GBM tumors as well, results were inconclusive due to limitations in study design and resource availability. Therefore, it is undetermined whether adding A21 to PEG/AS1411 GNPs confers a statistically significant survival benefit in this *in vivo* model.

Ultimately, the design and synthesis of a PEG/AS1411/A21 GNP nanoparticle system have been established, and its performance has been evaluated in *in vitro* and *in vivo* models of GBM. The suggested future directions below aim to develop a plan for the clinical translation of the PEG/AS1411 GNP. The adaptability of the design also confers the benefit of creating aptamer-based therapies using GNPs for many diseases with various anti-miR oligonucleotides.

6.2 Future Experimental Directions

6.2.1 Drug Release Kinetics

Understanding the drug delivery mechanisms of nanoparticle systems is necessary to understand their behavior *in vitro* and *in vivo*. PEG/AS1411/A21 GNP is assumed to retain the AS1411 and PEG molecules on the GNP surface, bound to the GNP through thiol linkages upon cellular internalization. The bond strength of the Au-thiol linkage is close to that of covalent bonds. However, the system should allow for releasing A21 from the GNP surface. This is due to the ester bonds that link A21 to the surface-bound PEG molecules. The ester linkage is acid labile and should impart a release mechanism for A21 upon internalization by the lower pH of cell endosomal compartments. This acidic environment should allow for the subsequent release of A21 oligonucleotides through hydrolysis reactions, allowing them to enter the cytosol to find their therapeutic miR-21 targets.

Confirming this pH sensitivity would allow a more thorough characterization of the PEG/AS1411/A21 GNP system. This could be accomplished by exposing GNPs to buffers of different pH ranges from 1.0 – 7.0 (typical pH values seen *in vitro* are 4.5-6.5) and measuring their RNA release over time [224]. An ideal experimental setup would normalize nanoparticle concentration to the effective concentrations of AS1411 (1, 2, or 5 μM in release solution) and measure RNA release over 72 hours at pre-determined intervals. RNAs could be fluorescently labeled for facile measurement by a fluorometer or fluorescent-based assay. Comparison of measured fluorescent intensity to an established concentration curve would allow quantification of the released RNA.

The A21 release data could then be fitted to drug release models such as zero order (constant rate), first order (slow and steady release), Higuchi (release from a porous system), Hixson Crowell (release from a non-constant size system), Korsmeyer-Peppas (release from a polymer; determines the mechanism of release), Baker-Lonsdale (release from the spherical system), or Weibull (dissolution system), detailing the specific release profile of conjugated A21, or other conjugated anti-miRNAs.

6.2.2 Confirming Intracellular GNP Delivery

Growth and metabolic assays reported in this dissertation showed alterations to the characteristics of U-87 MG cells due to the antiproliferative ability of PEG/AS1411 and PEG/AS1411/A21 GNPs. Examining intracellular Au content can confirm that these data result from GNP delivery. Similarly to XTT measurements, U-87 MG cells could be treated with various GNP formulations for the entire 72-hour period and then prepared for ICP-MS measurement by digesting cell pellets with aqua regia, followed by dilution for measurement [225]. To accompany quantitative data, silver staining of GNP-treated U-87 MG cells can be accomplished and imaged to compare Au content in intracellular compartments [226].

6.2.3 Confirming Macropinosome Escape

Because of the effects seen on U-87 MG growth, motility, miR-21 expression, and miR-21 protein target expression upon exposure to PEG/AS1411/A21 GNPs, it is assumed that the nanoparticles can escape from macropinosome encapsulation. The mechanism of how this escape occurs has yet to be elucidated. If GNPs were conjugated with fluorescently labeled A21 or other anti-miRNAs, then live-cell imaging would allow real-time tracking of A21 or other anti-miRNAs within the cell. The location and visualization of sub-cellular compartments could be enhanced with a fluorescent lipid stain, such as Nile red, or a macropinocytosis marker, such as dextran [197]. If A21 or anti-miRNA fluorescence appears present within the cytosol and away from lipid-stained or dextran-labeled compartments, then A21 or other anti-miRNAs would have had to escape the macropinosome.

Cellular assays examining hallmarks of sub-cellular organelle escape, such as membrane destabilization, pore formation, and membrane rupture [227], could further suggest an escape from macropinosome compartments. Treating U-87 MG cells with both PEG/AS1411/A21 GNPs and ion channel inhibitors that affect acidification of endosomal compartments (bafilomycin or concanamycins) [228] could suggest that internalization of GNPs into macropinosomes is necessary as a pre-cursor to their cytosolic delivery. If acidification cannot occur, then later stages of macropinosome escape may not happen either. Thus, in U-87 MG cells treated with acidification blockers, the effects on the bioactivity within cells should be reduced. Similarly, assays investigating pore formation (based on leakage of tracer compounds) can be conducted on GNP-treated U-87 MG cells. Diffuse cytosolic staining by these tracer compounds implies that leakage from endosomal compartments is occurring and, therefore, nanoparticle escape is also possible.

One potential hurdle to the elucidation of sub-cellular trafficking of the GNPs in this study is due to the inclusion of AS1411 in the nanoparticle construct. AS1411-triggered effects on cancer cells are hallmarked by a type of cell death known as methuosis. In methuosis, macropinosomes will coalesce and mature into late-stage vacuoles and cause the cells to rupture. It is yet to be understood whether macropinosomes can merge with early and late-stage endosomes or lysosomes in the early stages of vacuole development. However, the early stages of vacuoles are decorated with late-stage endosomal markers [229]. If methuosis occurs in these studies, it would complicate the underlying goal of proving endosomal escape.

6.2.4 Modification of GNPs with other GBM-specific anti-miRs

As mentioned, miR-21 is not the only miRNA implicated in the aberrant gene expression pathways in GBM; it has been researched the longest and thus provided a valuable tool to gauge the feasibility of a PEG/AS1411/A21 GNP-based system. Other miRNAs have bioactivity within GBM, and their complementary anti-miRs could be used to alter GBM gene expression. These include miR-7 [96, 97], miR-34a [98, 99], miR-128 [100, 101], miR-10b [20, 96], and miR-93 [107, 108]. Each of these miRNAs has an anti-sense anti-miRNA that can be evaluated within the PEG/AS1411/A21 GNP system using methods described in this dissertation. To further verify the desired effects of anti-miRNAs, gain-of-function studies can be completed to show that pre-treatment recovery occurs with exogenous miRNA treatments.

6.2.5 Whole Genome Screens of U-87 MG Cells treated with AS1411/A21 GNPs

Modifications to the expression of miR-21 targets PTEN and STAT3 were used as a gauge to verify A21 delivery into U-87 MG cells. Whole genome genetic screening could be used to examine the genetic effects of PEG/AS1411/A21 GNP treatments in more detail. Gene expression profiling of messenger RNA transcripts (RNA seq) could provide global perspectives on the impact of PEG/AS1411/A21 GNPs on the U-87 MG gene expression [230]. This information could help give broader context to the action of PEG/AS1411/A21 GNPs within cell signaling mechanisms. In conjunction with GNPs bearing differing anti-miRNAs, these tools can optimize the anti-miRNA selection for creating more effective GBM therapies.

6.2.6 Pharmacokinetic Analysis of Delivered GNPs *in vivo*

Determining effective dosing within *in vivo* models can be used to determine the pharmacokinetic profiles of therapies used. The work in this dissertation focused on the biodistribution of PEG/AS1411 and PEG/AS1411/A21 GNPs only in brain and tumor tissues. Due to limited resources, the pharmacokinetic profiles of synthesized particles in blood and urine were not determined. This could be accomplished through having parallel *in vivo* studies allowing for the collection of urine and blood at pre-determined time points to understand the retention of GNPs in blood and renal excretion of GNPs. Using ICP-MS, the concentration of Au can be determined in urine and blood levels at various time points during and after nanoparticle treatments.

6.2.7 Modification of 9X Ratio Conjugated onto GNP Surface

The work in this dissertation identified the 9X ratio of PEG: AS1411 onto GNPs as the best of 3 formulations for anti-GBM applications. This loading was obtained using a ratio of 3 AS1411 for every 1 PEG molecule bound to the GNP surface. However, modulating this ratio could provide additional benefits for implementing anti-miRNA delivery. Examining multiple conjugation ratios of AS1411 and PEG (*e.g.*, 1 to 1, 2 to 1, 3 to 1) while maintaining this optimal 9X loading onto the GNP surface could provide additional benefits for anti-miRNA GNP-based GBM therapies.

6.3 Future Application Directions

Aptamers are unique because they are small DNA oligonucleotides that can form secondary/tertiary structures that confer the ability to bind to specific target ligands selectively. However, their direct use is limited by their poor ability to be delivered *in vitro* and their poor pharmacokinetics *in vivo*. The GNP system in this dissertation provided an enhanced delivery mechanism for aptamers. While AS1411 has broad applicability as a treatment for many cancers, other aptamers can also be used, although their uses could be limited to specific cancers. Additionally, once an intended disease is chosen, anti-miRs can be selected to tailor the therapeutic to specific cancer further. Investigations into using other aptamers for cancer therapeutics have focused mainly on cancers involving leukemia, lymphoma, melanoma, and GBM [231].

6.3.1 Aptamers for Acute Myeloid Leukemia (AML)

CD33 is a transmembrane protein expressed by mature myeloid cells, AML blasts, and normal myeloid progenitors. CD33-specific aptamers have shown effective anti-cancer bioactivity in AML treatments. Additional therapeutic aptamers for myeloma and leukemia applications include anti-CXCL2 Spieglemer aptamer [232] (determined safe and effective in phase II clinical trials) or CD117-specific aptamers [233] (selected selectively therapeutic, similar to AS1411). Diagnostic aptamers such as the CD38-specific aptamer [234] or sgc8 [235] could also be used in GNP systems with anti-miRNAs selected to generate a similar targeting and therapeutic nanotherapy for AML applications. Some examples of miRNAs that express bioactivity in AML currently include miR-155, miR-196b, the miR-29 family, miR223, and miR-21 [236].

6.3.2 Aptamers for Lymphoma

Aptamers are also advantageous in lymphoma applications. CD30 is a cell membrane receptor that is over-expressed in some lymphoma cells. Single-stranded CD30 aptamers bind to the CD30 receptor with a high affinity and induce apoptosis of lymphoma cells [237]. Additionally, CD30 is a potential marker for lymphomas. This could allow a CD30 aptamer-loaded GNP system with anti-miRNAs to be helpful in the context of lymphoma. Other aptamers for lymphoma could also be used, such as the BAFF-R-specific aptamer TD05 [238]. Some examples of miRNAs known to express bioactivity in lymphoma, and therefore are possibly helpful in the design of anti-lymphoma nanotherapeutics, currently include miR-17-92, miR-223, miR221, miR-155, and miR-135a [239].

6.3.3 Aptamers in Melanoma

The aptamer MRP1 has been shown to impart activity in increasing T cell melanoma infiltration, slowing tumor growth rates, and extending survival of animals [240]. Similar aptamers such as F3B [241], RAGE [242], and CD63 [243] have shown bioactivity within melanoma. These aptamers are also believed to be effective in other solid tumors due to their ubiquitous nature and specific melanoma-targeting ability. Some examples of miRNAs known to express bioactivity in melanoma currently include miR-9, miR-18b, miR-22, miR-26a, and miR-34 [244].

6.3.4 Aptamers in GBM

Additional aptamers are also implicated for use in GBM applications. TfR aptamers are designed to interact with the transferrin receptor located on the BBB. [245] These receptors are responsible for the transcytosis of drugs into the brain. Dopamine aptamers, DBA and DA20, have been used with TfR aptamers to improve the systemic administration of dopamine aptamers. TfR aptamers are thus considered a potential therapeutic target for GBM applications. However, it has yet to be widely researched how to implement TfR into specific applications outside its combined use with other therapeutic aptamers [246]. Additional aptamers have been demonstrated to cross the BBB, such as the aptamer A15 [247]. Different miRNAs in GBM tumorigenesis have been discussed previously in this dissertation.

6.3.5 Aptamers in Other Cancers and Cancer Stem Cells

Recent advances in aptamer design for other cancers involve targeting a predominantly important class of cells known as cancer stem cells (CSCs). CSCs are present in several tumor types and display an enhanced capacity to initiate tumor formation and resist therapies. Aptamers against CD133 (prominin-1), a glycoprotein widely used as CSC biomarkers, have been used to deliver doxorubicin selectively to hepatic CSCs, which inhibited CSC proliferation in mouse models of cancer. Delivery of aptamers for therapies targeting CSCs also includes aptamers against TfR, CD44, and EpCAM—three cell surface receptors overexpressed in most solid tumors [248]. Aptamers against EpCAM have been proven effective in models for colon cancer [249]. Anti-CD44 aptamers have been combined with those against EpCAM for effectiveness in models for ovarian cancer [250]. Additional interest in aptamer delivery to CSCs as therapeutics comes from recent reports of using aptamer-siRNA chimeras to deliver siRNA against STAT3 to GBM cells selectively. These aptamers, PDR3 [251] and Gint4.T [252], express anti-GBM effects that contribute to decreasing cell growth or reducing tumor formation, propagation, and invasion of GBM CSCs. Even further, the aptamer A40s [253, 254] can target EphA2 on the cell surface of GBM CSCs and inhibit their growth and migration.

6.3.6 Aptamers in Other Diseases

Aptamers can be designed for specific therapeutic targets. In the context of cancer, this target is usually over-expressed in cancer compared to non-cancerous tissues. This concept extends beyond cancer-based diseases. Non-cancerous conditions such as sickle cell disease [255], complement disorders [256], Ebola [257], HIV [258], tuberculosis [259], hepatitis [260], myocardial infarction [261], and coronary heart disease [262] all have aptamers designed to provide a therapeutic benefit in their treatment or detection. While not an exhaustive list, the feasibility of modifying our PEG/AS1411/A21 GNP-based system with aptamers for these applications can aid in detecting and diagnosing several of these diseased states. In some cases, RNA-based delivery could enhance treatments by switching out the anti-miRNA (or other anti-sense oligonucleotides of choice).

With the onset of the discovery of aptamers and their implementation across multiple cancers and diseases, it is highly desirable to streamline their use as therapeutics—including FDA approval. As of 2020, 9 aptamers designed for cancer therapeutics have undergone FDA pre-clinical trials [263], with one aptamer, Macugen, being fully FDA-approved for the treatment of age-related macular degeneration. Any one of these has the potential to modify our GNP-based system to tailor it to their desired cancer therapy.

6.3 Concluding Summary of Dissertation

The work presented in this dissertation lays the groundwork for further developments of new GNP-based anti-GBM therapies. The synthesis of PEG/AS1411 GNPs was optimized and tailored specifically for maximal anti-GBM activity *in vitro*. Moreover, PEG/AS1411 GNP *in vivo* anti-GBM action suggested the potential for these nanoparticles to confer anti-GBM benefits. A foundational PEG/AS1411 GNP synthesis framework has been established for GBM applications. Furthermore, these based nanoparticles can be used to modify further and develop more potent anti-GBM therapies incorporating additional anti-GBM molecules—allowing for more robust treatments in the fight against GBM.

REFERENCES

1. Joseph, J.V., et al., *Three-dimensional culture models to study glioblastoma — current trends and future perspectives.* Current Opinion in Pharmacology, 2021. **61**: p. 91-97.
2. Siegel, R.L., et al., *Cancer statistics, 2023.* CA: A Cancer Journal for Clinicians, 2023. **73**(1): p. 17-48.
3. Ylanan, A.M.D., et al., *Intraoperative radiotherapy for glioblastoma: A systematic review of techniques and outcomes.* Journal of Clinical Neuroscience, 2021. **93**: p. 36-41.
4. Stupp, R., et al., *Maintenance therapy with tumor-treating fields plus temozolomide vs temozolomide alone for glioblastoma: a randomized clinical trial.* Jama, 2015. **314**(23): p. 2535-2543.
5. Aldoghachi, A.F., et al., *Recent Advances in the Therapeutic Strategies of Glioblastoma Multiforme.* Neuroscience, 2022. **491**: p. 240-270.
6. Youngblood, M.W., R. Stupp, and A.M. Sonabend, *Role of Resection in Glioblastoma Management.* Neurosurg Clin N Am, 2021. **32**(1): p. 9-22.
7. Nagasawa, D.T., et al., *Temozolomide and Other Potential Agents for the Treatment of Glioblastoma Multiforme.* Neurosurgery Clinics of North America, 2012. **23**(2): p. 307-322.
8. Wu, W., et al., *Glioblastoma multiforme (GBM): An overview of current therapies and mechanisms of resistance.* Pharmacological Research, 2021. **171**: p. 105780.
9. Upadhyay, R.K., *Drug delivery systems, CNS protection, and the blood brain barrier.* BioMed research international, 2014. **2014**.
10. Xu, L., A. Nirwane, and Y. Yao, *Basement membrane and blood–brain barrier.* Stroke and vascular neurology, 2019. **4**(2).
11. Obermeier, B., R. Daneman, and R.M. Ransohoff, *Development, maintenance and disruption of the blood-brain barrier.* Nature medicine, 2013. **19**(12): p. 1584-1596.
12. Amulya, E., et al., *Nanomedicine based strategies for oligonucleotide traversion across the blood–brain barrier.* Journal of Controlled Release, 2023. **354**: p. 554-571.
13. Huang, X., et al., *Advances in antibody-based drugs and their delivery through the blood-brain barrier for targeted therapy and immunotherapy of gliomas.* International Immunopharmacology, 2023. **117**: p. 109990.
14. Rape, A., B. Ananthanarayanan, and S. Kumar, *Engineering strategies to mimic the glioblastoma microenvironment.* Advanced Drug Delivery Reviews, 2014. **79-80**: p. 172-183.
15. Giakoumettis, D., A. Kritis, and N. Foroglou, *C6 cell line: the gold standard in glioma research.* Hippokratia, 2018. **22**(3): p. 105-112.

16. Kijima, N., et al., *Wilms' tumor 1 is involved in tumorigenicity of glioblastoma by regulating cell proliferation and apoptosis.* Anticancer Res, 2014. **34**(1): p. 61-7.
17. PontÉN, J. and E.H. Macintyre, *Long term culture of normal and neoplastic human glia.* Acta Pathologica Microbiologica Scandinavica, 1968. **74**(4): p. 465-486.
18. Clark, M.J., et al., *U87MG decoded: the genomic sequence of a cytogenetically aberrant human cancer cell line.* PLoS Genet, 2010. **6**(1): p. e1000832.
19. Schulz, J.A., et al., *Characterization and comparison of human glioblastoma models.* BMC Cancer, 2022. **22**(1): p. 844.
20. Ciafre, S., et al., *Extensive modulation of a set of microRNAs in primary glioblastoma.* Biochemical and biophysical research communications, 2005. **334**(4): p. 1351-1358.
21. Ahir, B.K., et al., *MicroRNAs in glioblastoma pathogenesis and therapy: A comprehensive review.* Critical Reviews in Oncology/Hematology, 2017. **120**: p. 22-33.
22. Esquela-Kerscher, A. and F.J. Slack, *Oncomirs — microRNAs with a role in cancer.* Nature Reviews Cancer, 2006. **6**(4): p. 259-269.
23. Bortolozzi, A., et al., *Oligonucleotides as therapeutic tools for brain disorders: Focus on major depressive disorder and Parkinson's disease.* Pharmacology & Therapeutics, 2021. **227**: p. 107873.
24. Mehta, M., et al., *Oligonucleotide therapy: An emerging focus area for drug delivery in chronic inflammatory respiratory diseases.* Chemico-Biological Interactions, 2019. **308**: p. 206-215.
25. Smith, C.I.E. and R. Zain, *Therapeutic Oligonucleotides: State of the Art.* Annual Review of Pharmacology and Toxicology, 2019. **59**(1): p. 605-630.
26. Khan, S., et al., *A review on the therapeutic applications of aptamers and aptamer-conjugated nanoparticles in cancer, inflammatory and viral diseases.* Arabian Journal of Chemistry, 2022. **15**(2): p. 103626.
27. Qian, S., et al., *Aptamers from random sequence space: Accomplishments, gaps and future considerations.* Analytica Chimica Acta, 2022: p. 339511.
28. Dehghani, S., et al., *Aptamer-based biosensors and nanosensors for the detection of vascular endothelial growth factor (VEGF): A review.* Biosensors and Bioelectronics, 2018. **110**: p. 23-37.
29. Khan, S., et al., *A review on the therapeutic applications of aptamers and aptamer-conjugated nanoparticles in cancer, inflammatory and viral diseases.* Arabian Journal of Chemistry, 2021: p. 103626.
30. Ahmadyousefi, Y., et al., *Nucleic acid aptamers in diagnosis of colorectal cancer.* Biochimie, 2019. **156**: p. 1-11.
31. Nimjee, S.M., et al., *Aptamers as Therapeutics.* Annual Review of Pharmacology and Toxicology, 2017. **57**(1): p. 61-79.
32. Romano, S., et al., *Nucleolin-based targeting strategies for cancer therapy: from targeted drug delivery to cytotoxic ligands.* Drug Discovery Today, 2019. **24**(10): p. 1985-2001.

33. Fonseca, N.A., et al., *Nucleolin overexpression in breast cancer cell sub-populations with different stem-like phenotype enables targeted intracellular delivery of synergistic drug combination.* Biomaterials, 2015. **69**: p. 76-88.
34. Huang, Y., et al., *The angiogenic function of nucleolin is mediated by vascular endothelial growth factor and nonmuscle myosin.* Blood, 2006. **107**(9): p. 3564-3571.
35. Di Segni, A., K. Farin, and R. Pinkas-Kramarski, *Identification of nucleolin as new ErbB receptors-interacting protein.* PloS one, 2008. **3**(6): p. e2310.
36. Hashemi, M., et al., *Progress in targeting PTEN/PI3K/Akt axis in glioblastoma therapy: Revisiting molecular interactions.* Biomedicine & Pharmacotherapy, 2023. **158**: p. 114204.
37. Rao, R.D., et al., *Disruption of Parallel and Converging Signaling Pathways Contributes to the Synergistic Antitumor Effects of Simultaneous mTOR and EGFR Inhibition in GBM Cells.* Neoplasia, 2005. **7**(10): p. 921-929.
38. Zhang, X., et al., *PD-L1 induced by IFN-γ from tumor-associated macrophages via the JAK/STAT3 and PI3K/AKT signaling pathways promoted progression of lung cancer.* International journal of clinical oncology, 2017. **22**: p. 1026-1033.
39. Qiu, X.Y., et al., *PD-L1 confers glioblastoma multiforme malignancy via Ras binding and Ras/Erk/EMT activation.* Biochimica et Biophysica Acta (BBA) - Molecular Basis of Disease, 2018. **1864**(5, Part A): p. 1754-1769.
40. Ezzatifar, F., A. Rafiei, and M. Jeddi-Tehrani, *Nucleolin; A tumor associated antigen as a potential lung cancer biomarker.* Pathology - Research and Practice, 2022. **240**: p. 154160.
41. Goldshmit, Y., et al., *Interfering with the interaction between ErbB1, nucleolin and Ras as a potential treatment for glioblastoma.* Oncotarget, 2014. **5**(18): p. 8602.
42. Qi, J., et al., *Multidrug delivery systems based on human serum albumin for combination therapy with three anticancer agents.* Molecular pharmaceutics, 2016. **13**(9): p. 3098-3105.
43. Jabir, N.R., et al., *Nanotechnology-based approaches in anticancer research.* International journal of nanomedicine, 2012. **7**: p. 4391.
44. Alshaer, W., H. Hillaireau, and E. Fattal, *Aptamer-guided nanomedicines for anticancer drug delivery.* Advanced drug delivery reviews, 2018. **134**: p. 122-137.
45. Tekie, F.S.M., et al., *Glutathione responsive chitosan-thiolated dextran conjugated miR-145 nanoparticles targeted with AS1411 aptamer for cancer treatment.* Carbohydrate polymers, 2018. **201**: p. 131-140.
46. Zhang, R., et al., *Co-delivery of doxorubicin and AS1411 aptamer by poly (ethylene glycol)-poly (β-amino esters) polymeric micelles for targeted cancer therapy.* Journal of Nanoparticle Research, 2017. **19**(6): p. 1-13.
47. Aravind, A., et al., *AS1411 aptamer tagged PLGA-lecithin-PEG nanoparticles for tumor cell targeting and drug delivery.* Biotechnology and bioengineering, 2012. **109**(11): p. 2920-2931.
48. Alibolandi, M., et al., *AS1411 aptamer-decorated biodegradable polyethylene glycol–poly (lactic-co-glycolic acid) nanopolymersomes for the targeted delivery*

of gemcitabine to non–small cell lung cancer in vitro. Journal of pharmaceutical sciences, 2016. **105**(5): p. 1741-1750.

49. Saravanakumar, K., et al., *Enhanced cancer therapy with pH-dependent and aptamer functionalized doxorubicin loaded polymeric (poly D, L-lactic-co-glycolic acid) nanoparticles.* Archives of biochemistry and biophysics, 2019. **671**: p. 143-151.
50. Chen, H., et al., *Dual aptamer modified dendrigraft poly-l-lysine nanoparticles for overcoming multi-drug resistance through mitochondrial targeting.* Journal of Materials Chemistry B, 2017. **5**(5): p. 972-979.
51. Alibolandi, M., et al., *Smart AS1411-aptamer conjugated pegylated PAMAM dendrimer for the superior delivery of camptothecin to colon adenocarcinoma in vitro and in vivo.* International journal of pharmaceutics, 2017. **519**(1-2): p. 352-364.
52. Malik, M.T., et al., *AS1411-conjugated gold nanospheres and their potential for breast cancer therapy.* Oncotarget, 2015. **6**(26): p. 22270.
53. Laber, D.A., et al., *Extended phase I study of AS1411 in renal and non-small cell lung cancers.* Journal of Clinical Oncology, 2006. **24**(18_suppl): p. 13098-13098.
54. Rosenberg, J.E., et al., *A phase II trial of AS1411 (a novel nucleolin-targeted DNA aptamer) in metastatic renal cell carcinoma.* Invest New Drugs, 2014. **32**(1): p. 178-87.
55. Lee, R.C., R.L. Feinbaum, and V. Ambros, *The C. elegans heterochronic gene lin-4 encodes small RNAs with antisense complementarity to lin-14.* cell, 1993. **75**(5): p. 843-854.
56. Peng, Y. and C.M. Croce, *The role of MicroRNAs in human cancer.* Signal Transduction and Targeted Therapy, 2016. **1**(1): p. 15004.
57. Fire, A., et al., *Potent and specific genetic interference by double-stranded RNA in Caenorhabditis elegans.* nature, 1998. **391**(6669): p. 806-811.
58. MacFarlane, L.-A. and P. R Murphy, *MicroRNA: biogenesis, function and role in cancer.* Current genomics, 2010. **11**(7): p. 537-561.
59. Mishra, S., T. Yadav, and V. Rani, *Exploring miRNA based approaches in cancer diagnostics and therapeutics.* Critical reviews in oncology/hematology, 2016. **98**: p. 12-23.
60. O'Donnell, K.A., et al., *c-Myc-regulated microRNAs modulate E2F1 expression.* nature, 2005. **435**(7043): p. 839-843.
61. He, L., et al., *A microRNA component of the p53 tumour suppressor network.* Nature, 2007. **447**(7148): p. 1130-1134.
62. Cencioni, C., et al., *The “Superoncogene” Myc at the Crossroad between Metabolism and Gene Expression in Glioblastoma Multiforme.* International Journal of Molecular Sciences, 2023. **24**(4): p. 4217.
63. Wang, B., et al., *Reciprocal regulation of microRNA-122 and c-Myc in hepatocellular cancer: role of E2F1 and transcription factor dimerization partner 2.* Hepatology, 2014. **59**(2): p. 555-566.
64. Han, H., et al., *A c-Myc-MicroRNA functional feedback loop affects hepatocarcinogenesis.* Hepatology, 2013. **57**(6): p. 2378-2389.

65. Tao, J., X. Zhao, and J. Tao, *c-MYC-miRNA circuitry: a central regulator of aggressive B-cell malignancies.* Cell Cycle, 2014. **13**(2): p. 191-8.
66. Mafi, A., et al., *Recent insights into the microRNA-dependent modulation of gliomas from pathogenesis to diagnosis and treatment.* Cellular & Molecular Biology Letters, 2022. **27**(1): p. 65.
67. Bautista-Sánchez, D., et al., *The Promising Role of miR-21 as a Cancer Biomarker and Its Importance in RNA-Based Therapeutics.* Molecular Therapy - Nucleic Acids, 2020. **20**: p. 409-420.
68. Zhang, L., Y. Liao, and L. Tang, *MicroRNA-34 family: a potential tumor suppressor and therapeutic candidate in cancer.* Journal of Experimental & Clinical Cancer Research, 2019. **38**(1): p. 53.
69. Zhu, S., et al., *Restoration of microRNA function impairs MYC-dependent maintenance of MLL leukemia.* Leukemia, 2020. **34**(9): p. 2484-2488.
70. Liu, Y., et al., *The Jun/miR-22/HuR regulatory axis contributes to tumourigenesis in colorectal cancer.* Molecular Cancer, 2018. **17**(1): p. 1-15.
71. Sharma, S., et al., *Enhanced efficacy of anti-miR-191 delivery through stearylamine liposome formulation for the treatment of breast cancer cells.* International Journal of Pharmaceutics, 2017. **530**(1): p. 387-400.
72. Reschke, C.R., et al., *Systemic delivery of antagomirs during blood-brain barrier disruption is disease-modifying in experimental epilepsy.* Molecular Therapy, 2021. **29**(6): p. 2041-2052.
73. Wu, L., et al., *Delivery of therapeutic oligonucleotides in nanoscale.* Bioactive Materials, 2022. **7**: p. 292-323.
74. Ochoa, S. and V.T. Milam, *Modified Nucleic Acids: Expanding the Capabilities of Functional Oligonucleotides.* Molecules, 2020. **25**(20).
75. Eble, J.A. and S. Niland, *The extracellular matrix in tumor progression and metastasis.* Clinical & experimental metastasis, 2019. **36**(3): p. 171-198.
76. Jones, C.H., et al., *Overcoming nonviral gene delivery barriers: perspective and future.* Molecular pharmaceutics, 2013. **10**(11): p. 4082-4098.
77. Loh, X.J., et al., *Utilising inorganic nanocarriers for gene delivery.* Biomaterials science, 2016. **4**(1): p. 70-86.
78. Pakunlu, R.I., et al., *In vitro and in vivo intracellular liposomal delivery of antisense oligonucleotides and anticancer drug.* Journal of controlled release, 2006. **114**(2): p. 153-162.
79. Love, J.C., et al., *Self-assembled monolayers of thiolates on metals as a form of nanotechnology.* Chemical reviews, 2005. **105**(4): p. 1103-1170.
80. Rosi, N.L., et al., *Oligonucleotide-modified gold nanoparticles for intracellular gene regulation.* Science, 2006. **312**(5776): p. 1027-1030.
81. Q, A., *Understanding the UV-Vis Spectroscopy for Nanoparticles.* 2019.
82. Carvalho, P.M., et al., *Application of Light Scattering Techniques to Nanoparticle Characterization and Development.* Frontiers in Chemistry, 2018. **6**.
83. Haiss, W., et al., *Determination of size and concentration of gold nanoparticles from UV− Vis spectra.* Analytical chemistry, 2007. **79**(11): p. 4215-4221.

84. Clogston, J.D. and A.K. Patri, *Zeta Potential Measurement*, in *Characterization of Nanoparticles Intended for Drug Delivery*, S.E. McNeil, Editor. 2011, Humana Press: Totowa, NJ. p. 63-70.
85. Danaei, M., et al., *Impact of Particle Size and Polydispersity Index on the Clinical Applications of Lipidic Nanocarrier Systems.* Pharmaceutics, 2018. **10**(2).
86. Yokoyama, T., *Chapter 1 - Basic Properties and Measuring Methods of Nanoparticles*, in *Nanoparticle Technology Handbook (Third Edition)*, M. Naito, et al., Editors. 2018, Elsevier. p. 3-47.
87. Hurst, S.J., A.K. Lytton-Jean, and C.A. Mirkin, *Maximizing DNA loading on a range of gold nanoparticle sizes.* Anal Chem, 2006. **78**(24): p. 8313-8.
88. Sun, R., et al., *The tumor EPR effect for cancer drug delivery: Current status, limitations, and alternatives.* Advanced Drug Delivery Reviews, 2022. **191**: p. 114614.
89. Maeda, H., et al., *Tumor vascular permeability and the EPR effect in macromolecular therapeutics: a review.* Journal of controlled release, 2000. **65**(1-2): p. 271-284.
90. Barenholz, Y.C., *Doxil®—The first FDA-approved nano-drug: Lessons learned.* Journal of controlled release, 2012. **160**(2): p. 117-134.
91. Balça-Silva, J., et al., *Nucleolin is expressed in patient-derived samples and glioblastoma cells, enabling improved intracellular drug delivery and cytotoxicity.* Exp Cell Res, 2018. **370**(1): p. 68-77.
92. Farin, K., et al., *Oncogenic synergism between ErbB1, nucleolin, and mutant Ras.* Cancer research, 2011. **71**(6): p. 2140-2151.
93. Reyes-Reyes, E.M., et al., *Mechanistic studies of anticancer aptamer AS1411 reveal a novel role for nucleolin in regulating Rac1 activation.* Molecular Oncology, 2015. **9**(7): p. 1392-1405.
94. Bates, P.J., et al., *G-quadruplex oligonucleotide AS1411 as a cancer-targeting agent: Uses and mechanisms.* Biochimica et Biophysica Acta (BBA) - General Subjects, 2017. **1861**(5, Part B): p. 1414-1428.
95. Sathiyaseelan, A., et al., *pH-controlled nucleolin targeted release of dual drug from chitosan-gold based aptamer functionalized nano drug delivery system for improved glioblastoma treatment.* Carbohydrate Polymers, 2021. **262**: p. 117907.
96. Wuchty, S., et al., *Prediction of associations between microRNAs and gene expression in glioma biology.* PloS one, 2011. **6**(2): p. e14681.
97. Kefas, B., et al., *microRNA-7 inhibits the epidermal growth factor receptor and the Akt pathway and is down-regulated in glioblastoma.* Cancer research, 2008. **68**(10): p. 3566-3572.
98. Li, Y., et al., *MicroRNA-34a inhibits glioblastoma growth by targeting multiple oncogenes.* Cancer research, 2009. **69**(19): p. 7569-7576.
99. Yin, D., et al., *miR-34a functions as a tumor suppressor modulating EGFR in glioblastoma multiforme.* Oncogene, 2013. **32**(9): p. 1155-1163.

100. Skalsky, R.L. and B.R. Cullen, *Reduced expression of brain-enriched microRNAs in glioblastomas permits targeted regulation of a cell death gene.* PloS one, 2011. **6**(9): p. e24248.
101. Godlewski, J., et al., *Targeting of the Bmi-1 oncogene/stem cell renewal factor by microRNA-128 inhibits glioma proliferation and self-renewal.* Cancer research, 2008. **68**(22): p. 9125-9130.
102. Chan, J.A., A.M. Krichevsky, and K.S. Kosik, *MicroRNA-21 is an antiapoptotic factor in human glioblastoma cells.* Cancer research, 2005. **65**(14): p. 6029-6033.
103. Corsten, M.F., et al., *MicroRNA-21 knockdown disrupts glioma growth in vivo and displays synergistic cytotoxicity with neural precursor cell–delivered S-TRAIL in human gliomas.* Cancer research, 2007. **67**(19): p. 8994-9000.
104. Gabriely, G., et al., *MicroRNA 21 promotes glioma invasion by targeting matrix metalloproteinase regulators.* Molecular and cellular biology, 2008. **28**(17): p. 5369-5380.
105. Papagiannakopoulos, T., A. Shapiro, and K.S. Kosik, *MicroRNA-21 targets a network of key tumor-suppressive pathways in glioblastoma cells.* Cancer research, 2008. **68**(19): p. 8164-8172.
106. Shi, L., et al., *MiR-21 protected human glioblastoma U87MG cells from chemotherapeutic drug temozolomide induced apoptosis by decreasing Bax/Bcl-2 ratio and caspase-3 activity.* Brain research, 2010. **1352**: p. 255-264.
107. Rao, S.A., V. Santosh, and K. Somasundaram, *Genome-wide expression profiling identifies deregulated miRNAs in malignant astrocytoma.* Modern Pathology, 2010. **23**(10): p. 1404-1417.
108. Huang, T., et al., *MIR93 (microRNA-93) regulates tumorigenicity and therapy response of glioblastoma by targeting autophagy.* Autophagy, 2019. **15**(6): p. 1100-1111.
109. Kim, J.K., et al., *Molecular imaging of a cancer-targeting theragnostics probe using a nucleolin aptamer- and microRNA-221 molecular beacon-conjugated nanoparticle.* Biomaterials, 2012. **33**(1): p. 207-217.
110. Chen, D., et al., *Dual targeting luminescent gold nanoclusters for tumor imaging and deep tissue therapy.* Biomaterials, 2016. **100**: p. 1-16.
111. Luo, Z., et al., *Precise glioblastoma targeting by AS1411 aptamer-functionalized poly (l-γ-glutamylglutamine)–paclitaxel nanoconjugates.* Journal of Colloid and Interface Science, 2017. **490**: p. 783-796.
112. Zhu, X., et al., *Transferrin/aptamer conjugated mesoporous ruthenium nanosystem for redox-controlled and targeted chemo-photodynamic therapy of glioma.* Acta Biomaterialia, 2018. **82**: p. 143-157.
113. Mosafer, J., et al., *Study and evaluation of nucleolin-targeted delivery of magnetic PLGA-PEG nanospheres loaded with doxorubicin to C6 glioma cells compared with low nucleolin-expressing L929 cells.* Materials Science and Engineering: C, 2017. **72**: p. 123-133.
114. Chen, H., et al., *Aptamer modification improves the adenoviral transduction of malignant glioma cells.* Journal of Biotechnology, 2013. **168**(4): p. 362-366.

115. Schmittgen, T.D., et al., *A high-throughput method to monitor the expression of microRNA precursors.* Nucleic Acids Res, 2004. **32**(4): p. e43.
116. Volinia, S., et al., *A microRNA expression signature of human solid tumors defines cancer gene targets.* Proceedings of the National Academy of Sciences, 2006. **103**(7): p. 2257-2261.
117. Zhu, S., et al., *MicroRNA-21 targets tumor suppressor genes in invasion and metastasis.* Cell Research, 2008. **18**(3): p. 350-359.
118. Fujita, S., et al., *miR-21 Gene expression triggered by AP-1 is sustained through a double-negative feedback mechanism.* Journal of molecular biology, 2008. **378**(3): p. 492-504.
119. Asangani, I.A., et al., *MicroRNA-21 (miR-21) post-transcriptionally downregulates tumor suppressor Pdcd4 and stimulates invasion, intravasation and metastasis in colorectal cancer.* Oncogene, 2008. **27**(15): p. 2128-2136.
120. Kutay, H., et al., *Downregulation of miR-122 in the rodent and human hepatocellular carcinomas.* Journal of cellular biochemistry, 2006. **99**(3): p. 671-678.
121. Zhu, S., et al., *MicroRNA-21 Targets the Tumor Suppressor Gene Tropomyosin 1 (TPM1)*.* Journal of Biological Chemistry, 2007. **282**(19): p. 14328-14336.
122. Frankel, L.B., et al., *Programmed cell death 4 (PDCD4) is an important functional target of the microRNA miR-21 in breast cancer cells.* Journal of Biological Chemistry, 2008. **283**(2): p. 1026-1033.
123. Sayed, D., et al., *MicroRNA-21 targets Sprouty2 and promotes cellular outgrowths.* Molecular biology of the cell, 2008. **19**(8): p. 3272-3282.
124. Pfeffer, S.R., C.H. Yang, and L.M. Pfeffer, *The role of miR-21 in cancer.* Drug development research, 2015. **76**(6): p. 270-277.
125. Lee, T.J., et al., *RNA Nanoparticle-Based Targeted Therapy for Glioblastoma through Inhibition of Oncogenic miR-21.* Molecular Therapy, 2017. **25**(7): p. 1544-1555.
126. Yin, H., et al., *Delivery of Anti-miRNA for Triple-Negative Breast Cancer Therapy Using RNA Nanoparticles Targeting Stem Cell Marker CD133.* Molecular Therapy, 2019. **27**(7): p. 1252-1261.
127. Nieland, L., et al., *CRISPR-Cas knockout of miR21 reduces glioma growth.* Molecular Therapy - Oncolytics, 2022. **25**: p. 121-136.
128. Bian, Z., et al., *Noncoding RNAs involved in the STAT3 pathway in glioma.* Cancer Cell International, 2021. **21**: p. 1-15.
129. Aloizou, A.-M., et al., *The role of MiRNA-21 in gliomas: Hope for a novel therapeutic intervention?* Toxicology Reports, 2020. **7**: p. 1514-1530.
130. Knauer, N., et al., *49P Antitumor effects of cationic dendritic molecules and their complexes with microRNA in glioblastoma stem-like cells.* Annals of Oncology, 2022. **33**: p. S21-S22.
131. Cao, H., X. Zhou, and Y. Zeng, *Microfluidic exponential rolling circle amplification for sensitive microRNA detection directly from biological samples.* Sensors and Actuators B: Chemical, 2019. **279**: p. 447-457.

132. Hu, X., et al., *Multifunctional Gold Nanoparticles: A Novel Nanomaterial for Various Medical Applications and Biological Activities.* Frontiers in Bioengineering and Biotechnology, 2020. **8**.
133. Faulk, W.P. and G.M. Taylor, *Communication to the editors: an immunocolloid method for the electron microscope.* Immunochemistry, 1971. **8**(11): p. 1081-1083.
134. Dykman, L.A. and N.G. Khlebtsov, *Gold nanoparticles in biology and medicine: recent advances and prospects.* Acta Naturae, 2011. **3**(2): p. 34-55.
135. Haiss, W., et al., *Determination of size and concentration of gold nanoparticles from UV-vis spectra.* Anal Chem, 2007. **79**(11): p. 4215-21.
136. Ding, Y., et al., *Gold Nanoparticles for Nucleic Acid Delivery.* Molecular Therapy, 2014. **22**(6): p. 1075-1083.
137. Rizvi, S.A.A. and A.M. Saleh, *Applications of nanoparticle systems in drug delivery technology.* Saudi Pharm J, 2018. **26**(1): p. 64-70.
138. QT., O., *CBTRUS Statistical Report: Primary Brain and Central Nervous System Tumors Diagnosed in the United States in 2008-2012. .* Neuro. Oncol. , 2015.
139. Roca, M. and A.J. Haes, *Probing cells with noble metal nanoparticle aggregates.* Nanomedicine, 2008. **3**(4): p. 555-565.
140. DeLong, R.K., et al., *Functionalized gold nanoparticles for the binding, stabilization, and delivery of therapeutic DNA, RNA, and other biological macromolecules.* Nanotechnol Sci Appl, 2010. **3**: p. 53-63.
141. Sperling, R.A., et al., *Electrophoretic separation of nanoparticles with a discrete number of functional groups.* Advanced Functional Materials, 2006. **16**(7): p. 943-948.
142. Aslan, K., C.C. Luhrs, and V.H. Perez-Luna, *Controlled and reversible aggregation of biotinylated gold nanoparticles with streptavidin.* Journal of Physical Chemistry B, 2004. **108**(40): p. 15631-15639.
143. Brennan, J.L., et al., *Bionanoconjugation via click chemistry: The creation of functional hybrids of lipases and gold nanoparticles.* Bioconjug Chem, 2006. **17**(6): p. 1373-5.
144. Gole, A. and C.J. Murphy, *Azide-derivatized gold nanorods: functional materials for "click" chemistry.* Langmuir, 2008. **24**(1): p. 266-72.
145. Carnovale, C., et al., *Identifying trends in gold nanoparticle toxicity and uptake: size, shape, capping ligand, and biological corona.* ACS omega, 2019. **4**(1): p. 242-256.
146. Behzadi, S., et al., *Cellular uptake of nanoparticles: journey inside the cell.* Chemical Society Reviews, 2017. **46**(14): p. 4218-4244.
147. Pudlarz, A. and J. Szemraj, *Nanoparticles as carriers of proteins, peptides and other therapeutic molecules.* Open life sciences, 2018. **13**(1): p. 285-298.
148. Medici, S., et al., *Gold nanoparticles and cancer: Detection, diagnosis and therapy.* Seminars in Cancer Biology, 2021. **76**: p. 27-37.
149. Wang, Z., et al., *Gold nanoparticle‑mediated delivery of paclitaxel and nucleic acids for cancer therapy.* Molecular Medicine Reports, 2020. **22**(6): p. 4475-4484.

150. Thambiraj, S., et al., *Evaluation of cytotoxic activity of docetaxel loaded gold nanoparticles for lung cancer drug delivery.* Cancer Treatment and Research Communications, 2019. **21**: p. 100157.
151. Ahn, J., et al., *Coassembled Nanoparticles Composed of Functionalized Mesoporous Silica and Pillar [5] arene-Appended Gold Nanoparticles as Mitochondrial-Selective Dual-Drug Carriers.* Particle & Particle Systems Characterization, 2020. **37**(9): p. 2000136.
152. Nie, L., et al., *Synthesis of aptamer-PEI-g-PEG modified gold nanoparticles loaded with doxorubicin for targeted drug delivery.* JoVE (Journal of Visualized Experiments), 2020(160): p. e61139.
153. Liu, Z., et al., *Development of a multifunctional gold nanoplatform for combined chemo-photothermal therapy against oral cancer.* Nanomedicine, 2020. **15**(07): p. 661-676.
154. Kabirian-Dehkordi, S., et al., *AS1411-conjugated gold nanoparticles affect cell proliferation through a mechanism that seems independent of nucleolin.* Nanomedicine: Nanotechnology, Biology and Medicine, 2019. **21**: p. 102060.
155. Baneshi, M., et al., *A novel theranostic system of AS1411 aptamer-functionalized albumin nanoparticles loaded on iron oxide and gold nanoparticles for doxorubicin delivery.* International Journal of Pharmaceutics, 2019. **564**: p. 145-152.
156. Ai, J., et al., *Multifunctional AS1411-functionalized fluorescent gold nanoparticles for targeted cancer cell imaging and efficient photodynamic therapy.* Talanta, 2014. **118**: p. 54-60.
157. Shafiei, F., R.S. Saberi, and M.A. Mehrgardi, *A label-free electrochemical aptasensor for breast cancer cell detection based on a reduced graphene oxide-chitosan-gold nanoparticle composite.* Bioelectrochemistry, 2021. **140**: p. 107807.
158. Ruttala, H.B., et al., *Multi-responsive albumin-lonidamine conjugated hybridized gold nanoparticle as a combined photothermal-chemotherapy for synergistic tumor ablation.* Acta Biomaterialia, 2020. **101**: p. 531-543.
159. Hong, E.J., et al., *Cancer-targeted photothermal therapy using aptamer-conjugated gold nanoparticles.* Journal of Industrial and Engineering Chemistry, 2018. **67**: p. 429-436.
160. Borghei, Y.-S., et al., *Visual detection of cancer cells by colorimetric aptasensor based on aggregation of gold nanoparticles induced by DNA hybridization.* Analytica Chimica Acta, 2016. **904**: p. 92-97.
161. Gallina, M.E., et al., *Aptamer-conjugated, fluorescent gold nanorods as potential cancer theradiagnostic agents.* Materials Science and Engineering: C, 2016. **59**: p. 324-332.
162. Motaghi, H., et al., *Electrochemiluminescence detection of human breast cancer cells using aptamer modified bipolar electrode mounted into 3D printed microchannel.* Biosensors and Bioelectronics, 2018. **118**: p. 217-223.
163. Dam, D.H., et al., *Biodistribution and in vivo toxicity of aptamer-loaded gold nanostars.* Nanomedicine, 2015. **11**(3): p. 671-9.

164. Zhang, Y., et al., *Laser-triggered collaborative chemophotothermal effect of gold nanoparticles for targeted colon cancer therapy.* Biomedicine & Pharmacotherapy, 2020. **130**: p. 110492.
165. Khademi, Z., et al., *Co-delivery of doxorubicin and aptamer against Forkhead box M1 using chitosan-gold nanoparticles coated with nucleolin aptamer for synergistic treatment of cancer cells.* Carbohydr Polym, 2020. **248**: p. 116735.
166. Saravanakumar, K., et al., *Nucleolin targeted delivery of aptamer tagged Trichoderma derived crude protein coated gold nanoparticles for improved cytotoxicity in cancer cells.* Process Biochemistry, 2021. **102**: p. 325-332.
167. Yu, A.Y.-H., et al., *Epidermal growth factor receptors siRNA-conjugated collagen modified gold nanoparticles for targeted imaging and therapy of lung cancer.* Materials Today Advances, 2021. **12**: p. 100191.
168. Deng, R., et al., *Targeting epigenetic pathway with gold nanoparticles for acute myeloid leukemia therapy.* Biomaterials, 2018. **167**: p. 80-90.
169. Taghdisi, S.M., et al., *Double targeting, controlled release and reversible delivery of daunorubicin to cancer cells by polyvalent aptamers-modified gold nanoparticles.* Materials Science and Engineering: C, 2016. **61**: p. 753-761.
170. Dam, D.H.M., R.C. Lee, and T.W. Odom, *Improved in Vitro Efficacy of Gold Nanoconstructs by Increased Loading of G-quadruplex Aptamer.* Nano Letters, 2014. **14**(5): p. 2843-2848.
171. Su, X., et al., *One-pot synthesized AuNPs/MoS2/rGO nanocomposite as sensitive electrochemical aptasensing platform for nucleolin detection.* Journal of Electroanalytical Chemistry, 2020. **859**: p. 113868.
172. Kim, J.-H., et al., *Effective delivery of anti-miRNA DNA oligonucleotides by functionalized gold nanoparticles.* Journal of Biotechnology, 2011. **155**(3): p. 287-292.
173. Jensen, S.A., et al., *Spherical Nucleic Acid Nanoparticle Conjugates as an RNAi-Based Therapy for Glioblastoma.* Science Translational Medicine, 2013. **5**(209): p. 209ra152-209ra152.
174. Cutler, J.I., E. Auyeung, and C.A. Mirkin, *Spherical Nucleic Acids.* Journal of the American Chemical Society, 2012. **134**(3): p. 1376-1391.
175. Rosi, N.L., et al., *Oligonucleotide-Modified Gold Nanoparticles for Intracellular Gene Regulation.* Science, 2006. **312**(5776): p. 1027-1030.
176. Lin, J., et al., *PEGylation on mixed monolayer gold nanoparticles: Effect of grafting density, chain length, and surface curvature.* Journal of Colloid and Interface Science, 2017. **504**: p. 325-333.
177. Masitas, R.A. and F.P. Zamborini, *Oxidation of Highly Unstable <4 nm Diameter Gold Nanoparticles 850 mV Negative of the Bulk Oxidation Potential.* Journal of the American Chemical Society, 2012. **134**(11): p. 5014-5017.
178. Jana, N.R., L. Gearheart, and C.J. Murphy, *Wet Chemical Synthesis of High Aspect Ratio Cylindrical Gold Nanorods.* The Journal of Physical Chemistry B, 2001. **105**(19): p. 4065-4067.
179. Schmittgen, T.D., et al., *Real-time PCR quantification of precursor and mature microRNA.* Methods, 2008. **44**(1): p. 31-38.

180. Roa, W., et al., *Identification of a new microRNA expression profile as a potential cancer screening tool.* Clinical and Investigative Medicine, 2010: p. E124-E132.
181. Reyes-Reyes, E.M., Y. Teng, and P.J. Bates, *A new paradigm for aptamer therapeutic AS1411 action: uptake by macropinocytosis and its stimulation by a nucleolin-dependent mechanism.* Cancer Res, 2010. **70**(21): p. 8617-29.
182. Zhao, N., et al., *An ultra pH-sensitive and aptamer-equipped nanoscale drug-delivery system for selective killing of tumor cells.* Small, 2013. **9**(20): p. 3477-84.
183. Stupp, R., et al., *Radiotherapy plus concomitant and adjuvant temozolomide for glioblastoma.* N Engl J Med, 2005. **352**(10): p. 987-96.
184. Hong, E.J., et al., *Cancer-targeted photothermal therapy using aptamer-conjugated gold nanoparticles.* Journal of Industrial and Engineering Chemistry, 2018.
185. Abnous, K., et al., *A novel chemotherapy drug-free delivery system composed of three therapeutic aptamers for the treatment of prostate and breast cancers in vitro and in vivo.* Nanomedicine: Nanotechnology, Biology and Medicine, 2017. **13**(6): p. 1933-1940.
186. Brann, T., et al., *Gold Nanoplates as Cancer-Targeted Photothermal Actuators for Drug Delivery and Triggered Release.* Journal of Nanomaterials, 2016. **2016**: p. 2036029.
187. Chauhan, R., et al., *Targeted Gold Nanoparticle–Oligonucleotide Contrast Agents in Combination with a New Local Voxel-Wise MRI Analysis Algorithm for In Vitro Imaging of Triple-Negative Breast Cancer.* Nanomaterials, 2019. **9**(5): p. 709.
188. Wang, W., et al., *Zeta-potential data reliability of gold nanoparticle biomolecular conjugates and its application in sensitive quantification of surface absorbed protein.* Colloids and Surfaces B: Biointerfaces, 2016. **148**: p. 541-548.
189. Stolarczyk, E.U., et al., *Pemetrexed conjugated with gold nanoparticles - Synthesis, characterization and a study of noncovalent interactions.* Eur J Pharm Sci, 2017. **109**: p. 13-20.
190. Subramaniam, V.D., et al., *Comparative study on anti-proliferative potentials of zinc oxide and aluminium oxide nanoparticles in colon cancer cells.* Acta Biomed, 2019. **90**(2): p. 241-247.
191. Jazayeri, M.H., et al., *Various methods of gold nanoparticles (GNPs) conjugation to antibodies.* Sensing and Bio-Sensing Research, 2016. **9**: p. 17-22.
192. Tsai, S.-W., et al., *Internalized Gold Nanoparticles Do Not Affect the Osteogenesis and Apoptosis of MG63 Osteoblast-Like Cells: A Quantitative, In Vitro Study.* PLOS ONE, 2013. **8**(10): p. e76545.
193. Madhusudanan, P., et al., *Effect of gold nanoparticle treated dorsal root ganglion cells on peripheral neurite differentiation.* Toxicology in Vitro, 2021. **74**: p. 105175.
194. Kharazian, B., et al., *Bare surface of gold nanoparticle induces inflammation through unfolding of plasma fibrinogen.* Scientific Reports, 2018. **8**(1): p. 12557.
195. Kitambi, S.S., et al., *RETRACTED: Vulnerability of glioblastoma cells to catastrophic vacuolization and death induced by a small molecule*. 2014, Elsevier.

196. Li, C., et al., *Nerve growth factor activation of the TrkA receptor induces cell death, by macropinocytosis, in medulloblastoma Daoy cells.* Journal of neurochemistry, 2010. **112**(4): p. 882-899.
197. Cheng, Y., et al., *AS1411-Induced Growth Inhibition of Glioma Cells by Up-Regulation of p53 and Down-Regulation of Bcl-2 and Akt1 via Nucleolin.* PLoS One, 2016. **11**(12): p. e0167094.
198. Khademi, Z., et al., *A novel dual-targeting delivery system for specific delivery of CRISPR/Cas9 using hyaluronic acid, chitosan and AS1411.* Carbohydrate Polymers, 2022. **292**: p. 119691.
199. Calin, G.A., et al., *MicroRNA profiling reveals distinct signatures in B cell chronic lymphocytic leukemias.* Proceedings of the National Academy of Sciences, 2004. **101**(32): p. 11755-11760.
200. Krichevsky, A.M. and G. Gabriely, *miR-21: a small multi-faceted RNA.* Journal of Cellular and Molecular Medicine, 2009. **13**(1): p. 39-53.
201. D'Abramo, M., et al., *On the Nature of DNA Hyperchromic Effect.* The Journal of Physical Chemistry B, 2013. **117**(29): p. 8697-8704.
202. Chintala, S.K., J.C. Tonn, and J.S. Rao, *Matrix metalloproteinases and their biological function in human gliomas.* International Journal of Developmental Neuroscience, 1999. **17**(5-6): p. 495-502.
203. Belkourchia, F. and R.R. Desrosiers, *The enzyme L-isoaspartyl (D-aspartyl) methyltransferase promotes migration and invasion in human U-87 MG and U-251 MG glioblastoma cell lines.* Biomedicine & Pharmacotherapy, 2021. **140**: p. 111766.
204. Jansen, A.P., et al., *Characterization of programmed cell death 4 in multiple human cancers reveals a novel enhancer of drug sensitivity.* Molecular Cancer Therapeutics, 2004. **3**(2): p. 103-110.
205. Selcuklu, S.D., Mark T.A. Donoghue, and C. Spillane, *miR-21 as a key regulator of oncogenic processes.* Biochemical Society Transactions, 2009. **37**(4): p. 918-925.
206. Ren, Y., et al., *MicroRNA-21 inhibitor sensitizes human glioblastoma cells U251 (PTEN-mutant) and LN229 (PTEN-wild type) to taxol.* BMC cancer, 2010. **10**: p. 1-13.
207. Jiang, L.-H., et al., *miR-21 regulates tumor progression through the miR-21-PDCD4-Stat3 pathway in human salivary adenoid cystic carcinoma.* Laboratory Investigation, 2015. **95**(12): p. 1398-1408.
208. Lai, C.-Y., et al., *MicroRNA-21 Plays Multiple Oncometabolic Roles in Colitis-Associated Carcinoma and Colorectal Cancer via the PI3K/AKT, STAT3, and PDCD4/TNF-α Signaling Pathways in Zebrafish.* Cancers, 2021. **13**(21): p. 5565.
209. Pichiorri, F., et al., *In vivo NCL targeting affects breast cancer aggressiveness through miRNA regulation.* Journal of Experimental Medicine, 2013. **210**(5): p. 951-968.
210. Huszthy, P.C., et al., *In vivo models of primary brain tumors: pitfalls and perspectives.* Neuro Oncol, 2012. **14**(8): p. 979-93.
211. Mahesparan, R., et al., *Expression of extracellular matrix components in a highly infiltrative in vivo glioma model.* Acta Neuropathol, 2003. **105**(1): p. 49-57.

212. Jin, K., et al., *Patient-derived human tumour tissue xenografts in immunodeficient mice: a systematic review.* Clinical and Translational Oncology, 2010. **12**(7): p. 473-480.
213. Taillandier, L., L. Antunes, and K.S. Angioi-Duprez, *Models for neuro-oncological preclinical studies: solid orthotopic and heterotopic grafts of human gliomas into nude mice.* J Neurosci Methods, 2003. **125**(1-2): p. 147-57.
214. Li, X., et al., *Surface chemistry governs the sub-organ transfer, clearance and toxicity of functional gold nanoparticles in the liver and kidney.* J Nanobiotechnology, 2020. **18**(1): p. 45.
215. Sanchez Gil, J., et al., *Nanobody-based retargeting of an oncolytic herpesvirus for eliminating CXCR4+ GBM cells: A proof of principle.* Molecular Therapy - Oncolytics, 2022. **26**: p. 35-48.
216. Liu, F., et al., *Rapid tumor recurrence in a novel murine GBM surgical model is associated with Akt/PD-L1/vimentin signaling.* Biochemical and Biophysical Research Communications, 2021. **569**: p. 1-9.
217. Patrizii, M., et al., *Utility of Glioblastoma Patient-Derived Orthotopic Xenografts in Drug Discovery and Personalized Therapy.* Front Oncol, 2018. **8**: p. 23.
218. Chiarelli, P.A., et al., *Iron oxide nanoparticle-mediated radiation delivery for glioblastoma treatment.* Materials Today, 2022. **56**: p. 66-78.
219. Ye, Z., et al., *Esterase-responsive and size-optimized prodrug nanoparticles for effective intracranial drug delivery and glioblastoma treatment.* Nanomedicine: Nanotechnology, Biology and Medicine, 2022. **44**: p. 102581.
220. Wang, H., et al., *A Magnetic T7 Peptide&AS1411 Aptamer-Modified Microemulsion for Triple Glioma-Targeted Delivery of Shikonin and Docetaxel.* Journal of Pharmaceutical Sciences, 2021. **110**(8): p. 2946-2954.
221. Tsang, A.W., et al., *Altered membrane trafficking in activated bone marrow-derived macrophages.* Journal of Leukocyte Biology, 2000. **68**(4): p. 487-494.
222. Noireaux, J., et al., *Gold Nanoparticle Uptake in Tumor Cells: Quantification and Size Distribution by sp-ICPMS.* Separations, 2019. **6**(1): p. 3.
223. Gunduz, N., et al., *Intracellular Accumulation of Gold Nanoparticles Leads to Inhibition of Macropinocytosis to Reduce the Endoplasmic Reticulum Stress.* Sci Rep, 2017. **7**: p. 40493.
224. Dröse, S. and K. Altendorf, *Bafilomycins and concanamycins as inhibitors of V-ATPases and P-ATPases.* Journal of Experimental Biology, 1997. **200**(1): p. 1-8.
225. Maltese, W.A. and J.H. Overmeyer, *Methuosis: Nonapoptotic Cell Death Associated with Vacuolization of Macropinosome and Endosome Compartments.* The American Journal of Pathology, 2014. **184**(6): p. 1630-1642.
226. Mischel, P.S., T.F. Cloughesy, and S.F. Nelson, *DNA-microarray analysis of brain cancer: molecular classification for therapy.* Nature Reviews Neuroscience, 2004. **5**(10): p. 782-792.
227. Aljohani, M.M., et al., *Aptamers: Potential Diagnostic and Therapeutic Agents for Blood Diseases.* Molecules, 2022. **27**(2).
228. Marasca, R. and R. Maffei, *NOX-A12: mobilizing CLL away from home.* Blood, The Journal of the American Society of Hematology, 2014. **123**(7): p. 952-953.

229. Paerl, H.W., *Coastal eutrophication and harmful algal blooms: Importance of atmospheric deposition and groundwater as “new” nitrogen and other nutrient sources.* Limnology and oceanography, 1997. **42**(5part2): p. 1154-1165.
230. Wen, J., et al., *A unique aptamer-drug conjugate for targeted therapy of multiple myeloma.* Leukemia, 2016. **30**(4): p. 987-991.
231. Huang, Y.F., et al., *Molecular assembly of an aptamer–drug conjugate for targeted drug delivery to tumor cells.* ChemBioChem, 2009. **10**(5): p. 862-868.
232. Ramzi, M. and N. Shokrgozar, *MicroRNAs: Regulatory Biomarkers in Acute Myeloid Leukemia and Graft Versus Host Disease.* Clin. Lab, 2022. **68**: p. 247-255.
233. Parekh, P., et al., *Immunotherapy of CD30-expressing lymphoma using a highly stable ssDNA aptamer.* Biomaterials, 2013. **34**(35): p. 8909-8917.
234. Shi, H., et al., *In vivo fluorescence imaging of tumors using molecular aptamers generated by cell-SELEX.* Chemistry–An Asian Journal, 2010. **5**(10): p. 2209-2213.
235. Fernandez-Mercado, M., L. Manterola, and C.H. Lawrie, *MicroRNAs in Lymphoma: Regulatory Role and Biomarker Potential.* Curr Genomics, 2015. **16**(5): p. 349-58.
236. Pastor, F., et al., *CD28 aptamers as powerful immune response modulators.* Molecular therapy-Nucleic acids, 2013. **2**: p. e98.
237. Kryza, D., et al., *Ex vivo and in vivo imaging and biodistribution of aptamers targeting the human matrix metalloprotease-9 in melanomas.* PLoS One, 2016. **11**(2): p. e0149387.
238. Ojima, A., et al., *DNA aptamer raised against advanced glycation end products inhibits melanoma growth in nude mice.* Laboratory Investigation, 2014. **94**(4): p. 422-429.
239. Li, H., et al., *A novel aptamer LL4A specifically targets vemurafenib-resistant melanoma through binding to the CD63 protein.* Molecular Therapy-Nucleic Acids, 2019. **18**: p. 727-738.
240. Varrone, F. and E. Caputo, *The miRNAs Role in Melanoma and in Its Resistance to Therapy.* Int J Mol Sci, 2020. **21**(3).
241. McConnell, E.M., et al., *In vivo use of a multi-DNA aptamer-based payload/targeting system to study dopamine dysregulation in the central nervous system.* ACS Chemical Neuroscience, 2018. **10**(1): p. 371-383.
242. Imrich, S., M. Hachmeister, and O. Gires, *EpCAM and its potential role in tumor-initiating cells.* Cell adhesion & migration, 2012. **6**(1): p. 30-38.
243. Bukari, B., et al., *Non-invasive delivery of therapeutics into the brain: the potential of aptamers for targeted delivery.* Biomedicines, 2020. **8**(5): p. 120.
244. Shigdar, S., et al., *Cancer stem cell targeting: the next generation of cancer therapy and molecular imaging.* Therapeutic delivery, 2012. **3**(2): p. 227-244.
245. Xiang, D., et al., *Transforming doxorubicin into a cancer stem cell killer via EpCAM aptamer-mediated delivery.* Theranostics, 2017. **7**(17): p. 4071.
246. Zheng, J., et al., *Simultaneous targeting of CD44 and EpCAM with a bispecific aptamer effectively inhibits intraperitoneal ovarian cancer growth.* Theranostics, 2017. **7**(5): p. 1373.

247. Catuogno, S., C.L. Esposito, and P.H. Giangrande, *Stick-based methods for aptamer-mediated siRNA targeted delivery*, in *Design and Delivery of SiRNA Therapeutics*. 2021, Springer. p. 31-42.
248. Esposito, C.L., et al., *STAT3 gene silencing by aptamer-siRNA chimera as selective therapeutic for glioblastoma.* Molecular Therapy-Nucleic Acids, 2018. **10**: p. 398-411.
249. Affinito, A., et al., *The discovery of RNA aptamers that selectively bind glioblastoma stem cells.* Molecular Therapy-Nucleic Acids, 2019. **18**: p. 99-109.
250. Affinito, A., et al., *Targeting ephrin receptor tyrosine kinase A2 with a selective aptamer for glioblastoma stem cells.* Molecular Therapy-Nucleic Acids, 2020. **20**: p. 176-185.
251. Gutsaeva, D.R., et al., *Single-Stranded Oligonucleotide Aptamer Binding to P-Selectin Inhibits Adhesion of Sickle Red Blood Cells And Leukocytes to Endothelial Cells in Sickle Cell Disease Model Mice: Novel Therapeutics for Vaso-Occlusive Episodes.* 2009.
252. Biesecker, G., et al., *Derivation of RNA aptamer inhibitors of human complement C5.* Immunopharmacology, 1999. **42**(1-3): p. 219-230.
253. Wandtke, T., J. Woźniak, and P. Kopiński, *Aptamers in diagnostics and treatment of viral infections.* Viruses, 2015. **7**(2): p. 751-780.
254. Tombelli, S., M. Minunni, and M. Mascini, *Analytical applications of aptamers.* Biosensors and Bioelectronics, 2005. **20**(12): p. 2424-2434.
255. Sypabekova, M., et al., *Selection, characterization, and application of DNA aptamers for detection of Mycobacterium tuberculosis secreted protein MPT64.* Tuberculosis, 2017. **104**: p. 70-78.
256. Mirian, M., et al., *Oligonucleotide aptamers: potential novel molecules against viral hepatitis.* Research in Pharmaceutical Sciences, 2017. **12**(2): p. 88.
257. Wang, Q., et al., *Screening of DNA aptamers against myoglobin using a positive and negative selection units integrated microfluidic chip and its biosensing application.* Analytical chemistry, 2014. **86**(13): p. 6572-6579.
258. McKeague, M., et al., *Development of a DNA aptamer for direct and selective homocysteine detection in human serum.* RSC Advances, 2013. **3**(46): p. 24415-24422.
259. Fu, Z. and J. Xiang, *Aptamers, the Nucleic Acid Antibodies, in Cancer Therapy.* International Journal of Molecular Sciences, 2020. **21**(8): p. 2793.

APPENDIX A

A1. Western Blot Images

A1-1: PTEN Fluorescent and Greyscale Blot Images

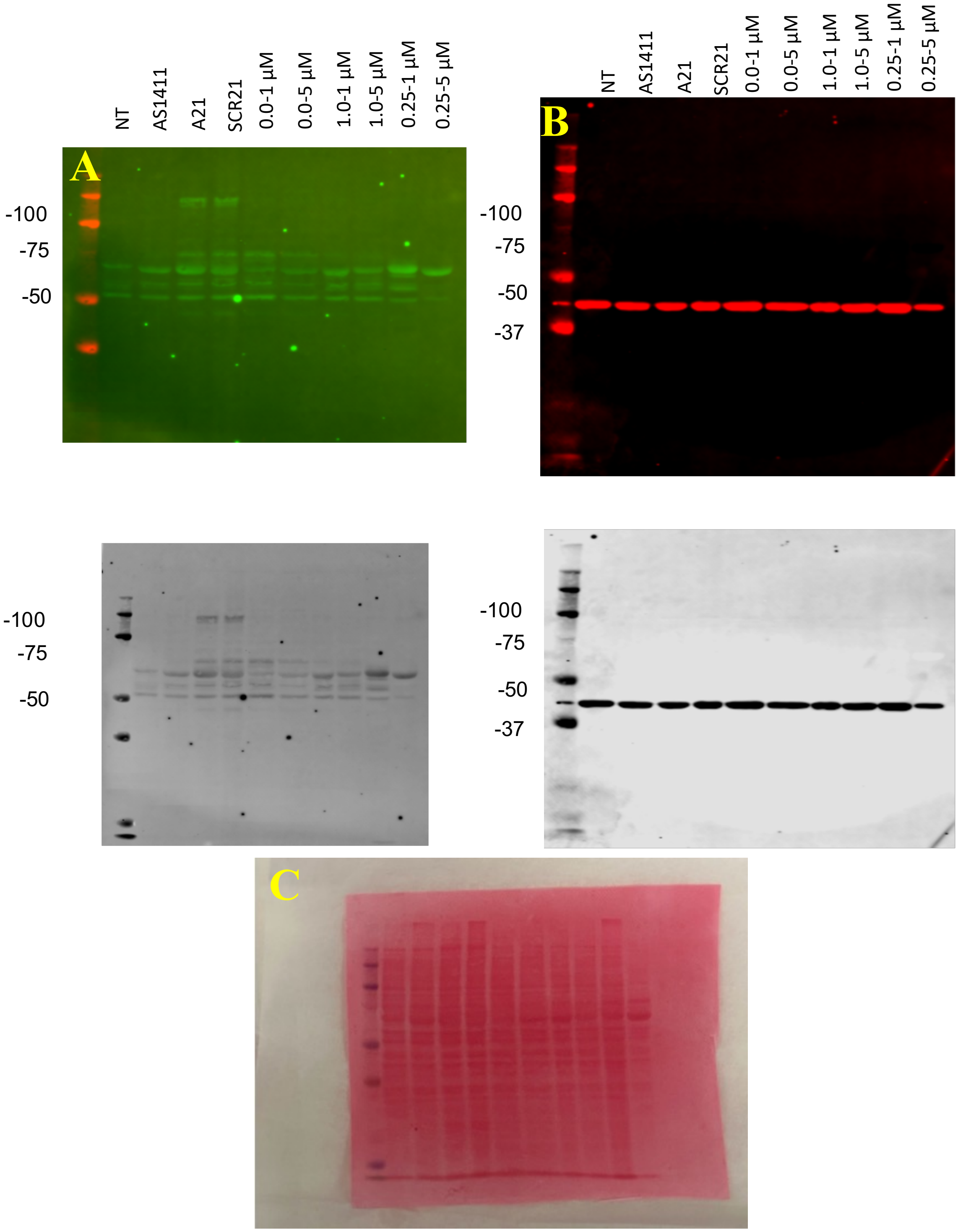

Figure A1-1.1: Fluorescent and greyscale image of Western Blot 1 investigating PTEN (A) and b-actin (B) expression. Ponceau S-Stained blots are shown in C. Sample names are listed above, and respective kDa of interest is labeled on the left, where needed.

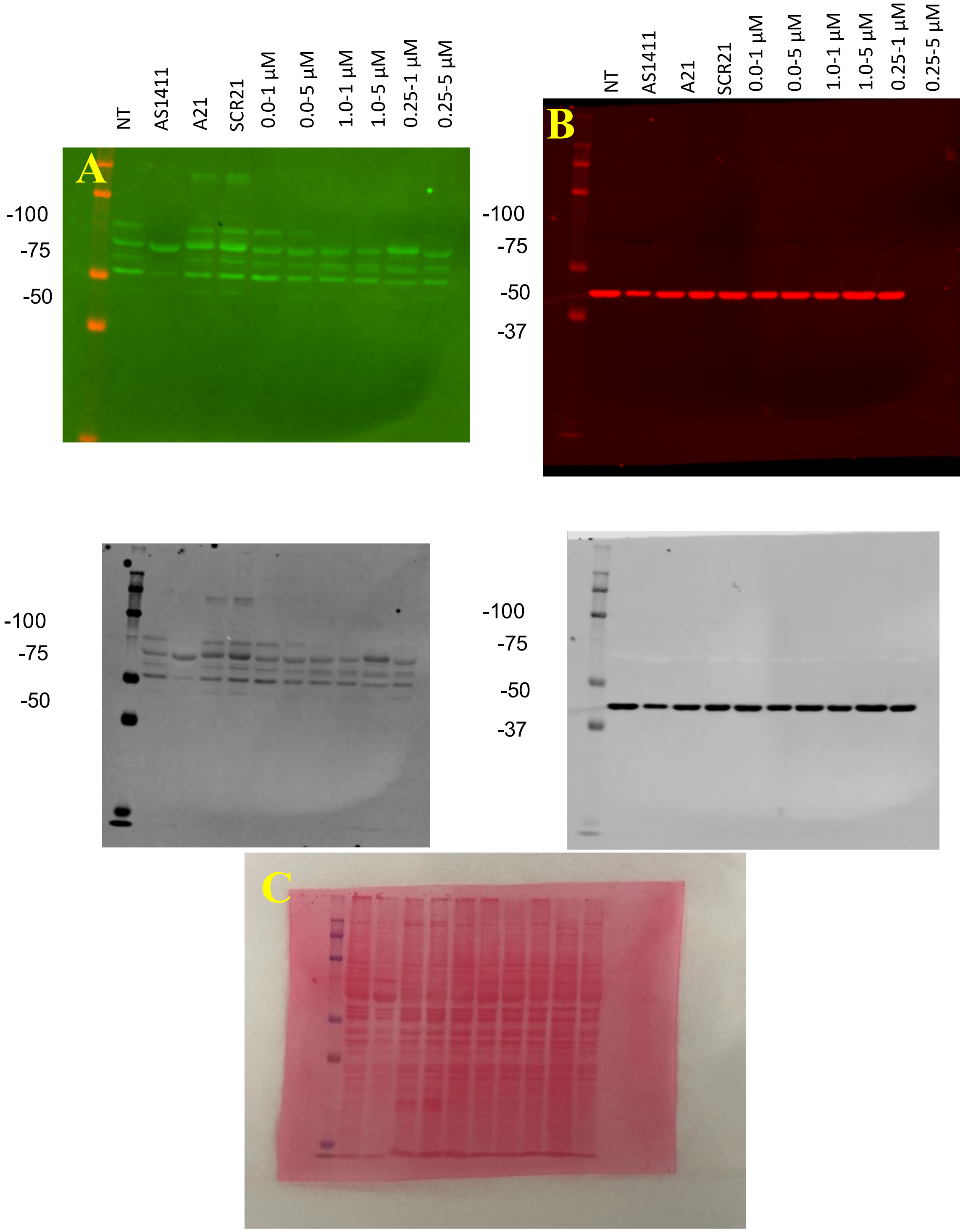

Figure A1-1.2: Fluorescent and greyscale image of Western Blot 2 investigating PTEN (A) and b-actin (B) expression. Ponceau S Stained blots are shown in C. Sample names are listed above, and respective kDa of interest is labeled on the left, where needed.

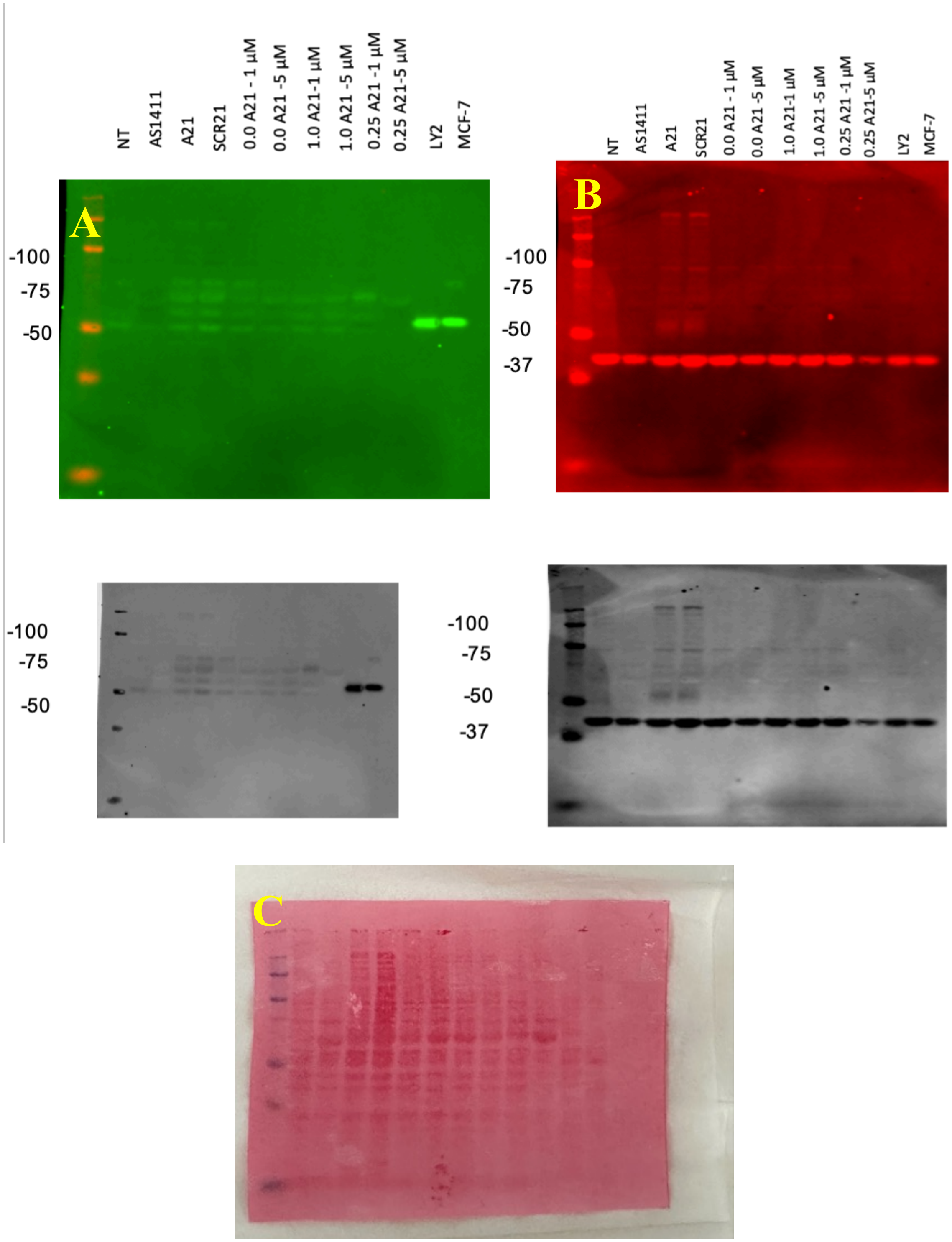

Figure A1-1.3: Fluorescent and greyscale image of Western Blot 3 investigating PTEN (A) and b-actin (B) expression. Ponceau S Stained blots are shown in C. Sample names are listed above, and respective kDa of interest is labeled on the left, where needed.

A1-2: STAT3 Fluorescent and Greyscale Blot Images

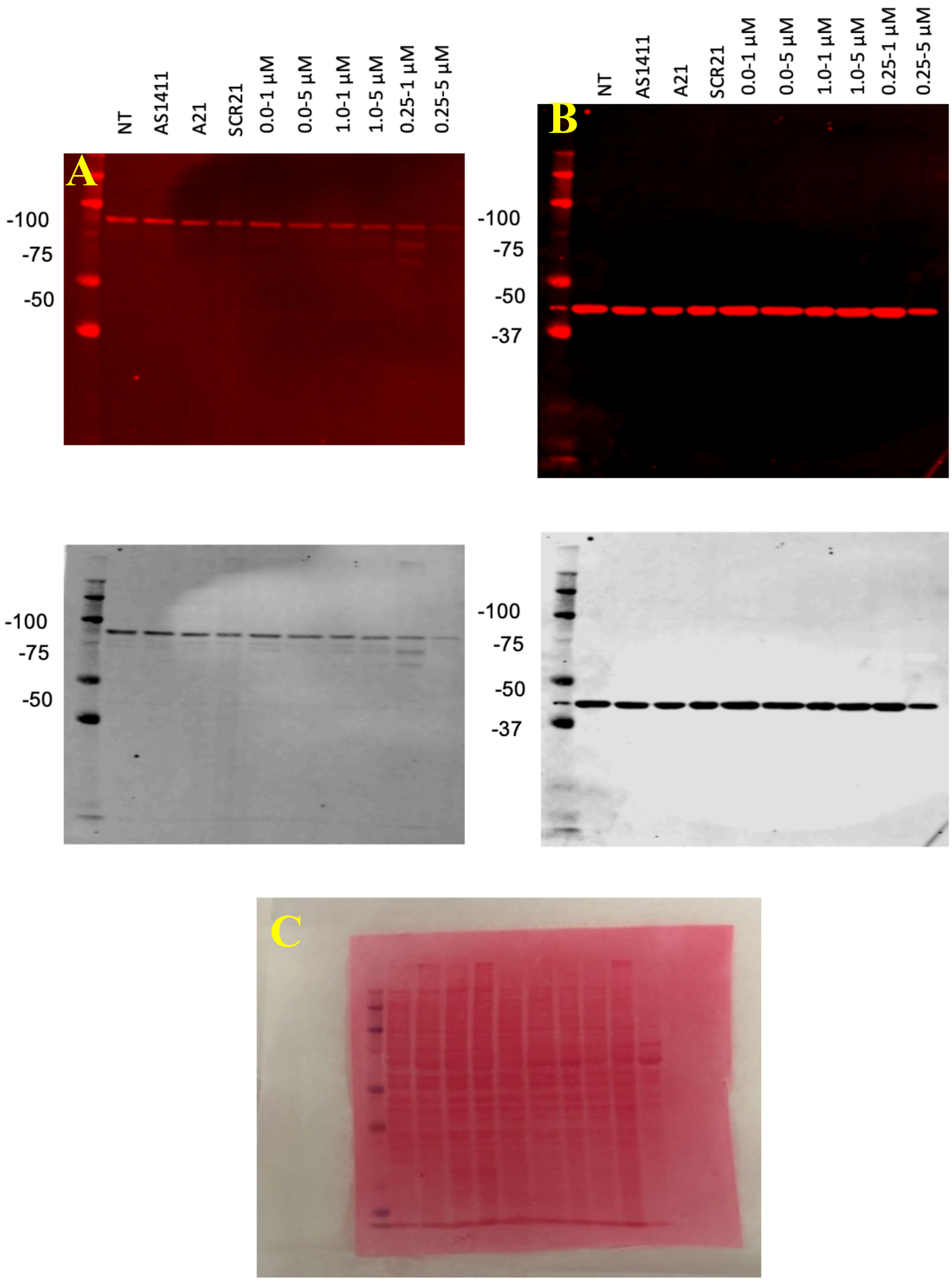

Figure A1-2.2: Fluorescent and greyscale image of Western Blot 1 investigating STAT3 (A) and b-actin (B) expression. Ponceau S Stained blots are shown in C. Sample names are listed above, and respective kDa of interest is labeled on the left, where needed.

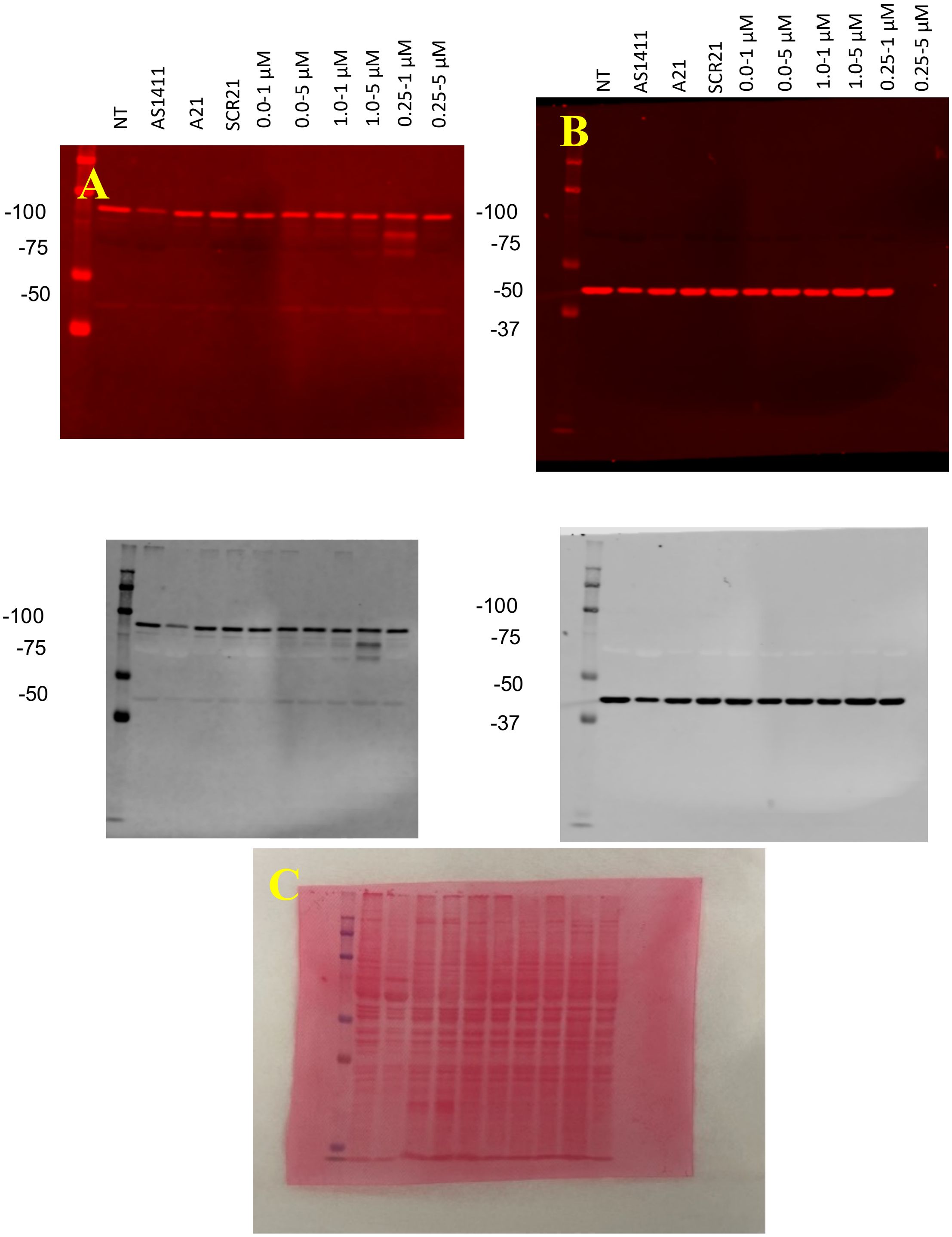

Figure A1-2.2: Fluorescent and greyscale image of Western Blot 2 investigating STAT3 (A) and b-actin (B) expression. Ponceau S Stained blots are shown in C. Sample names are listed above, and respective kDa of interest is labeled on the left, where needed.

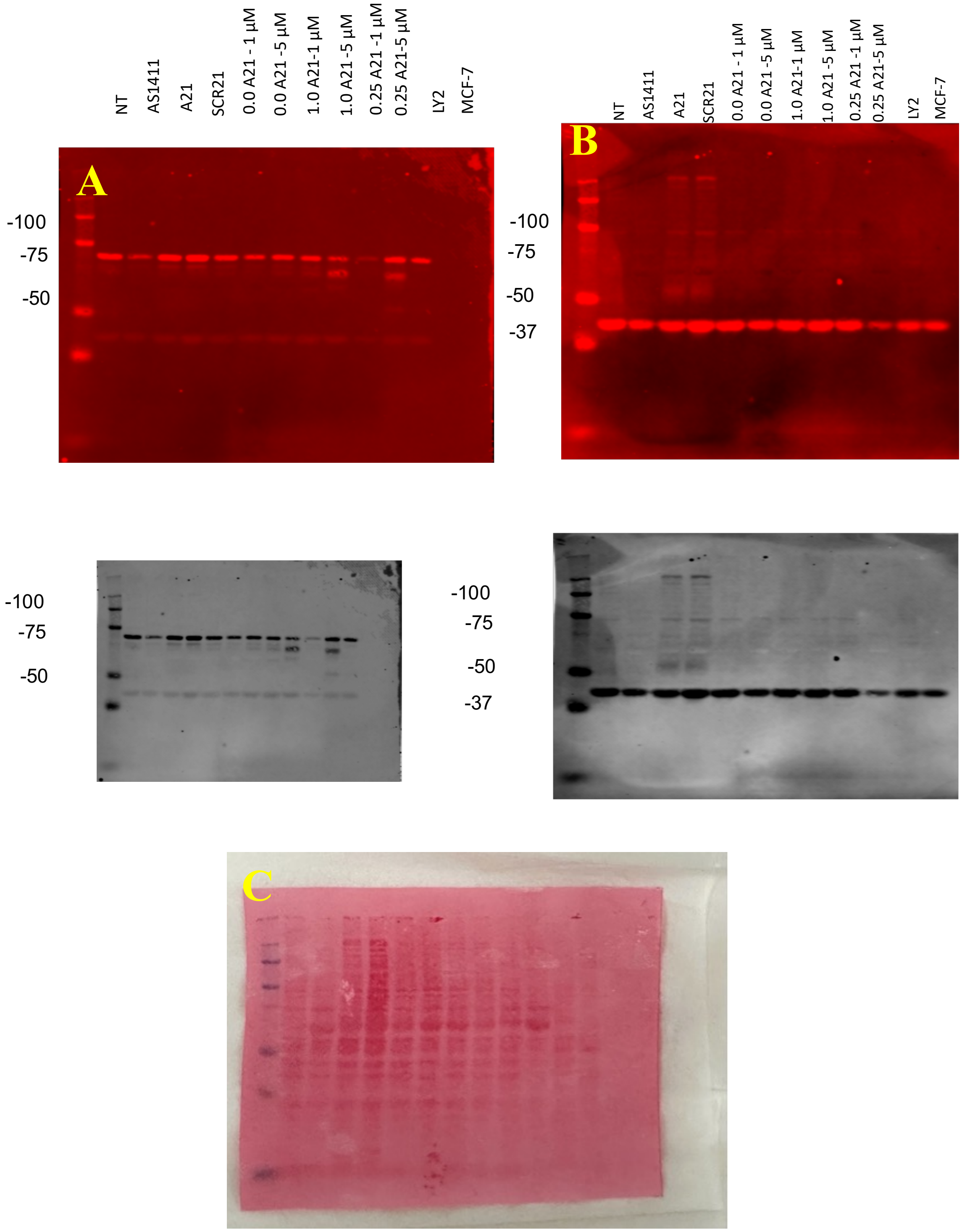

Figure A1-2.3: Fluorescent and greyscale image of Western Blot 3 investigating STAT3 (A) and b-actin (B) expression. Ponceau S Stained blots are shown in C. Sample names are listed above, and respective kDa of interest is labeled on the left, where needed.

CURRICULUM VITA

Name: Nicholas Allen

Address: 3401 Imperator Lane 103
Louisville, KY 40245

Skills and Expertise:

- Biochemical Assay Development
- Nanoparticle Design
- Sterile Technique/Cell Culture
- Mammalian Cell Culture
- Fluorescent Microscopy
- Animal Models
- Detail Oriented Organization
- Statistics and Design of Experiments
- Relationship Building

Work Experience:

PhD Candidate - Nanotherapeutic Lab **University of Louisville** **May 2017 – March 2023**

- Examine the *in vitro* and *in vivo* effects on glioblastomas from the combined treatment with AS1411 and anti-miR21 DNA and RNA oligos conjugated gold nanoparticles in a fast-paced entrepreneurial lab environment.
- Optimize synthesis of DNA and RNA-loaded gold nanoparticle constructs and characterize using UV-VIS, DLS, size-exclusion chromatography, HPLC, and biological assays
- Conjugate gold nanoparticles with PEG and DNA via thiol-gold chemistry
- Evaluated loading of various oligos on gold nanoparticles to determine maximum DNA activity *in vitro*
- Independently determined modification of nanoparticles with anti-miR21 via Sulfo-NHS and EDC chemistry
- Evaluate nanoparticle uptake and effects on glioblastoma motility via confocal live cell imaging
- Determine nanoparticle bioactivity against glioblastoma using morphological images from an epiflorescent microscope, gel electrophoresis, western blots, and metabolic, proliferation, BCA, and qPCR assays
- Analyzed all via Microsoft Excel, ImageJ, and GraphPad Prism
- Investigate *in vivo* effects of nanoparticle designs in large group animal studies within UofL Animal Facilities
- Performed Teaching Assistant role within Bioengineering and Chemistry Departments for six courses since 2018

- Taught Organic Chemistry and Cell Culture Labs on standard chemistry analysis techniques
- Assisted for Tissue Engineering, Nanoengineering, Anatomy and Physiology, Research Bioethics
- Graded lab reports, lab performance, and specific presentations within each course

REACH Academic Tutor and Supervisor **University of Louisville** **January 2013 – Present**

Small and Large Group Master Tutor (Spring 2013 – August 2022)

- Lead supplemental instruction in large (20-100 students) or small group settings (1-5 students) for 14 different courses across seven different disciplines within three tutoring centers at UofL
- Coordinate lessons using in-depth handouts of material for additional instruction and comprehension

Peer Supervisor and Mentor (Fall 2013 – August 2022)

- Evaluate a cumulative number of approximately 60 tutors in job progress and development as a tutor
- Conduct regular observations throughout the semester
- Update attendance data of each tutor's sessions and give final evaluation of tutor's performance

Undergraduate Co-ops **Various**

Lab of Tissue Engineering and Biomimetics (Louisville, KY – Summer 2013 and M.Eng 2015-2016)

- Collaborated within a cross functional tissue engineering research team analyzing the structural and functional effects on human cardiac fibroblasts post radiation exposure
- Utilized cell culture techniques to effectively evaluate radiation effects on ROS production and protein production within independently designed ROS, BCA, and ELISA assays
- Evaluated z-stacks of decellularized human cardiac ECM for differences in volume of fluorescently labeled proteins pre and post radiation exposure
- Evaluated fibrotic markers within cardiac fibroblasts via fluorescent volume analysis
- Investigated fibroblast migratory potential from mice aortas
- Analyzed data from BCA, ROS, ELISA, outgrowth assays, and fluorescent image analysis via Microsoft Excel, ImageJ, and GraphPad Prism

Lab of Regenerative Medicine (Houston, TX – Summer 2014)

- Explored the decellularization of various tissues for regenerative medicine applications
- Learned surgical isolation techniques used for tissue harvesting and independently designed experimental plan for the decellularization and re-endothelialization of mammary arteries for CABG grafts
- Paraffin embedded and examined histological stains of mammary arteries

Lab of Structural Biology (Louisville, KY – Spring 2015)

- Investigated protein-protein interaction within serum-plasma from melanoma patients
- Performed essential analytical lab techniques such as Size Exclusion Chromatography, BCA assay, DSC, and SDS PAGE gel electrophoresis
- Used Origin 7.0 (data analysis software) to analyze large quantities of experimental data

Education:

Ph.D. in Interdisciplinary Studies of Translational Bioengineering	J.B. Speed School of Engineering University of Louisville	Anticipated May 2023
M.Eng in Bioengineering: Highest Honors	J.B Speed School of Engineering University of Louisville	August 2016
B.S. in Bioengineering; summa cum lade; Minor of Pure Mathematics	J.B. Speed School of Engineering University of Louisville	May 2015

Professional Accomplishments:

***Publications**:*

- Nick Allen, Luis Rodriguez, Paula Bates, Carolyn Klinge, Martin O’Toole. **“Synthesis and Evaluation of Tumor Targeting Gold Nanoparticles with RNAi for Glioblastoma Applications.”** *Pharmaceutics*. In peer review.
- Nick Allen, Rajat Chauhan, Paula Bates, Martin O’Toole. **“Optimization of Tumor Targeting Gold Nanoparticles for Glioblastoma Applications.”** *Nanomaterials.* https://www.mdpi.com/2079-4991/12/21/3869/htm
- Nick Allen, Martin O’Toole. “**Advancements in Oligonucleotide-Based Therapies for Use in Glioblastoma.**” *Journal of Nanoparticle Research*. In peer review.
- Rajat Chauhan, Nick Allen, Robert Keynton, Paula Bates, Mohammed Malik, Martin O’Toole. “**Engineering Sequence and Stimuli Dependent Doxorubicin Release from anti-nucleoli aptamer coated gold nanoparticles,”** 2018 IEEE International Symposium On Signal Processing and Information Technology. https://doi.org/10.1109/ISSPIT.2018.8642659

Patents:

- Paula Bates, Martin O’Toole, Nick Allen. **“Anti-Nucleolin Agent-Conjugated Nanoparticles.”** US Patent No. 62/898,527. In review.

Memberships and Service:

Volunteer for UofL INSPIRE (Summer 2014, 2017, 2018, 2021, 2022)

- Present to high school students the opportunities of pursuing a Bioengineering Degree at UofL

Biomedical Engineering Society (Member: Fall 2012- present)

- Planned and volunteered for Engineering Expo, which showcased various Bioengineering projects to students of primary through high school levels to motivate interest in the sciences

UL chapter Secretary: Summer 2013 – Spring 2014

- Maintained updated records for society on all social, fundraising, and professional events.
- Worked with the elective council to plan each semester's events and organized schedules to coordinate all events

UL chapter Treasurer: Fall 2014

- Maintained financial records of all events planned for society
- Collected local and national membership dues by BMES guidelines
- Organized sending 3 UofL BMES members to a national conference in San Antonio, TX

Mortar Board National Honor Society (Member: Summer 2013- present)
Secretary: Fall 2014

- Maintained detailed meeting notes and assisted in organizing membership events
- Proposed and developed a plan for a university-wide academic hall of fame

Tutor for Upward Bound – ECTC (Spring 2012)

- Worked with local underprivileged high schools and tutored students in science and mathematics subjects

Phi-Theta Kappa National Community College Honor Society (Member: Fall 2011)
Nominee for Golden Key National Honor Society